



博士学位论文

DOCTORAL DISSERTATION

CENTRAL CHINA NORMAL UNIVERSITY

Wuhan, CHINA

**Centrality Dependence of K_S^0 and Λ elliptic flow in
Au + Au collisions at $\sqrt{s_{NN}} = 200$ GeV**

A dissertation submitted

for the degree of

Doctor of Philosophy in Physics

by

Yan Lu

Co-supervisors: Feng Liu, Nu Xu



博士学位论文
DOCTORAL DISSERTATION

© Copyright by

Yan Lu

2007

All Rights Reserved



Dedicated to my dear father and mother.



摘要

几千年来，人类一直在问一个问题：在我们生活的世界，什么是物质的基本组成部分？1808年道尔顿建立了原子论，表明物质是由原子组成的。随着近代科技的发展，人类发现原子又是由电子和原子核组成。原子核包括质子和中子。随后，通过电子打核子的深度非弹实验，人们认识到这些粒子可能由更基本的结构组成，这就是夸克和胶子。但是在自然界，我们没有观察到自由存在的夸克。一种自然的解释是夸克通过相互作用被禁闭在强子里，这种相互作用称为强相互作用。量子色动力学（QCD）是描述强相互作用的理论。QCD理论的一个重要特征是渐进自由，即夸克之间的相互作用强度与距离成正比，只有在距离很小的时候，强相互作用才变弱。分开两个夸克要无穷的能量，所以不可能把它们分开。QCD理论描述了夸克禁闭。QCD理论预言在极高温或高重子数密度下，强子物质会解除禁闭形成夸克胶子等离子体（Quark Gluon Plasma）。在这种新的物质形态内，夸克和胶子可以在较大的（超出核子）范围内运动。

夸克胶子等离子体可能存在于宇宙大爆炸早期阶段（很高的温度）以及中子星（重子数密度很高）内。在实验室里，我们让两束高能重离子束流以极高的能量对撞，产生高温高密的强相互作用物质，有可能在实验室里产生QGP。在美国布鲁克海汶国家实验室（Brookhaven National Laboratory）的相对论重离子对撞机（Relativistic Heavy Ion Collider）是当今世界上正在运行的质心能量最高的重离子对撞机。RHIC的最高质心系能量（核核对撞）是 $\sqrt{s_{NN}} = 200$ GeV。在西欧核子中心CERN运行的大型强子对撞机（Large Hadron Collider）将实现更高的质心系能量（pp对撞 $\sqrt{s_{NN}} = 14$ TeV，重离子对撞 $\sqrt{s_{NN}} = 5.4$ TeV）。

相对论重离子碰撞可以描述为两个高度洛仑兹收缩的核以接近光速对撞。在RHIC能区上，两个核将相互穿透，在中心快度区形成一个高能量，低净重子数的碰撞区。初始碰撞主要是部分子之间大横动量的硬碰撞。随着部分子之间相互作用的频繁发生，夸克将有可能解禁闭并达到热平衡。这个态也就是寻找的夸克胶子等离子体。随着系统的膨胀，系统开始冷却，部分子开始冻结成强子。当非弹性散射停止，强子的相对数目将不再改变，系统达到化学冻结。随着系统继续冷却，强子间的相互作用停止，系统达到动力学冻结。



实验上，我们测得末态的强子分布，希望通过末态强子信息寻找夸克胶子等离子体存在的信号。”集体行为”是指在一次碰撞中所观察到的多个粒子的共同性质，它是一种可能信号。”集体行为”源于中心快度区形成的火球从中心到边缘的密度梯度。火球中心的密度比边缘的密度高，组分粒子之间的相互作用推动形成的物质向外扩张。频繁的相互作用使组分粒子有一个相同的速度分布。我们称这种大量粒子具有相同的运动方向和速度为”集体流”。由于方向的不同，流分为”纵向流”和”横向流”。”纵向流”描述粒子在初始束流方向上的集体行为。”横向流”描述粒子在垂直于初始束流方向上的集体行为。”横向流”又可以分为”径向流”和”各向异性流”。”径向流”描述粒子在某个方向的有相似的速度。”各向异性流”描述粒子”径向流”在不同方向的不同。各种流是整个集体流图像在不同方面的表现。

在非对心碰撞中（碰撞参数 b 不为零），”反应平面”定义为碰撞参数和束流方向所决定的平面。系统初始坐标空间中的方位角各向异性相对于”反应平面”有一个椭圆的形状。它有利于我们研究”各向异性流”。密度梯度在椭圆短轴上比长轴上大。组分粒子的相互作用把密度梯度转化为压力梯度，导致压力梯度在椭圆短轴上比长轴上大。所以椭圆短轴上有较大的”径向流”。椭圆长轴和短轴之间的压力梯度差又由于粒子的运动速度在两个方向的差别而不断减小。在碰撞早期压力梯度大，椭圆流决定于早期，所以椭圆流可以提供系统早期的信息。

实验上，我们用末态粒子相对于”反应平面”的方位角分布的傅立叶展开来描述动量空间的各向异性。傅立叶展开的系数就是”各向异性流”参数。第二谐波系数对应于椭圆的方位角分布，称为”椭圆流”参数 v_2 。这篇论文中我们将集中讨论”椭圆流”参数 v_2 。

RHIC实验对各向异性椭圆流参数 v_2 测量已经有了很多的结果。在低横动量区，实验上观测到流体力学预言的强子质量顺序性，它表明在金金碰撞中已经形成了部分子层次的集体运动。进一步，在中间横动量区，实验上观测到组分夸克数目标度性，它表明系统达到了解禁闭状态。再进一步，多重奇异粒子横动量分布和椭圆流的结果预示系统可能达到了部分子层次的热化。值得注意的是，在RHIC能区，关于动力学热化的讨论直到现在还没有确定的结论。流体力学计算结果假设系统是理想流体，并成功的重复了RHIC能区的实验结果。流体力学对不同强子椭圆流的计算结果可以定量的符合RHIC能区金金碰撞中最小无偏事件的实验数据。但是，流体力学计算结果不能重复RHIC能区 π 介子和质子中心度的依赖性。另外，基于对带电粒子 v_2/ϵ_{part} 的讨论



暗示RHIC能区系统只可能在中心碰撞中达到热化。带电粒子 v_2/ε_{part} 随中心度的增加而增加, 这个结果表明系统不可能在最小无偏事件中达到热化。然而, 已有的结果, 讨论都集中在最小无偏事件中鉴别粒子的测量或带电粒子积分 v_2 的测量。鉴别粒子在不同中心度中的系统测量还是缺乏。这篇论文的物理动机是, 通过对鉴别粒子椭圆流在不同中心度中的系统测量, 系统的讨论集体运动, 横向运动能量标度性, 组分夸克数目标度性以及热化性质随中心度的依赖性。

我们分析了RHIC在2004运行中由STAR合作组收集的22,000,000最小无偏事件, 它是2002年运行数据的10倍。我们通过衰变道 $K_S^0 \rightarrow \pi^+ + \pi^-$, $\Lambda(\bar{\Lambda}) \rightarrow p(\bar{p}) + \pi^-(\pi^+)$ 来重建 K_S^0 和 $\Lambda(\bar{\Lambda})$ 。对任一对具有相反电荷的带子粒子, 我们通过衰变的几何截断来排除背景。我们发展了一种新的方法来快速有效的分析出几何截断的值。新的方法是在信噪比随给定几何截断的分布中, 截断值选取在信噪比较大的位置。

我们用反应平面和李杨零点的流分析方法分别对 v_2 进行了测量。以前对鉴别粒子所采用的流分析方法是反应平面方法, 它利用的是粒子和反应平面的角关联。这个方法不能去掉和反应平面无关的非流效应。最近提出的李杨零点的流分析方法利用是所有粒子的相互关联, 理论上它可以去掉非流效应。我们首次用李杨零点方法对 v_2 进行了测量。

在测量 v_2 中扣除背景的方法上, 我们首次用 v_2 的不变质量依赖性的方法。新的方法考虑了背景 v_2 随不变质量变化的效应, 它比以前采用的拟合信号方位角分布的方法更有力。

我们在金金碰撞质心系能量200 GeV中用李杨零点方法测量了带电粒子的椭圆流参数 v_2 , 并分别用反应平面方法和李杨零点方法测量了 K_S^0 和 $\Lambda + \bar{\Lambda}$ 粒子椭圆流参数 v_2 : v_2 的横动量分布, v_2 的横向运动能量分布, p_T 积分的 v_2 以及它们的中心度依赖性。在不同的中心度中, 我们将 K_S^0 和 $\Lambda + \bar{\Lambda}$ 粒子的测量结果和含有多个奇异夸克的 ϕ 介子, Ξ 和 Ω 重子的测量结果进行了系统的比较。我们也对流体力学的计算结果进行了讨论。

李杨零点方法测得的 v_2 值比反应平面方法要小10%, 而且两个方法的差别到横动量为5GeV/c都没有很强的横动量依赖性。在高横动量区, 喷注产生的非流效应期望比低横动量区要大。根据李杨零点方法所得的结果, 非流效应引起的系统误差在横动量为5GeV/c以下约为10%, 喷注产生的非流效应可能主要贡献在横动量大于5GeV/c以



上。

我们观测到在低横动量区间 ($p_T < 2 \text{ GeV}/c$)，不同的粒子的 v_2 都随横动量的增大而增大。对给定的横动量 p_T ，较重的强子的 v_2 值要比较轻的强子的 v_2 值小。这种强子质量的顺序性和流体力学的计算结果相一致。这表明了金金碰撞中不同质量的粒子形成了集体运动。含有多个奇异夸克的强子在强子阶段的相互作用截面很小，它们的 v_2 值和轻味夸克强子相似。这表明产生的集体运动起源于部分子阶段。并且在不同中心度的碰撞中，我们都观测到了这种强子质量的顺序性。在这个横动量区间，在不同的中心度碰撞中，所有测得的强子的 v_2 都符合横向运动能量 ($m_T - mass$) 标度性。

在中间横动量区间 ($2 \text{ GeV}/c < p_T < 5 \text{ GeV}/c$)， v_2 开始偏离流体力学的计算结果，随横动量增加的趋势减缓，然后饱和。如果把 v_2 和 p_T 都除以强子中组分夸克的数目 n_q 。重子和介子将符合同一条曲线。我们称之为组分夸克数目标度性。这个标度性本身，表明粒子的 v_2 有组分夸克自由度。组分夸克再组合模型可以定性解释这个这个标度性。在这类模型中，强子是在强子化阶段由组合两个或三个组分夸克形成的。如果这个解释正确的话，RHIC形成的物质已经解禁了。并且在不同中心度的碰撞中，我们都观测到了组分夸克数目标度性。结合横向运动能量标度性和组分夸克数目标度性，在不同的中心度中，我们得到一个新的标度性— m_T-n_q 标度性。

对不同中心度的碰撞，为了去掉初始的几何效应，我们把 v_2 除以初始坐标空间的各向异性参数 ϵ_{part} 。我们没有观测到 $v_2(p_T)/\epsilon_{part}$ 随中心度的标度性。带电粒子和奇异与多重奇异粒子的 $\langle v_2 \rangle / \langle \epsilon_{part} \rangle$ 都随着中心度(参加碰撞的核子数 N_{part})增加而增加。这表明在中心碰撞中的集体流要比偏心碰撞中要大。在热化的情况下， $\langle v_2 \rangle / \langle \epsilon \rangle$ 对中心度的依赖性应该消失。流体力学假设了局域热平衡， $\langle v_2 \rangle / \langle \epsilon \rangle$ 显示了对中心度比较弱的依赖性。 $\langle v_2 \rangle / \langle \epsilon_{part} \rangle$ 的实验值在 N_{part} 大于170的区间增加的趋势减缓并接近流体力学的计算结果。这表明在金金碰撞质心系能量200GeV中产生的系统在 N_{part} 大于170的对心碰撞中达到了局域热平衡。而在不同中心度中所观测到的集体运动，横向运动能量标度性，组分夸克数目标度性并不依赖于系统是否达到热平衡。

关键词: 相对论重离子碰撞 夸克胶子等离子体 集体运动 椭圆流参数 奇异粒子 K_S^0 和 Λ 横向运动能量标度性 组分夸克标度性 热化



Abstract

The heavy ion collisions at Relativistic Heavy Ion Collider (RHIC) located at Brookhaven National Laboratory (BNL) provide a high energy density environment of nuclear matter to search for Quark-Gluon Plasma (QGP) and study its properties. The signature of QGP formation has to be identified from the measured final-state hadrons. Measurements of azimuthal anisotropy in transverse momentum distribution of produced particles can get information on the early stage of the heavy ion collisions. From the data collected at RHIC during year 2002, the second harmonic azimuthal anisotropy, elliptic flow v_2 of identified particles from Au + Au collisions established hydro-like mass hierarchy at low p_T . This observation demonstrates the development of partonic collectivity. Further, the Number-of-Constituent-Quark scaling observed at intermediate p_T suggest the system has been in the deconfined state prior to hadronization. On the other hand, charged particle $\langle v_2 \rangle$ scaled by the eccentricity suggests possible thermalization only in the most central collisions at RHIC. The comparisons have been focused either on identified hadrons from minimum bias collisions or integrated v_2 of charged hadrons. A systematic comparisons for identified hadrons at different collision centralities are still scarce. The centrality dependence of v_2 measurement for identified particles will gain information on interplay of collectivity, NQ scaling and thermalization as a function of collision centralities.

This thesis presents STAR results on the elliptic flow v_2 of K_S^0 and $\Lambda + \bar{\Lambda}$ from $\sqrt{s_{NN}} = 200$ GeV Au + Au collisions at RHIC. The high statistics data were collected at RHIC during year 2004. The detailed study of centrality dependence of v_2 over a broad transverse momentum range is presented. The results from Lee-Yang Zero method and Event Plane method are shown. Comparisons with multi-strange particles ϕ , $\Xi + \bar{\Xi}$ and $\Omega + \bar{\Omega}$ are made for systematic study of identified particles.

In the relatively low p_T region ($p_T < 2$ GeV/c), for a given p_T , the heavier particle has smaller v_2 than the lighter particle. This mass ordering is predicted by the hydrodynamical calculations. The hydro-like mass hierarchy is observed for all centrality bins.



In this p_T region, a scaling with kinetic energy $m_T - m$ is observed for all measured identified hadrons in each centrality bin.

In the higher p_T region, v_2 deviates from hydrodynamical calculations and then saturates or decreases. Baryon saturates at higher p_T with larger values of v_2 than meson. For all measured hadrons, v_2 scaled by the number of quark n_q within a given hadron follows a universal curve as a function of p_T scaled by n_q . This Number-of-Quark scaling is observed for all centrality bins.

n_q -scaled v_2 is divided by the participant eccentricity for different centralities to remove the initial geometry effect. We do not observe $v_2(p_T)$ scaled by the participant eccentricity ε_{part} to be independent of centrality. As a function of collision centrality, an increase of $\langle v_2 \rangle / \langle \varepsilon_{part} \rangle$ has been observed. This indicates a stronger collective flow in more central Au + Au collisions.

For hydrodynamical calculations with assumptions of local thermalization, $\langle v_2 \rangle / \langle \varepsilon \rangle$ shows little sensitivity to centrality bins. The rate of increase in $\langle v_2 \rangle / \langle \varepsilon_{part} \rangle$ for data appears to slow down when $N_{part} > 170$ and approach that from the hydrodynamic model calculations. This indicates that the system created in 200 GeV Au + Au collisions reached local thermalization in central collisions when the number of participants is larger than 170. Further, the observed collectivity, $m_T - m$ scaling and number-of-quark scaling do not depend on local thermalization.

Keywords: Relativistic heavy ion collisions, Quark Gluon Plasma, Elliptic flow v_2 , Strange particle K_S^0 and Λ , $m_T - m$ scaling, Number-of-Quark scaling, Thermalization



TABLE OF CONTENTS

1	Introduction	1
1.1	Elementary Particles and Interactions	1
1.2	Quantum Chromo Dynamics and Asymptotic Freedom	3
1.3	Deconfined Quark Matter	4
1.4	Relativistic Heavy Ion Collisions	7
1.5	Theoretical Description of Heavy Ion Collisions	8
1.5.1	pQCD Description	8
1.5.2	Hydrodynamics	9
1.6	Experimental Observations	11
1.6.1	Hard Probe: Jet Quenching	11
1.6.2	Bulk Properties and Collective Dynamics	13
1.7	Centrality Dependence of v_2 Measurements	23
2	Experimental Setup	24
2.1	History of Heavy Ion Accelerator Facilities	24
2.2	The Relativistic Heavy-Ion Collider	25
2.3	RHIC Experiments	27
2.4	STAR Detector Systems	28
2.5	STAR Time Projection Chamber	31
2.5.1	Sub-structures	32
3	Analysis Method	37
3.1	Event and Track Selection	37



3.2	V0 Reconstruction	40
3.3	Event Plane Method	48
3.3.1	Event Plane Reconstruction	48
3.3.2	Flattening Event Plane Distribution	49
3.3.3	Event Plane Resolution	51
3.4	Sub-event Method	53
3.5	Lee-Yang Zero Method	54
3.5.1	Integrated Flow	55
3.5.2	Differential Flow	57
3.5.3	Product Generating Function	59
3.6	v_2 versus m_{inv} Method	59
3.7	Systematic Errors	62
4	Results	65
4.1	Glauber calculations	65
4.2	Elliptic Flow	66
4.2.1	Event Plane Method Results	66
4.2.2	Lee-Yang Zero Method Results	67
5	Discussion	71
5.1	Collective Flow	71
5.1.1	p_T Dependence	72
5.1.2	Centrality Dependence	74
5.1.3	$m_T - m$ Scaling	74
5.1.4	NQ Scaling	76
5.1.5	ε_{part} Scaled v_2	82
5.1.6	Energy Dependence	85



6 Summary and Outlook	89
A Anisotropic Flow at RHIC: How Unique is the Number-of-Constituent- Quark Scaling?	92
References	99
Presentations and publication List	104
Acknowledges	110



LIST OF FIGURES

1.1	Summary of fundamental particles	2
1.2	Summary of four fundamental interactions	2
1.3	Color screening of confining potential	5
1.4	Phase transition from lattice QCD prediction	6
1.5	Time evolution of a heavy ion collision	7
1.6	Equation of State	10
1.7	R_{AB} and di-hadron azimuthal correlations	12
1.8	p_T -integrated yield ratios for different hadron species	14
1.9	Freeze-out temperature versus collective velocity from blast wave fit	15
1.10	Spatial and momentum space azimuthal anisotropy	16
1.11	Initial particle density gradient	17
1.12	Two components of hydrodynamic flow	17
1.13	Charge particle v_2/ε versus $\frac{1}{5}dN_{ch}/dy$ from AGS, SPS to RHIC energies.	19
1.14	Minimum bias v_2 at low p_T	20
1.15	Minimum bias v_2 at intermediate p_T and Number-of-Constituent-Quark scaling	22
2.1	RHIC acceleration complex	26
2.2	RHIC experiments	27
2.3	Cutaway side view of the STAR detector	28
2.4	STAR trigger provided by ZDC and CTB	30
2.5	Perspective view of the STAR TPC	31
2.6	Design of inner field cage of TPC	33
2.7	Full sector pad plane of TPC end caps	35



2.8	Outer sub-sector wire geometry of TPC end-caps	36
3.1	Multiplicity distribution and centrality definition	39
3.2	V0 decay topology	41
3.3	Invariant mass distribution of $\Lambda + \bar{\Lambda}$ candidates and backgrounds	41
3.4	V0 cuts selection	43
3.5	Invariant mass distribution of K_S^0	46
3.6	Invariant mass distribution of $\Lambda + \bar{\Lambda}$	47
3.7	Phi weights	50
3.8	Event plane distribution	51
3.9	Event plane resolution	53
3.10	The first minimum of generating function	57
3.11	Centrality and θ dependence of the first minimum	58
3.12	v_2 versus m_{inv} method	61
3.13	Charged particle integrated v_2	62
3.14	$v_2\{LYZ\}/v_2\{EP\}$ as a function of p_T	63
4.1	Glauber Calculations	66
4.2	Minimum bias v_2 from Event Plane method.	68
4.3	Centrality dependence of v_2 from Event Plane method.	68
4.4	Mid-central v_2 from Lee-Yang Zero method.	69
4.5	Centrality dependence of v_2 from Lee-Yang Zero method.	70
5.1	p_T dependence	73
5.2	$m_T - m$ dependence	75
5.3	Number-of-quark scaling for minimum bias	77
5.4	Centrality dependence of number-of-quark scaling I	78



5.5	Centrality dependence of number-of-quark scaling II	79
5.6	m_T - n_q -scaling with Lee-Yang Zero method	80
5.7	$v_2(p_T)/\epsilon_{part}$	83
5.8	v_2/ϵ_{part} versus N_{part}	84
5.9	Energy dependence of $v_2(p_T)$	86
5.10	Energy dependence of $v_2/(n_q \times \epsilon_{part})$	87
A.1	93
A.2	95
A.3	96



LIST OF TABLES

2.1	RHIC performance parameters	25
3.1	Trigger and events selection	37
3.2	STAR centrality definition for Run IV	38
3.3	K_S^0 and $\Lambda(\bar{\Lambda})$ weak decay	40
3.4	K_S^0 V0 cuts	44
3.5	$\Lambda + \bar{\Lambda}$ V0 cuts	44
3.6	Selection criteria for flow tracks	49
4.1	Glauber calculations in Au + Au collisions at $\sqrt{s_{NN}} = 200$ GeV. The nucleon-nucleon interaction cross section σ_{NN} of 42mb is used in the calculation.	65



CHAPTER 1

Introduction

1.1 Elementary Particles and Interactions

For thousands of years, human beings keeps asking the question: what elementary components are the matter in the world we live nowadays made up of? In 1808, John Dalton developed the atomism (theory of atom), which suggests the matter is composed of the atoms. In 1897, J. J. Thomson found atom was not an "indivisible" particle with his discovery of the electron [Tho897]. In 1911, Ernest Rutherford found the the existence of atomic nuclear [Rut11a, Rut14a] through the experiment of scattering α -particles off gold foil. Nuclear is composed of protons and neutrons, which are called nucleons. As many "elementary particles" such as pion, kaon are found, physicists doubt that there are more fundamental particles. In 1964, Gell-Mann and G. Zweig suggest that these particles are made up of quarks [Gel64a, Zwe64a]. Further, in 1969, the first evidence for the existence of quarks [Bre69a] was obtained through the experiment of probing the internal structure of the nucleon via deep inelastic electron scattering (DIS) in Stanford Linear Accelerator Center. So in the field of particle physics, an elementary particle or fundamental particle is defined as a particle, which doesn't have unknown sub-structures.

Standard Model summarized the known elementary particles listed in Figure 1.1. Fundamental particles are fermions, which are defined as particles with spin $\frac{1}{2}$. Interactions between fundamental fermions are described by exchange of characteristic bosons, which are defined as particles with integral spin. Bosons are the interaction mediators characterizing their interactions. There are four types of fundamental interactions: Gravitation, Electromagnetic interaction, Weak interaction and Strong interaction. There are



FERMIONS						matter constituents spin = 1/2, 3/2, 5/2, ...					
Leptons spin = 1/2			Quarks spin = 1/2			BOSONS			force carriers spin = 0, 1, 2, ...		
Flavor	Mass GeV/c ²	Electric charge	Flavor	Approx. Mass GeV/c ²	Electric charge	Unified Electroweak spin = 1			Strong (color) spin = 1		
						Name	Mass GeV/c ²	Electric charge	Name	Mass GeV/c ²	Electric charge
ν_e electron neutrino	$<1 \times 10^{-8}$	0	u up	0.003	2/3	γ photon	0	0	g gluon	0	0
e electron	0.000511	-1	d down	0.006	-1/3	W⁻	80.4	-1			
ν_μ muon neutrino	<0.0002	0	c charm	1.3	2/3	W⁺	80.4	+1			
μ muon	0.106	-1	s strange	0.1	-1/3	Z⁰	91.187	0			
ν_τ tau neutrino	<0.02	0	t top	175	2/3						
τ tau	1.7771	-1	b bottom	4.3	-1/3						

Figure 1.1: The summary of the known fundamental particles: quarks, leptons and the interaction mediators. The figure is from <http://particleadventure.org>.

Interaction	Mediator	Spin Parity	relative magnitudes	interaction range
strong	gluon, g	1^-	1	$\sim 10^{-13}$ cm
electromagnetic	photon, γ	1^-	10^{-2}	∞
weak	W^\pm, Z^0	$1^-, 1^+$	10^{-12}	$\sim 10^{-16}$ cm
gravity	graviton, g	2^+	10^{-38}	∞

Figure 1.2: Summary of four fundamental interactions. The figure is from <http://particleadventure.org>.



six flavor quarks: up (u), down (d), strange (s), charm (c), bottom (b), top (t). Quarks have fractional electric charge. The mass listed in Figure 1.1 is the bare mass. The strong interaction is responsible for binding quarks in nucleons and nucleons in the nuclei. The strong interaction mediator is gluon. There are six leptons: electron (e), muon (μ), tau (τ) and their corresponding neutrinos. The electromagnetic interaction is responsible for the phenomena associated with the electric charges. The electromagnetic interaction mediator is photon. The weak interaction appears in decay processes. The weak interaction mediator is W^\pm and Z^0 bosons. The gravitational interaction exists between all particles. The gravitation mediator, graviton is not listed in Figure 1.1 since there is no experimental evidences of observation of gravitons. In Figure 1.2, features of four interactions are summarized. The gravitation is the weakest interaction. The strong interaction and weak interaction are short-range interactions.

1.2 Quantum Chromo Dynamics and Asymptotic Freedom

Quarks are the building blocks of nucleons and all hadronic matter. Quantum Chromo Dynamics is thought to be the correct theory to describe strong interactions of quarks and gluons. It is a non-abelian gauge field theory based on $SU(3)_c$, where subscript c denotes the quantum number - color. Each flavor has three colors: Blue, Green, Red. In QCD, quarks interact with each other by exchanging the color force mediator gluons. This is analogous to the electromagnetic force mediator photons. However, unlike photons carry no electric charge, gluons do carry color charges due to the non-abelian character of the color group. So gluons can interact with each other and quarks. Hadrons are the color-singlet combination of quarks, anti-quarks and gluons. The only free parameters in QCD are the bare quark mass and the strong coupling strength g_s between quarks and gluons. g_s is determined from the experiment. Unlike the electrodynamic coupling constant $\alpha = \frac{1}{137}$ is a constant, the strong coupling constant $\alpha_s = \frac{g_s^2}{4\pi}$ varies with energies.

The renormalized QCD coupling α_s depends on the energy scale μ . The running



coupling constant $\alpha_s(\mu)$ can be written as:

$$\alpha_s(\mu) \equiv \frac{g_s^2(\mu)}{4\pi} \approx \frac{4\pi}{\beta_0 \ln(\mu^2/\Lambda_{QCD}^2)} \quad (1.1)$$

Where $\beta_0 = 11 - \frac{2}{3}n_f$, n_f is the number of quarks with mass less than the energy scale μ . α_s averaged over different experiments in the world is 0.1187 ± 0.002 at the fixed-reference $\mu_0 = M_Z$ [Eid04a] and the QCD scale $\Lambda_{QCD} \sim 200$ MeV. α_s decreases logarithmically with increasing energies. The larger energy transfer the shorter distance, according to the uncertainty relation. So the strong force becomes smaller at shorter distance. This phenomenon is known as asymptotic freedom. Conversely, the coupling constant increases with decreasing energy. This means the strong force between quarks becomes stronger at larger distances when you try to separate them. So quarks seem to remain confined to a small region in colorless group of $q\bar{q}$ (mesons) or qqq (baryons).

Since the coupling constant is running, QCD is not a perturbative theory in general sense. Only when α_s is small in case of interactions involving high momentum transfer (i.e. hard process), QCD can be calculated perturbatively. The dominant processes in the universe are the soft processes, where perturbative QCD is not a valid approximation. Explicit QCD calculation can be made through numerical calculation: Lattice QCD [Wil74]. The numerical calculations are done on a discretized space-time lattice. The quark field is only defined on the lattice and the gluon field is only defined on the link of the lattice. Physical quantities are numerically calculated from the path integrals of the QCD Lagrangian. The expected value is obtained with the extrapolation extended to infinite small lattice spacing. The calculation ability of Lattice QCD is limited by the number and size of the lattice or the computing power.

1.3 Deconfined Quark Matter

Quarks are point-like and confined in the hadron by a binding potential $V_0(r)$, which increases with the quark separation r ,



$$V_0(r) \sim \sigma r \quad (1.2)$$

where the string tension σ measures the energy per unit separation distance. Infinite amount of energy are needed to isolate a quark. It's impossible to split a hadron into isolated quarks. A deconfined quark is defined as the one that can move in a volume much larger than the volume of a nucleon (a hadron). We have never seen deconfined quarks in normal temperature and density.

The interaction of quarks in QCD is based on their intrinsic color charges. Confinement is a long-range feature of color charges. The long-range feature is also the nature of electric charges. In a extreme high density of color charges, color charges can be screened in the same way as electric charges known as Debye screening: the long-range interaction is shortened in dense medium of charges. At high density, the potential with the expected color screening [Sat00a] is given by

$$V(r) \sim \sigma r \left[\frac{1 - \exp(-\mu r)}{\mu r} \right] \quad (1.3)$$

where μ is the color screening mass.

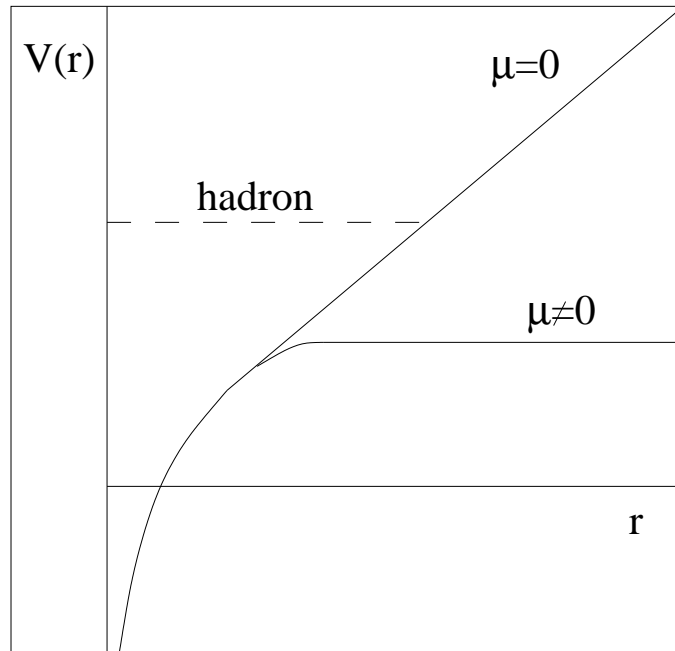


Figure 1.3: Color screening of confining potential. The calculations are from [Sat00a].



The Figure 1.3 shows the potential as a function of r . When μ is equal to 0, the potential increases linearly with r . When μ is not equal to 0, the potential remains a finite constant as r increases. The resulting damping of the binding force removes all long range effects. Color screening occurs at sufficiently high density, so one can image a simple picture: hadrons made up of point-like quarks start to overlap, so each quark finds a large number of quarks in the vicinity of the volume size equal to intrinsic spatial extension of nucleons. It is no way to identify which quarks are the original constituents of a specific nucleon at some previous state of low density. Beyond a certain point, the concept of a hadron loses its meaning. So under color screening, the interactions between the quarks and gluons will be short-range. The color insulator is transformed to the color conductor, and the hadron matter is transformed to the Quark Gluon Plasma [Sat00a].

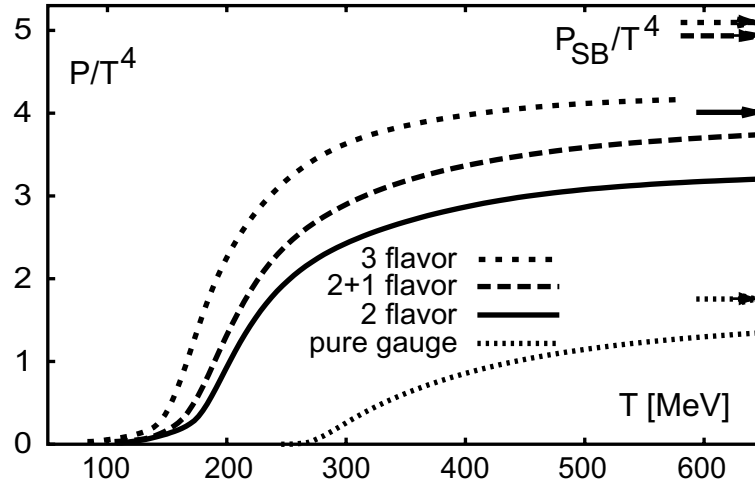


Figure 1.4: Pressure divided by T^4 as a function of T from LQCD calculation for several different choices of the number of quark flavors. The corresponding Stefan-Boltzmann pressure is indicated by the arrows near the right axis. LQCD calculation results from [Kar02a].

Recently, results from lattice QCD suggest that when sufficient high temperature is reached, quarks reveal effectively deconfined. The exposure of new (color) degrees of freedom should be manifested by a rapid increase in entropy density, hence in pressure, with increasing temperature. Figure 1.4 shows that above the critical temperature $T_c \sim 160\text{MeV}$, the ratio of the pressure divided by T^4 (where T is the system temperature) rapidly rises. This sharp increase reveals a transition from a hadronic phase to a QGP phase, in which quarks and gluons are the relevant degrees of freedom. The



arrows indicate the Stefan-Boltzman limits, where the deconfined quarks and gluons are non-interacting and massless. The deviation from the SB limit indicates remaining interactions among the quarks and gluons in the QGP phase.

1.4 Relativistic Heavy Ion Collisions

The main goal of building the Relativistic Heavy Ion Collider (RHIC) is to create bulk matter of deconfined quarks and gluons (Quark Gluon Plasma) and study its properties in extreme high temperature and density. The new form of matter created in the laboratory is believed to exist at very early stage of universe evolution. Studying QGP formation will help us to understand the fundamental structure of the matter and evolution of our universe.

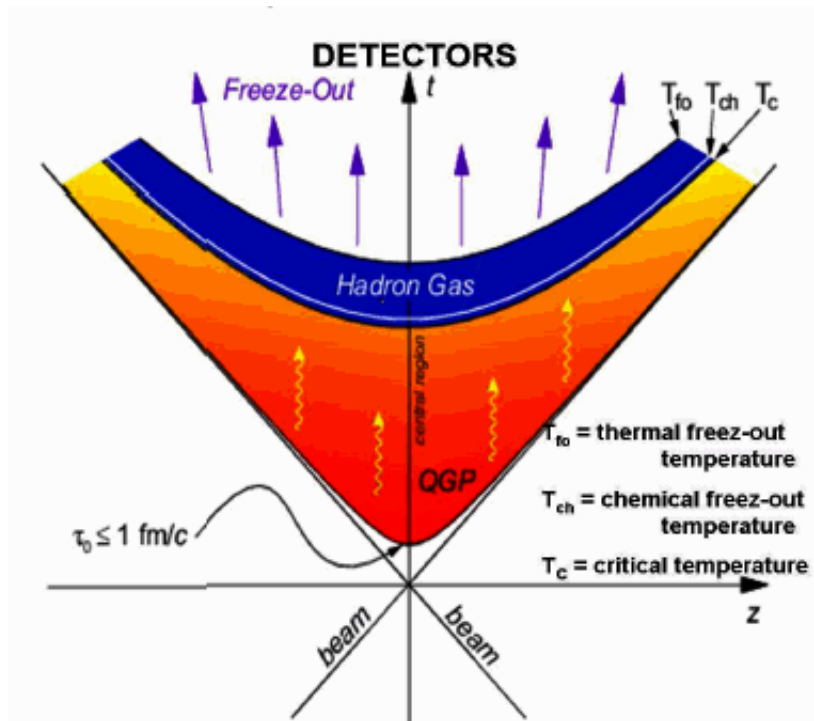


Figure 1.5: Space-time Evolution of a Heavy Ion Collision

Figure 1.5 illustrates the space-time evolution of a typical heavy ion collision. It can be described as two highly lorentz-contracted nuclei collide with each other in their moving directions mostly at the speed of light. At RHIC energies, they will penetrate



each other, unlike the case of "bounce off" at SPS energies. The initial stage ($\tau_0 < 1 \text{ fm}/c$) involves interactions of partons with very high momentum (i.e. hard partons). The creation of high p_T jets and $c\bar{c}$ pairs mainly occur at this stage because these processes need high momentum and energy transfer. With the evolution of interactions among partons, a state of deconfined quarks and gluons with chemical and (local) thermal equilibrium (i.e. QGP) [Ada05a] are formed. With the further evolution of the system, it cools down. Partons start to form hadrons (i.e. hadronization). The temperature, under which hadronization process starts is the critical temperature. As the system continue to cool down, the hadronization ceases and the relative ratios of different hadron species are fixed. The temperature at this stage is the chemical freeze-out temperature. As the system continue to expand, interactions between hadrons disappear. The corresponding temperature is the thermal freeze-out temperature (kinetic freeze-out temperature). The freeze-out hadrons move freely till they reach the detectors.

1.5 Theoretical Description of Heavy Ion Collisions

Due to complex nature of heavy ion collisions, no complete computable dynamical theories can describe the whole evolution of the heavy ion collisions. One theory (model) only can describe one or several stages of the system evolution and predict some features of experimental observables. Here, we have a brief review of different interesting theories/models.

1.5.1 pQCD Description

QCD is only calculable at sufficient high μ , where α_s is very small. When the coupling strength of interactions is small, physics quantities can be calculated by perturbative approach such as Leading Order (LO), Next-to-Leading Order (NLO). The cross section of a inclusive process $A + B \rightarrow C + X$ can be written as:



$$E_C \frac{d\sigma_{hard}^{AB \rightarrow C}}{d^3p} = K \sum_{abcd} \int dx_a dx_b f_{a/A}(x_a, Q_a^2) f_{b/B}(x_b, Q_b^2) \frac{d\sigma}{dt}(ab \rightarrow cd) \frac{D_{c/C}(z_c, Q_c^2)}{\pi z_c} \quad (1.4)$$

Factorization is assumed to make it possible to calculate the middle factor $\frac{d\sigma}{dt}(ab \rightarrow cd)$ in pQCD from Feynman diagrams. $x_a = p_a/p_A$ and $x_b = p_b/p_B$ are the initial momentum fraction of a hadron carried by the interacting parton. $z_c = p_C/p_c$ is the momentum fraction carried by the hadron fragmented from parton c . $f_{a/A}(x_a, Q_a^2)$ and $f_{b/B}(x_b, Q_b^2)$ are the Parton Distribution Function (PDF) in a hadron. $D_{c/C}(z_c, Q_c^2)$ is the Fragmentation Function (FF). The PDF and FF need calculation from models.

1.5.2 Hydrodynamics

For an extremely hot and dense system, a hydrodynamical formalism may be a natural description of its dynamics. The hydrodynamic equations of motion [Kol03a] are given by:

$$\partial_\mu T^{\mu\nu} = 0, T^{\mu\nu}(x) = u^\mu u^\nu (\epsilon + P) - g^{\mu\nu} P \quad (1.5)$$

$$\partial_\mu j_i^\mu = 0, j_i^\mu(x) = n_i u^\mu \quad (1.6)$$

where ϵ , P and n_i are the proper energy density, pressure and density of charge i in local rest frame, and u_μ is the four velocity. $T^{\mu\nu}$ is the energy-momentum tensor, j^μ is the charge current density. The equation of motion is derived from the local conservation of energy and momentum $\partial_\mu T^{\mu\nu} = 0$ and local charge conservation $\partial_\mu j^\mu = 0$.

The essential assumption is the thermal and chemical equilibrium (locally) reached in the applied system. For heavy-ion collisions, due to the dense nature, the interactions between the constituents (partons or hadrons) should be strong and frequent. If the time of the interactions is long enough, the system will reach (local) equilibrium. The initial condition is prior to the reach of (local) equilibrium. At the late hadronic stage of system evolution, the interaction rates are small and can not sustain the (local) thermal



equilibrium. So the hydrodynamics is only applicable in the middle possible QGP phase. The initial condition and hadronization need be modelled for a complete description of a collision. A sharp hadronization is modelled by the Cooper-Frye formula [Coo74a], which calculates the momentum distribution for hadrons created from the fluid elements on the freeze-out hyper-surface. Once modeling the hadronization is done, one can take advantage of the time evolution of hydrodynamics backward to estimate the initial conditions.

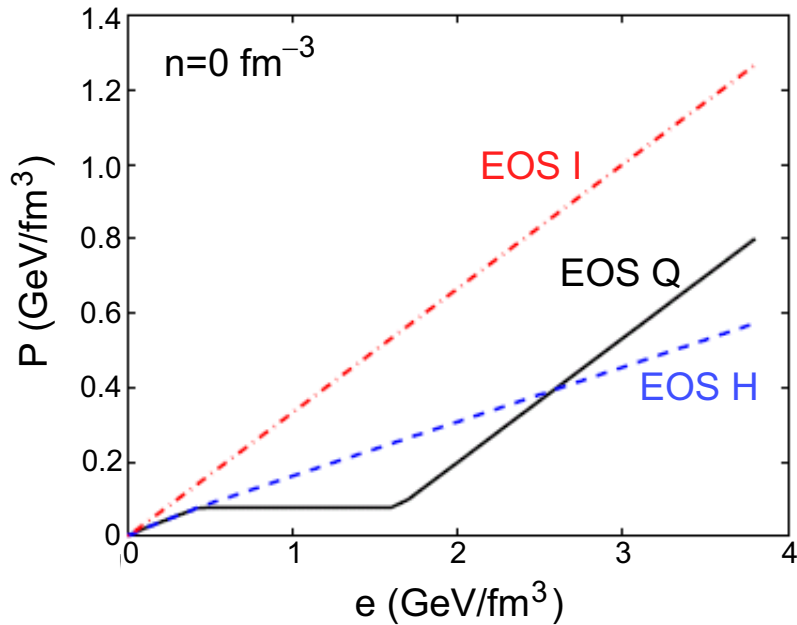


Figure 1.6: Pressure as a function of energy density at vanishing net baryon density for Equation-of-State of a Hagedorn resonance gas (EOS H), an ideal gas of massless partons (EOS I) and a connection of the two via a first-order transition at $T_c = 164$ MeV (EOS Q) [Kol03a].

With the equation of motion, the equation-of-state (EOS) need be modelled for calculation of the thermodynamic quantities of the system. Figure 1.6 shows the Equation of State from LQCD results. These EOS are used in hydrodynamic calculation in [Kol03a]. One example of EOS for a heavy ion collision is shown in solid line (EOS Q) connecting an ideal gas of massless partons at high temperature to a Hagedorn hadron resonance gas at low temperature via a first-order phase transition.



1.6 Experimental Observations

To search for the QGP in experiment, it is critical to begin by defining clearly what QGP mean for experimental aspects. QGP is taken to be a (locally) thermalized state of matter in which quarks and gluons are deconfined, so that color degrees of freedom become manifest over the nuclear, rather than merely nucleonic, volumes [Ada05a]. The thermalization and deconfinement are the two experimental concentrations to claim QGP formation. In particular, thermalization is viewed as a necessary condition to be dealing with a state of matter. In this section, we review some experimental probes and results.

1.6.1 Hard Probe: Jet Quenching

The dynamical processes that produce the bulk medium also produce energetic particles through hard scattering processes. The interactions of these energetic particles with the medium provide a class of unique, penetrating probes. The hard partons (jets) will interact with the medium and thus suffer energy loss. The amount of the energy loss should reflect the gluon density of the medium. The softened partons fragmenting into hadrons will lead to the suppression of high p_T hadrons in the final state compared to that of no medium effects ($p + p$ collisions). This effect is so called jet quenching [Wan92a, Wan98a, Wan05a]. For $p_T > 5$ GeV/c, the observed hadron spectra in Au + Au collisions at RHIC exhibit the power-law falloff in cross section with increasing p_T that is characteristic of perturbative QCD hard-scattering processes [Adl02a]. The nuclear modification factor is defined as

$$R_{AB}(p_T) = \frac{d^2 N^{AA}/dp_T d\eta}{T_{AB} d^2 \sigma^{pp}/dp_T d\eta} \quad (1.7)$$

where $d^2 N^{AA}/dp_T d\eta$ is the differential yield in A + B collisions, $d^2 \sigma^{pp}/dp_T d\eta$ is the measured differential cross section for $p + p$ inelastic collisions. To compare two collisions, $T_{AB} = \langle N_{bin} \rangle / \sigma_{inelastic}^{pp}$, where $\langle N_{Bin} \rangle$ is the mean number of binary nucleon-nucleon collisions, is introduced to account for the nuclear geometry. R_{AB} is equal to



unit if $A + B$ collision is a simple superposition of $p + p$ collisions.

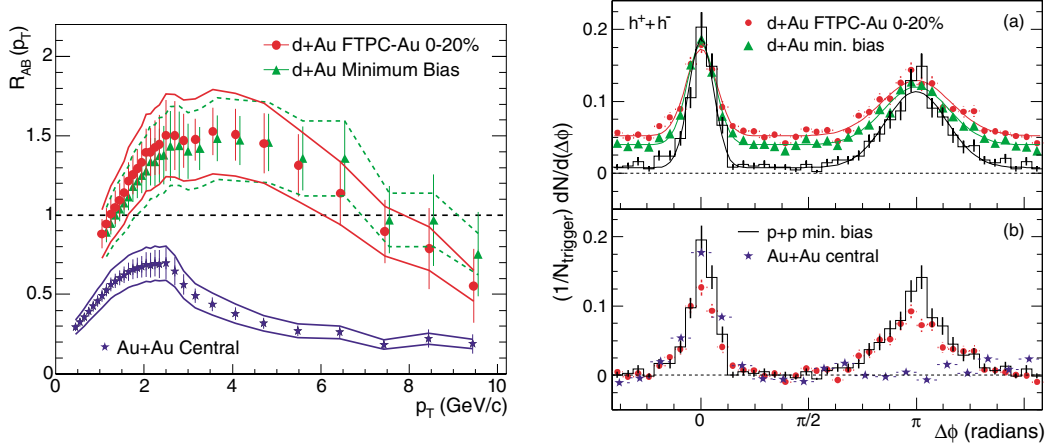


Figure 1.7: Left Panel: $R_{AB}(p_T)$ for minimum bias and central $d + Au$ collisions, and central $Au + Au$ collisions. The minimum bias $d + Au$ collisions data are displaced 100 MeV/c to the right for clarity. The bands show the normalization uncertainties, which are highly correlated point-to-point and between the two $d + Au$ distributions. Right Panel: (a) Efficiency corrected two-particle azimuthal distributions for minimum bias and central $d + Au$ collisions, and for $p + p$ collisions. (b) Comparison of two-particle azimuthal distributions for central $d + Au$ collisions to those seen in $p + p$ and $Au + Au$ collisions. The respective pedestals have been subtracted. The figure is from [Ada03b]

Left panel in Figure 1.7 shows R_{AB} as a function of p_T for $Au + Au$ and $d + Au$ collisions. Large p_T hadrons in central $Au + Au$ collisions are suppressed by a factor of 5 relative to naive binary scaling expectations. High p_T hadron suppression is not observed in $d + Au$ collisions. This is an evidence that nuclear effects, such as nuclear shadowing of parton distribution functions and initial state multiple scattering can not account for the suppression. Further, the energy lose is expected to depend on the length of the path, which partons travel. The parton near the surface can penetrate the medium while the back-to-back produced parton will go through the significant length in dense matter and lose most of its energies into the medium thus can not be observed. Right panel in Figure 1.7 shows the azimuthal distribution of hadrons with $p_T > 2$ GeV/c relative to a trigger hadron with $p_T^{trig} > 4$ GeV/c. A hadron pair from a single jet will generate the near-side correlation ($\Delta\phi \approx 0$) as observed in $p + p$, $d + Au$ and $Au + Au$ collisions. A hadron pair from back-to-back di-jets will generate the away-side



correlation ($\Delta\phi \approx \pi$) as observed in $p + p$ and $d + \text{Au}$ collisions. The significant disappearance of back-to-back correlation is observed in central $\text{Au} + \text{Au}$ collisions. These results provide experimental evidence that the hot and dense medium has been formed at RHIC.

1.6.2 Bulk Properties and Collective Dynamics

The properties of bulk matter created in collisions can be studied via multiplicities, yields, momentum spectra, especially at low p_T , where most of particles are produced. Due to the dynamical origin and evolution of the bulk matter, information on its degree of thermalization and its Equation of State related to the QGP formation are expected to be obtained.

1.6.2.1 Hadron Yield and Chemical Freeze-out

In heavy ion collisions, inelastic collisions cease at chemical freeze-out and the abundance of the chemical elements become fixed. The measured yields for different hadron species can provide information on the properties of the bulk matter at chemical freeze-out. Thermal model, assuming chemical and thermal equilibrium, is used to extract chemical freeze-out information such as chemical freeze-out temperature T_{ch} , baryon chemical potential μ_B and strangeness suppression factor γ_s [Bra03a, Hwa03a, Hua88a].

Figure 1.8 shows p_T integrated particle yield ratios for various hadron species in central $\text{Au} + \text{Au}$ collisions at $\sqrt{s_{NN}} = 200$ GeV measured by the STAR experiment. The thermal model fit to the data is shown by horizontal lines. From the fit, the chemical freeze-out temperature is 163 ± 4 MeV, and the baryon chemical potential is 24 ± 4 MeV. The thermal model fits well for stable and long-lived hadrons through multi-strange baryons. The deviations for the short-lived resonance yields, such as for Λ^* and K^* from the fits, presumably result from hadronic re-scatterings after chemical freeze-out. The inset in Figure 1.8 shows the strangeness suppression factor γ_s [Xu02a] as a function of number of participants. γ_s reflects how far a system is from chemical equilibrium. γ_s increases from 0.75 in peripheral $\text{Au} + \text{Au}$ collisions to 0.99 in central



Au + Au collisions. γ_s consistent with unity for central collisions strongly indicates that the chemical equilibrium has been reached in central collisions at RHIC.

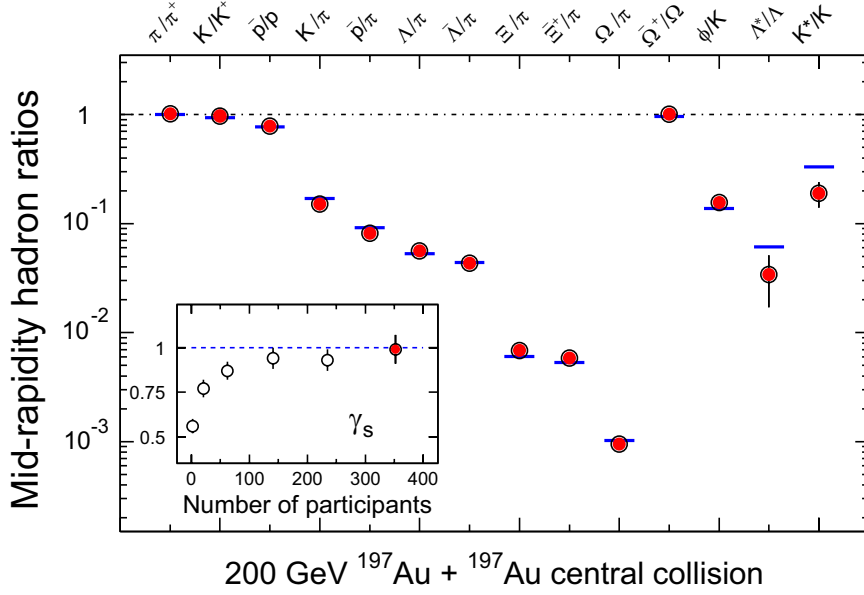


Figure 1.8: Ratios of p_T -integrated mid-rapidity yields for different hadron species for central Au + Au collisions at $\sqrt{s_{NN}} = 200$ GeV measured by STAR. The horizontal bars represent thermal model fits to the measured yield ratios. The fit parameters are $T_{ch} = 163 \pm 4$ MeV, $\mu_B = 24 \pm 4$ MeV, $\gamma_s = 0.99 \pm 0.07$ [Bar04a]. The inset shows the variation of γ_s with number of participants, including the value (leftmost point) from fits to yield ratios for 200 GeV $p + p$ collisions measured by STAR.

1.6.2.2 Spectra and Kinetic Freeze-out

The elastic collisions do not cease after chemical freeze-out until the kinetic or thermal freeze-out. The measurements of hadron transverse momentum spectra can provide information on the characteristics of the system at kinetic freezeout. In order to characterize the transverse expansion of the system, the hydrodynamics-motivated fit [Sch93a] to the spectra has been used to extract the random motion component and the collective motion component, which is respectively described by the fit parameter kinetic freeze-out temperature T_{fo} and radial flow collective velocity $\langle\beta_T\rangle$.

Figure 1.9 shows T_{fo} and $\langle\beta_T\rangle$ as a function of centrality from STAR experiment.



For the copiously produced particles π , K and p , the extracted T_{fo} becomes smaller and smaller as the collisions appear more and more central, while the extracted $\langle\beta_T\rangle$ becomes larger and larger. This indicates that the system created in central collisions grows cooler and develops stronger flow than peripheral collisions. Compared to $p + p$ collisions, most peripheral centrality bin has the similar T_{fo} but smaller $\langle\beta_T\rangle$. On the other hand, for most central collisions, the multi-strange particles ϕ and Ω appear to manifest a higher freeze-out temperature and lower radial flow velocity than π , K and p . Their freeze-out temperature is close to the chemical freeze-out temperature. ϕ and Ω are suggested to have small hadronic interactions with the expanding matter after chemical freeze-out [Ada04a, Bar04a, Bra95a, Bra99a, Bas99b]. If this is true, the radial flow velocity of ϕ and Ω have to be accumulative prior to the chemical freezeout, making them particularly sensitive to the early partonic stage in the system evolution.

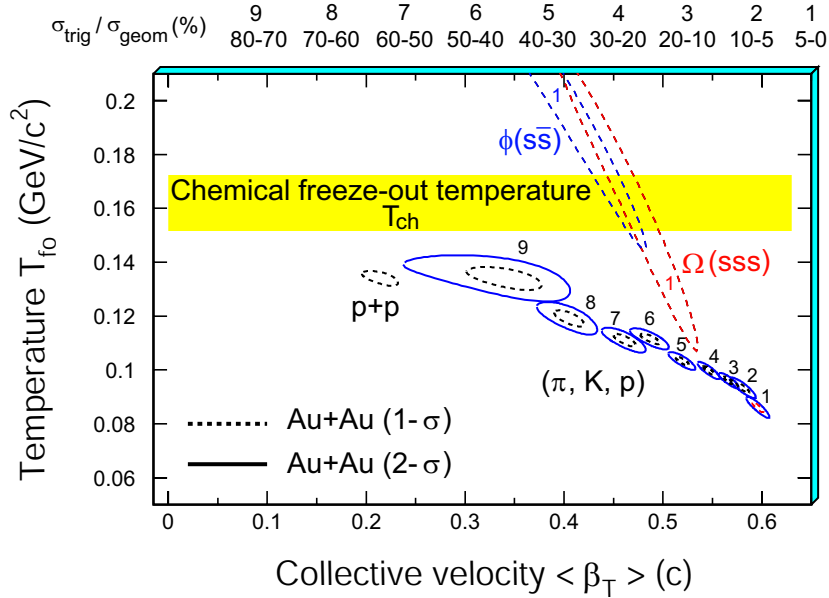


Figure 1.9: The χ^2 contours for T_{fo} and $\langle\beta_T\rangle$ extracted from thermal + radial flow fits to π , K , p together in 9 centrality bins from top 5% to 70%-80% for Au + Au collisions at $\sqrt{s_{NN}} = 200$ GeV and for $p + p$ collisions at $\sqrt{s_{NN}} = 200$ GeV. The results for ϕ and Ω are shown only for most central Au + Au collisions at $\sqrt{s_{NN}} = 200$ GeV. Dashed and solid lines are the 1σ and 2σ contours, respectively. The figure is from [Ada05a].



1.6.2.3 Collective Flow

The transverse momentum distribution of different particles reflects a random and collective component. The random component can be identified with the temperature of the system at kinetic freeze-out. Collective component has its origin of the matter density gradient from the center to the boundary of the fireball created in mid-rapidity. Interactions between constituents push the matter outwards: frequent interactions will lead to a common velocity distribution. Thus *Collective flow* is sensitive to the strength of interactions and degrees of freedom. Collectivity is defined as all particles moving with a common velocity.

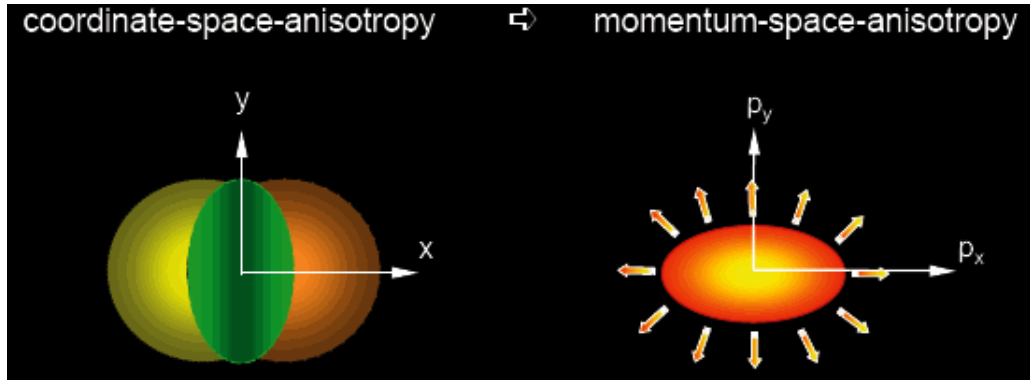


Figure 1.10: Azimuthal anisotropy in coordinate space and momentum space with respect to the reaction plane determined from the impact parameter and z (beam) directions.

The reaction plane is determined by the impact parameter and beam (z) directions. The azimuthal anisotropy of transverse momentum distribution is well studied with respect to the reaction plane illustrated in Figure 1.10 since the initial spatial anisotropy has its almond shape with respect to the reaction plane.

In spatial coordinate, the length in x direction is shorter than that in y direction, shown in left cartoon of Figure 1.10. This results in larger density gradient in x direction than in y direction, which is shown in Figure 1.11 with projection of all particles on one dimension (x or y direction). The area under the density variation curves in x direction and in y direction is the same, which is equal to total number of particles. Through frequent interactions among particles, the larger density gradient in x direction leads to the larger pressure gradient than in y direction. The larger pressure gradient further

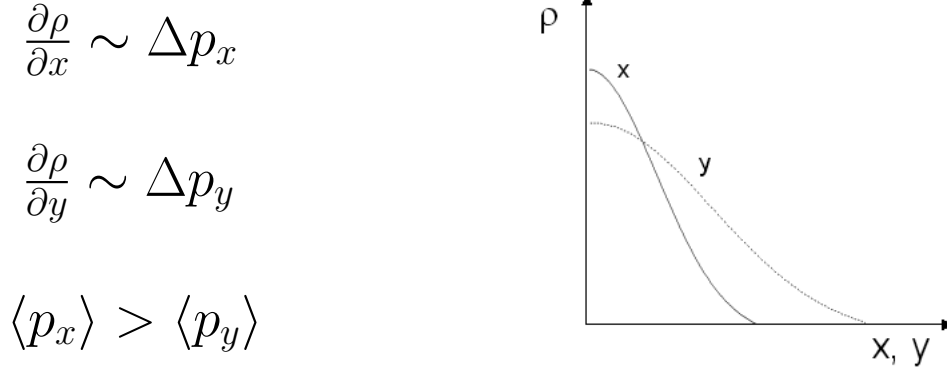


Figure 1.11: A sketch map of initial particle density in x and y direction.

leads to larger collective flow velocity. The momentum space azimuthal anisotropy results from azimuthal anisotropy of collective flow velocity, which is shown in right cartoon of Figure 1.10. The initial spatial anisotropy will be washed out by the momentum space anisotropy during the system expansion, so this self-quenching effect makes anisotropic flow sensitive to the early stage [Sor97a].



Figure 1.12: Two components of hydrodynamic flow.

Due to the dense and hot nature of created medium, hydrodynamics is expected to be a good description of collective flow effect in heavy ion collisions. The hydrodynamical flow is expected to be separated into two components: collectivity and (local) thermalization, which is shown in Figure 1.12. The development of collectivity only need the pressure gradient. The pressure gradient only depend on the density gradient and interactions among particles. No thermalization is needed. If the interactions are enough, local thermalization may be reached. Thus random and collective components can not be fully separated, which is represented by the cross product between them in Figure 1.12.



1.6.2.4 Elliptic Flow and Results

Here, we introduce the experimental flow observables.

In non-central Au + Au collisions, the initial spatial anisotropy in the reaction region is characterized by the eccentricity defined by:

$$\varepsilon = \frac{\langle y^2 - x^2 \rangle}{\langle y^2 + x^2 \rangle} \quad (1.8)$$

where x and y are the spatial coordinates in overlapping region.

The anisotropic flow can be studied by the Fourier expansion [Oll92a, Oll93a, Vol96a] of azimuthal angle distribution of produced particles with respect to the reaction plane:

$$E \frac{d^3 N}{d^3 p} = \frac{1}{2\pi} \frac{d^2 N}{p_T dp_T dy} \left(1 + \sum_{n=1}^{\infty} 2v_n \cos[n(\phi - \Psi_r)] \right) \quad (1.9)$$

where p_T and y are the transverse momentum and rapidity of a particle, ϕ is its azimuthal angle, v_n is the n th harmonic coefficient and Ψ_r is the azimuthal angle of the reaction plane. The different harmonic coefficients represent different aspects of the global flow behavior. v_1 is so called directed flow and v_2 is so called elliptic flow since it is the largest component characterizing the ellipse shape of the azimuthal anisotropy. Equivalently, v_2 can be calculated by:

$$v_2 = \left\langle \frac{p_x^2 - p_y^2}{p_x^2 + p_y^2} \right\rangle \quad (1.10)$$

The experimental evidence of the system reaching (local) thermalization is required to claim the QGP formation. Recently, reference [Vol00a] suggests centrality dependence of elliptic flow can measure whether the system has reached the thermal equilibrium. The argument is based on two limits: in the hydro limit, which has complete thermalization, the centrality dependence of elliptic flow is mostly defined by the eccentricity. 2. in the low density limit, where dynamical thermalization is not expected, elliptic flow is proportional to the eccentricity and the initial particle density.

Figure 1.13 shows charge particle v_2/ε as a function of $\frac{1}{S} dN_{ch}/dy$, where S is the



area of the overlapping zone, thus $\frac{1}{S}dN_{ch}/dy$ is the measured particle density in mid-rapidity. At RHIC energies, STAR measurements are presented for Au + Au and Cu + Cu collisions at both 62.4 GeV and 200 GeV. At SPS energies, NA49 measurements are presented for Pb + Pb collisions at 40A GeV and 158A GeV. At AGS energies, E877 measurements is shown for Au + Au at 11.8A GeV. v_2/ε increases with $\frac{1}{S}dN_{ch}/dy$. The particle density $\frac{1}{S}dN_{ch}/dy$ defines the re-scattering probability among constituents. In more central collisions, there are more frequent interactions among constituents. This increase in v_2/ε indicates the system created in heavy ion collisions evolves towards the thermalization in central collisions.

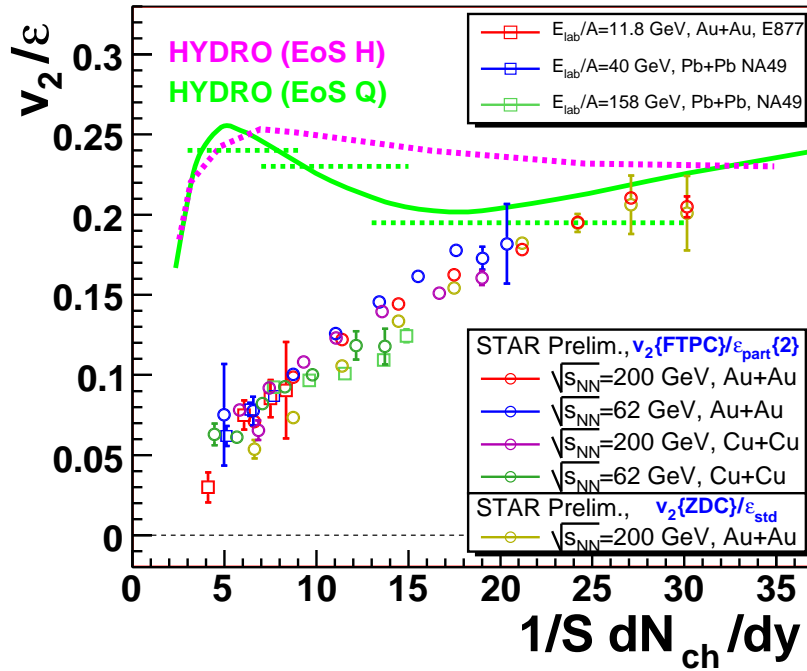


Figure 1.13: Charge particle v_2/ε versus $\frac{1}{S}dN/dy$ from AGS, SPS to RHIC energies. The figure is from [Vol06a]

Figure 1.14 shows the measured low- p_T v_2 distribution from minimum bias in Au + Au collisions at $\sqrt{s_{NN}} = 200$ GeV from STAR and PHENIX experiments. Identified particle v_2 are shown for π^\pm , K_S^0 , \bar{p} ($p + \bar{p}$) and $\Lambda + \bar{\Lambda}$. Up to 1.6 GeV/c, at a given p_T , the heavier particle has the smaller v_2 than the lighter particle. This characteristic mass-ordering is predicted by the hydrodynamic calculation represented by the dot-dashed



lines. This indicates the collectivity has been developed at RHIC. In this hydrodynamic calculation [Huo01a, Huo03a], the critical temperature is 165 MeV and the freeze-out temperature is 130 MeV. The absolute magnitude of v_2 is well produced as the parameters of the hydrodynamics calculations have been tuned to achieve good agreement with data. In particular, since the parameters are tuned for zero impact parameter while data is measured for minimum bias, the comparison for v_2 between the theory and the experiment should test hydrodynamical calculations as a function of centrality. This is especially a critical test in assessing QGP claims since the hydrodynamical calculations assume local thermalization while the system is most likely to reach thermalization in central collisions.

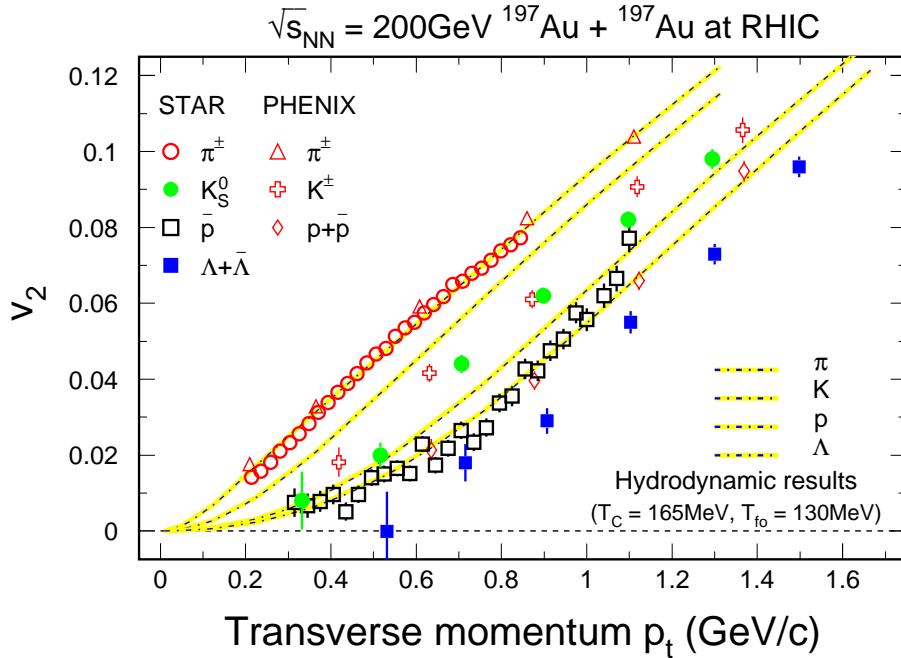


Figure 1.14: minimum bias $v_2(p_T)$ results from the STAR and PHENIX experiments for π^\pm , K_S^0 , \bar{p} ($p + \bar{p}$) and $\Lambda + \bar{\Lambda}$ up to 1.6 GeV/c. Hydrodynamics calculation [Huo01a, Huo03a] assuming early thermalization, ideal fluid expansion, an equation of state from LQCD calculation including a phase transition at $T_c = 165$ MeV and a sharp kinetic freeze-out with $T_{fo} = 130$ MeV (EOS Q in [Kol03a] and Figure 1.6), are shown as dot-dashed lines. The figure is from [Old04a]



Figure 1.15 shows elliptic flow results at intermediate p_T for minimum bias in Au + Au collisions at $\sqrt{s_{NN}} = 200$ GeV. Panel (a) and (b) show v_2 as a function of p_T for K_S^0 and $\Lambda + \bar{\Lambda}$ up to 6 GeV. Multi-strange baryon $\Xi + \bar{\Xi}$ and $\Omega + \bar{\Omega}$ are shown in (a) and (b), respectively. Hydrodynamics calculations [Huo01a] are indicated by dotted curves. At intermediate p_T , v_2 values deviate from hydrodynamic calculations and then saturate. Baryons saturate with higher v_2 value at higher p_T value than mesons. The dot-dashed curves in Figure 1.15 (a) and (b) represent simple analytical function fits to K_S^0 and $\Lambda + \bar{\Lambda}$ v_2 . The saturated v_2 of K_S^0 and $\Lambda + \bar{\Lambda}$ is independent on p_T up to 6 GeV with larger statistical uncertainties. The multi-strange baryon $\Xi + \bar{\Xi}$ and $\Omega + \bar{\Omega}$ are consistent with that of $\Lambda + \bar{\Lambda}$ within still sizable statistical uncertainties. Multi-strange baryons are suggested to have small hadronic cross section [Bar04a, Bra95a, Bra99a, Bas99b]. If this interpretation is correct, the development of their substantial v_2 must be accumulated at early partonic stage. Their v_2 consistent with the hydro-like mass ordering, indicates that partonic collectivity has been developed at RHIC.

Both v_2 and p_T scaled by the number of constituent quarks n_q are shown in Figure 1.15 (c) for all particles in Figure 1.15 (a) and (b), together with π and $p + \bar{p}$. For mesons, n_q is equal to 2 while for baryons, n_q is equal to 3. For $n_q > 1$ GeV/c, all particles follow a universal curve. This is so called Number of Constituent Quark (NCQ) scaling. This scaling itself seem to point to constituent quarks as the most effect degree of freedom in determining hadron flow at intermediate p_T . The data need to be improved in statistical precision and p_T extent for more identified mesons and baryons in order to establish this scaling more definitively.

Quark recombination/coalescence models [Fri03a, Gre03a, Lin02a, Vol02a] assume that the constituent quarks carry its v_2 by themselves, before they start to form hadrons. The hadron v_2 is developed by recombining constituent quarks into hadrons (i.e. hadronization). These models can roughly explain the NQ scaling. This suggests that the system has been in the deconfined state prior to hadronization.

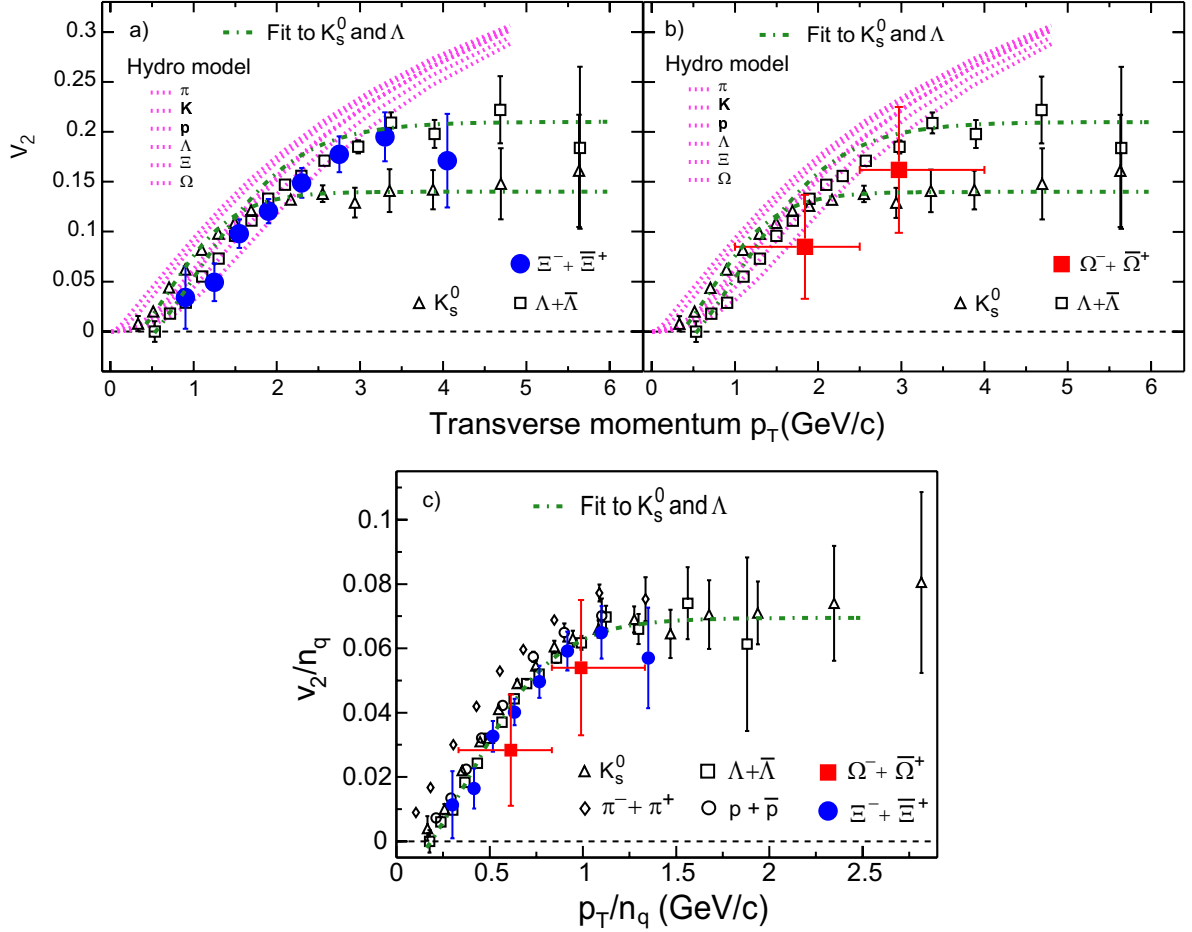


Figure 1.15: (a) and (b): transverse momentum dependence of elliptic flow for various hadron species in minimum bias Au + Au collisions at $\sqrt{s_{NN}} = 200$ GeV. STAR results [Ada04b] for K_S^0 and $\Lambda + \bar{\Lambda}$ are shown in both panels, together with a simple analytic function fits (dot-dashed lines). STAR multi-strange baryon results for $\Xi + \bar{\Xi}$ and $\Omega + \bar{\Omega}$ are shown in (a) and (b), respectively. Hydrodynamics calculations are indicated by dotted curves. (c): both v_2 and p_T scaled by the number of constituent quarks (n_q) in each hadron. Additionally, PHENIX results for π and $p + \bar{p}$ are shown together with STAR results in (a) and (b). The figure is from [Ada05a]



1.7 Centrality Dependence of v_2 Measurements

Recently, discussions on deconfinement, thermalization and partonic collectivity from v_2 results have been focused on either identified particles for minimum bias or integrated v_2 for charge particles. A systematic comparison for identified hadrons at different centrality bins are still scarce. In this thesis, we present centrality dependence of v_2 measurements for K_S^0 and $\Lambda + \bar{\Lambda}$ in Au + Au collisions at $\sqrt{s_{NN}} = 200$ GeV. Systematic study for identified hadron v_2 will gain information on interplay of collectivity, NQ scaling and thermalization as a function of collision centralities. This will help us to determine parameters for partonic EoS.

This thesis is organized as following. Chapter 2 will review the facilities used to study heavy-ion collisions. The Relativistic Heavy Ion Collider and its programs will be discussed. The STAR detector system will be discussed in more details. Chapter 3 includes analysis methods. Techniques for measuring K_S^0 and Λ v_2 and different flow methods will be discussed. Chapter 4 will present the results of this analysis. Chapter 5 will stimulate discussions on centrality dependence of v_2 measurements. Chapter 6 will give summary and outlook.



CHAPTER 2

Experimental Setup

2.1 History of Heavy Ion Accelerator Facilities

The first facility to accelerate ion beams is BEVALAC made at Lawrence Berkeley National Laboratory, which accelerate ion beams energies up to 2 AGeV. It starts the study on relativistic heavy ion collisions. The high-energy physics researches have been driving the accelerator to higher energies. The Alternating Gradient Synchrotron (AGS) at the Brookhaven National Laboratory (BNL) provided gold beams up to an energy of 11.7 AGeV and allowed gold-on-gold collisions at center of mass energies per nucleon pair from $\sqrt{s_{NN}} = 2.68$ GeV to $\sqrt{s_{NN}} = 4.75$ GeV. The Super Proton Synchrotron (SPS) at CERN can accelerate lead ion beams up to an energy of 158 AGeV and lead-on-lead collisions up to $\sqrt{s_{NN}} = 17.3$ GeV. A new accelerator is planned to be built at GSI. It is designed to accelerate Uranium beams up to an energy of about 20 AGeV.

The Relativistic Heavy-Ion Collider (RHIC) is a heavy-ion collider located and operated by the Brookhaven National Laboratory (BNL) in Upton, New York. RHIC is the first facility designed to collide the heavy-ion beams. The top energy at RHIC is $\sqrt{s_{NN}} = 200$ GeV for gold beams and higher energy for lighter beams. The next large collider in development is the Large Hadron Collider (LHC) at CERN. It is originally designed for proton-on-proton collisions up to an energy of 14 TeV and lead-on-lead collisions up to $\sqrt{s_{NN}} = 5.5$ TeV.



2.2 The Relativistic Heavy-Ion Collider

The RHIC collider consists of two quasi-circular concentric accelerator/storage rings on a common horizontal plane, one ("Blue Ring") for clockwise and the other ("Yellow Ring") for the counter-clockwise beams. Bending and focusing of ion beams are achieved by the ring super-conducting magnets. The counter-rotating beams can collide with one another at six location along their 3.8 km circumference. The two independent rings and two sources of ions make a various collisions possible, such as equal ion species from $\text{Au} + \text{Au}$ to $p + p$, unequal ion species of protons on gold ions or light ions on gold. The basic design parameters of the collider are shown in Table 2.1. The top energy for heavy ion beams is 100 GeV/u. The operational momentum increases with the charge-to-mass ratio, resulting in the top energy of 125 GeV/u for lighter ion beams and 250 GeV/u for proton beams. The average luminosity for gold-on-gold collisions at $\sqrt{s_{NN}} = 200$ GeV is $8 \times 10^{26} \text{ cm}^{-2}\text{s}^{-1}$ without electron cooling and $7 \times 10^{27} \text{ cm}^{-2}\text{s}^{-1}$ with electron cooling. The average luminosity for proton-on-proton collisions at 250 GeV is $2.4 \times 10^{32} \text{ cm}^{-2}\text{s}^{-1}$ without electron cooling and $8 \times 10^{32} \text{ cm}^{-2}\text{s}^{-1}$ with electron cooling.

	Au + Au
Top beam energy	100 GeV/u
Nominal luminosity	$1 \times 10^{26} \text{ cm}^{-2}\text{s}^{-1}$
RHIC II luminosity	$8 \times 10^{26} \text{ cm}^{-2}\text{s}^{-1}$
Luminosity lifetime	10 hours
Number of bunches/ring	60

Table 2.1: RHIC performance parameters

The RHIC acceleration scenario is shown in Fig. 2.1. Three accelerators in the injector chain will successively boost the energy of ions, and strip electrons from the atoms. Negatively charge gold ions from the ion source at the Tandem Van de Graaff are partially stripped of their electrons with a foil, and then accelerated to the energy of 1 MeV/u by the seconde stage of the Tandem. After further stripping at the exit of the Tandem and a charge selection by bending magnets, beams of gold ions with the



charge state of $+32e$ are delivered to the Booster Synchrotron and accelerated to 95 MeV/u. Ions are stripped again at the exit of the Booster Synchrotron to reach the charge state of $+77e$, and injected into the Alternating Gradient Synchrotron (AGS) for acceleration to the RHIC injection energy of 10.8 GeV/u. The beams are transferred to RHIC through the AGS-to-RHIC Beam Transfer Line. Gold ions are fully stripped to the charge state of $+79e$ at the exit of the AGS. Finally, beams are accelerated to the top energy at RHIC.

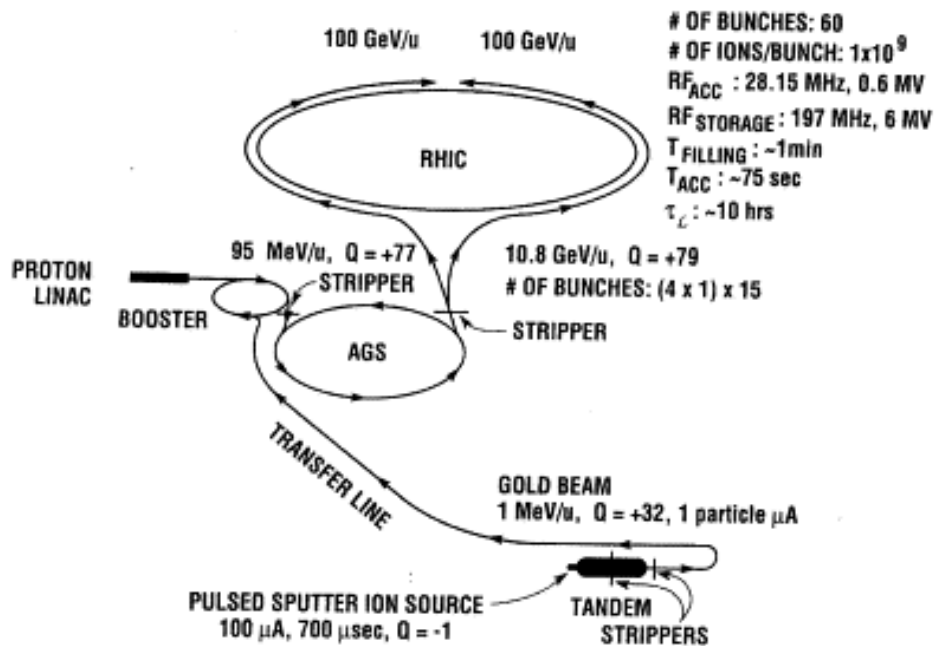


Figure 2.1: A diagram of the Relativistic Heavy-Ion collider complex at the Brookhaven National Laboratory including the facilities that accelerate the gold ions up to the RHIC injection energy.

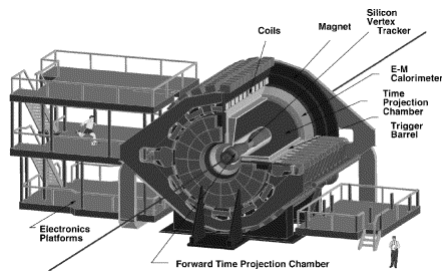
Acceleration and storage of beam bunches at RHIC use two Radio Frequency (RF) system. One operating at 28 MHz is used to capture the AGS bunches and accelerate to the top energy. The other operating at 197 MHz is used to store the beam, which is transferred from the acceleration RF system. The storage RF system shorten the bunches and store the beam for 10 hours.



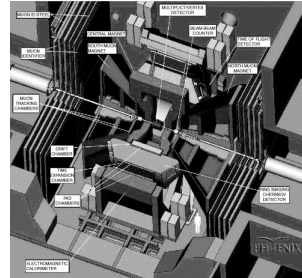
2.3 RHIC Experiments

There are four experimental programs at RHIC: STAR collaboration located at 6 o'clock position, PHENIX collaboration located at 8 o'clock position, PHOBOS collaboration located at 10 o'clock position, BRAHMS collaboration located at 2 o'clock position. Figure 2.2 shows the global view of STAR, PHENIX, PHOBOS and BRAHMS detectors.

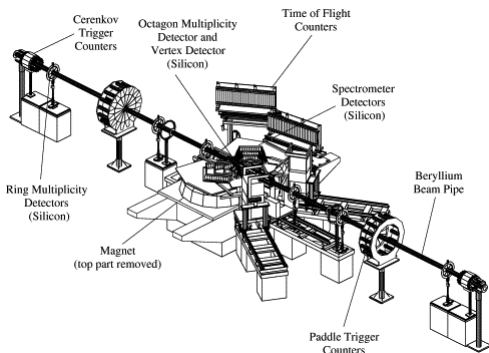
STAR experiment [Ack03a] is designed to focus on global event reconstruction, resonance identification, event-by-event variables and fluctuations with full azimuthal acceptance. A large solenoidal tracking detector covers the full azimuthal angle $0 < \phi < 2\pi$. Subsystems include a main TPC covering $|\eta| < 1.3$, two forward TPCs covering $2.5 < |\eta| < 4$ and others such as, silicon vertex tracker, electromagnetic calorimeter, time of flight.



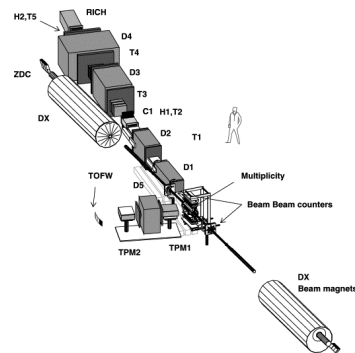
STAR detector



PHENIX detector



PHOBOS detector



BRAHMS detector

Figure 2.2: Global view of STAR detector, PHENIX detector, PHOBOS detector and BRAHMS detector at RHIC.

PHENIX experiment [Adc03a] is designed to focus on rare probes, hadron identifica-



tion and electron identification with smaller acceptance and faster detectors. A central spectrometer with two arms and tracking sub-system, each subtends $\pi/2$ radians and covers $|\eta| < 0.35$. It is used to measure electrons, hadrons and photons at mid-rapidity. Two forward muon spectrometers covers $1.1 < |\eta| < 2.4$ and azimuthal angle $0 < \phi < 2\pi$. They are used to measure muons at forward rapidity.

BRAHMS experiment [Ada03a] is designed to measure charge hadrons over the widest possible range of rapidity and transverse momentum ($0 < Y < 4$, $0.2 < p_T < 3.0 \text{ GeV}/c$) with two small solid-angle spectrometers.

PHOBOS experiment [Bac03a] is designed to detect charge particles over the full solid angle using a multiplicity detector and measure identified charge particles near mid-rapidity in two spectrometers arms.

2.4 STAR Detector Systems

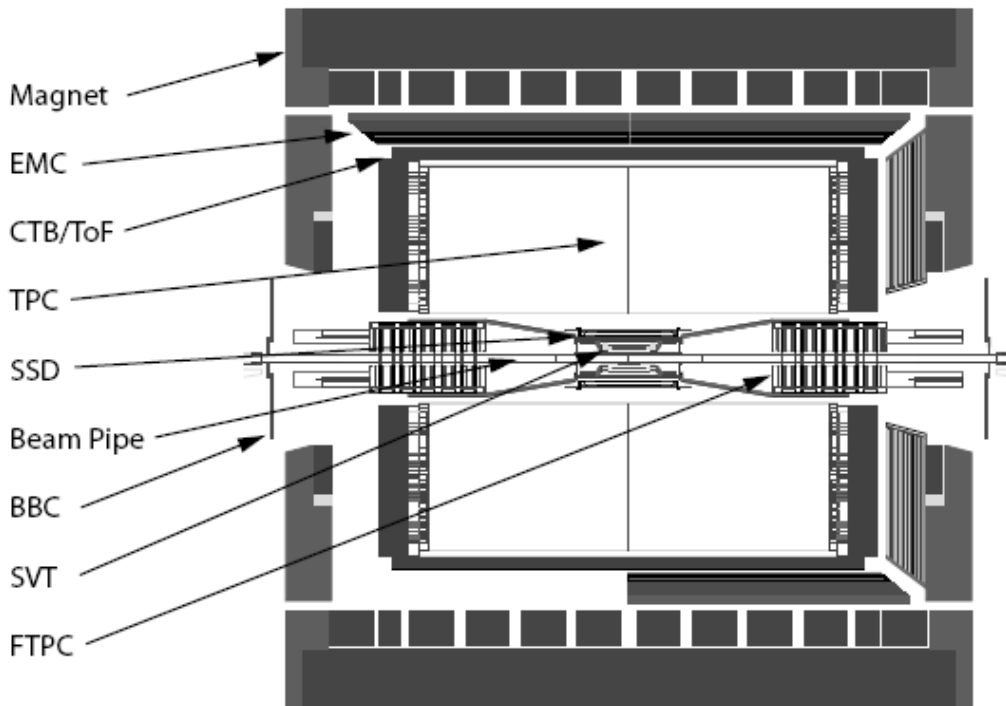


Figure 2.3: Cutaway side view of the STAR detector as configured in 2004



To search for signatures of Quark Gluon Plasma (QGP), the Solenoidal Tracker At RHIC (STAR) was constructed for measurements of hadron production over a large solid angle with high precision momentum. It is particularly suitable to measure event-by-event fluctuations, correlations and jets. Particle identification provides the possibility to study those observables for different particle species and identified particle spectra.

A cutaway side view of the STAR detector as configured for the RHIC 2004 run is displayed in Figure 2.3. The STAR detector consists of several subsystems, which integrate to the whole functionality of the detector. The STAR detector sits in a large solenoidal magnet with a uniform magnitude 0.25 or 0.5 Tesla [Ber03a]. The beam is surrounded by the beam pipe [Mat03a]. Its material, Beryllium with low density and low nuclear charge is chosen to minimize the number of photon conversions and multiple scattering of particles traversing the beam pipe. The main tracking detector in STAR is the Time Projection Chamber (TPC) [And03a], which provides symmetric tracking information with coverage $|\eta| < 1.8$. To extend the tracking to the forward region, a radial-drift TPC (FTPC) [Ack03b] is installed covering $2.5 < |\eta| < 4$ with complete azimuthal coverage and symmetry. The Silicon Vertex Tracker (SVT) [Bel03a] supplements tracking information provided by the TPC for precise location of primary vertex and secondary vertex of the weak decay that move from the primary vertex before decaying into charge particles. The Silicon Strip Detector (SSD) [Arn03a] completes the intermediate trackers and improves the extrapolation of TPC tracks through SVT hits with good hit position resolution. A full-barrel electromagnetic calorimeter (EMC) and the end-cap calorimeter located on the west side [Bed03a, All03a], provide capability of photon and electron identification. Measurements of the spatial distribution of photons within $2.5 < \eta < 3.5$ is also provided by the Photon Multiplicity Detector (PMD) [Agg03a]. Time-of-Flight based on Multi-gap Resistive Plate Chamber (TOFr) [Bon03a] extends TPC capability of particle identification. It covers $-1 < \eta < 0$ and $\pi/30$ in azimuth.

The STAR trigger system [Bei03a] is based on input from fast detectors to control the event selection for the much slower tracking detectors. The Central Trigger Barrel (CTB) at $|\eta| < 1$ and Zero Degree Calorimeters (ZDC) located in the forward direction

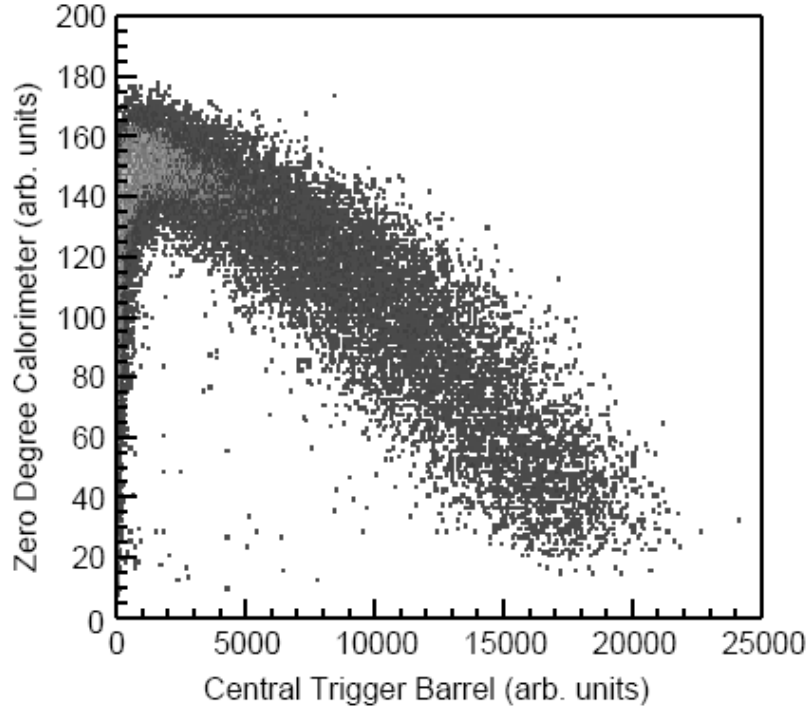


Figure 2.4: Correlation between the summed pulse heights from the ZDC and the CTB for events with a primary collision vertex reconstructed from tracks in the TPC.

at $\theta < 2$ mrad, provide input to the trigger system. The CTB surrounds the outer cylinder of the TPC, and determines the flux of charge particles in the mid-rapidity region. The ZDCs determine the energy in neutral particles remaining in the forward direction. The correlations between ZDC pulse height and that of the CTB shown in Figure 2.4 is a monotonic function, which is used in experiment to provide a trigger for centrality of the collision. Peripheral collisions characteristically leave a large amount of energy in forward direction into the ZDC and a small amount of energy and particles sideward into the CTB. Central collisions leave less energy into ZDC and more energy and particles into the CTB. The largest number of events occurs for large ZDC values and small CTB values, which is corresponding to the peripheral collisions. A minimum bias trigger requires at least one neutron in each of the forward ZDCs, which corresponds to 95% of the geometrical cross-section. Central triggers further require less energy in ZDCs and sufficient CTB signals to reduce the second branch at low CTB values shown in Figure 2.4.

Future upgrades of STAR detectors are under development to expand the detection



capabilities and physics program. TOF upgrade will provide full azimuthal coverage and two units in pseudo-rapidity $-1.0 < \eta < 1.0$. This allows STAR to extend capability of particle identification over full acceptance and TPC pseudo-rapidity coverage. It will benefit detailed and precise measurement of observables such as correlations and fluctuations. Heavy Flavor Tracker (HFT) [Wie06a] is proposed to extend STAR's capability to measure displaced vertices very close to the primary vertex, namely direct reconstruction of open charm states such as D meson. Measurement of D meson v_2 will gain information on the thermalization among u , d , s quarks. Measurement of D meson R_{AA} will test heavy flavor energy loss.

2.5 STAR Time Projection Chamber

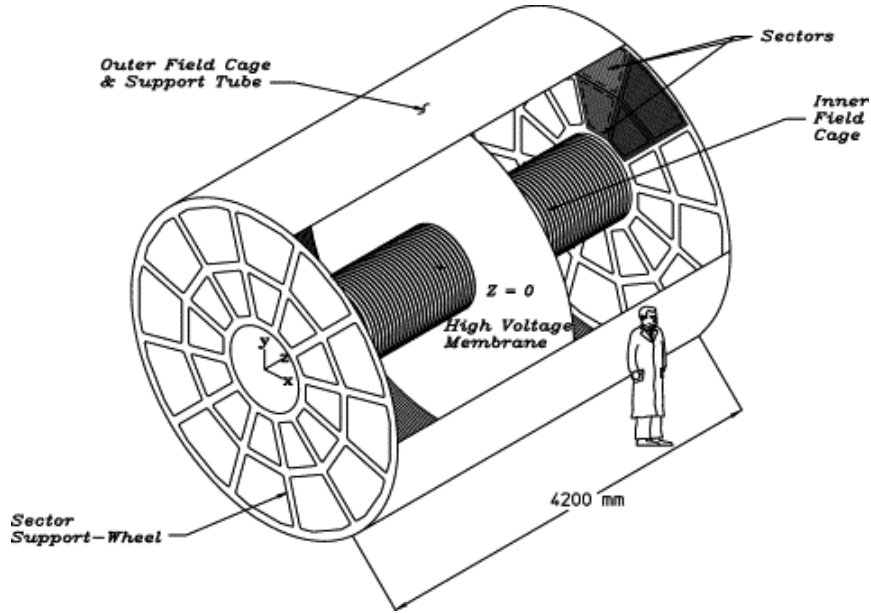


Figure 2.5: Perspective view of the STAR TPC.

The STAR TPC is shown schematically in Figure 2.5. The TPC is the primary detector element of the STAR detector. A large volume Time Projection Chamber (TPC) [Tho02a] for charge particle tracking and particle identification is located at a radial distance from 50 to 200 cm from the beam axis. The TPC is 4 m long and it covers a pseudo-rapidity range $|\eta| < 1.8$ for tracking with complete azimuthal symmetry



($0 < \phi < 2\pi$) providing the equivalent of 70 million voxels via 136,608 channels of front-end electronics (FEE). The TPC records the tracks of particles, measures their momenta, and identifies particles by measuring their ionization energy loss (dE/dx). Particles are identified over a momentum range from 100 MeV/c to greater than 1 GeV/c, and momenta are measured over a range of 100 MeV/c to 30 GeV/c.

The TPC sits in a large solenoidal magnet that operates at 0.5 T [Ber03a]. It is an empty volume of gas in a well-defined, uniform, electric field of ~ 135 V/cm. The paths of primary ionizing particles passing through the gas volume are reconstructed with high precision from the released secondary electrons which drift to the readout end caps at the end of the chamber. The uniform electric field which is required to drift the electrons is defined by a thin conductive Central Membrane (CM) at the center of the TPC, concentric field-cage cylinders and the readout end caps. Electric field uniformity is critical since track reconstruction precision is sub-millimeter and electron drift paths are up to 2.1 m.

The readout system is based on Multi-Wire Proportional Chambers (MWPC). The drifting electrons avalanche in the high fields at the $20 \mu\text{m}$ anode wires providing an amplification of 1000-3000. Diffusion of the drifting electrons and their limited number defines the position resolution. Ionization fluctuations and finite track length limit the dE/dx particle identification.

2.5.1 Sub-structures

The uniform electric field in the TPC is defined by establishing the correct boundary conditions with the parallel disks of the CM, the end caps, and the concentric field cage cylinders. The central membrane is located at the center of TPC and is operated at high voltage 28 kV. The Inner Field Cage (IFC) and Outer Field Cage (OFC) insure that the electric field uniformity is high. The field cage cylinders provide a series of equi-potential rings that divide the space between the central membrane and the anode planes into 182 equally spaced segments. One ring at the center is common to both ends. The central membrane is attached to this ring. The end caps as a whole are at ground.



2.5.1.1 Central Membrane

The CM is made from a number of pie-shaped, carbon-loaded kapton file sections, each of which is $70 \mu\text{m}$ thick. An outer hoop, which is mounted in the OFC, supports and keeps the CM secured under tension. There is no mechanical coupling to the IFC, other than a single electrical connection. This design minimizes material and maintains a good flat surface to within 0.5 mm . Thirty six aluminum stripes have been attached to each side of the CM to provide a low work function as the target for the TPC laser calibration system [Abe03a, Leb02a]. Electrons are photo-ejected when ultraviolet laser photons hit the stripes, and since the position of the narrow stripes are precisely measured, the ejected electrons can be used for spatial calibration.

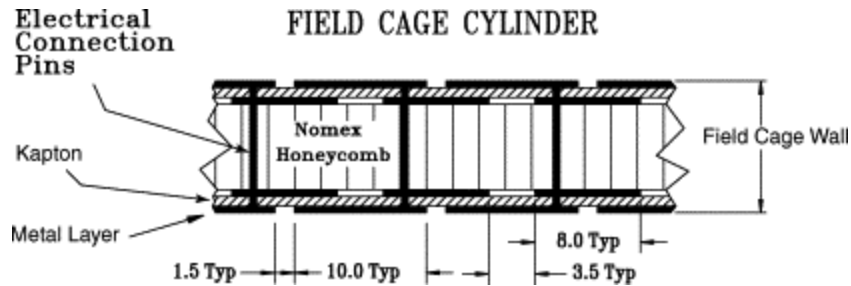


Figure 2.6: An example of IFC construction and composition of the cylinder wall.

2.5.1.2 Field Cage

The field cage cylinders serve the dual purpose of both gas containment and electric field definition. The mechanical design was optimized to reduce mass, minimize track distortions from multiple Coulomb scattering, and reduce background from secondary particle production. As the particles make their way from the collision vertex, through the IFC, and eventually to the active detector region of the TPC, the corruption of their kinematic information is kept to a minimum. Mechanically, the walls of the low mass self-supporting cylinders are effectively a bonded sandwich of two metal layers separated by NOMEX honeycomb (see Figure 2.6 for a cutaway view). Punch-through pins were used to electrically connect the layers on the two sides of the sandwich. The metal layer, which consists of kapton with metal on both sides, is etched to form electrically



separated 10 mm strips separated by 1.5 mm. The 1.5 mm break is held to the minimum required to maintain the required voltage difference between rings safely in order to limit the dielectric exposure in the drift volume thus reducing stray, distorting electric fields. The metal layer, is etched into stripes so that, after rolling the whole assembly into a cylinder, the stripes become rings around the cylinder. The sandwich structure of the OFC cylinder wall is 10 mm thick while the IFC has a wall thickness of 12.9 mm. Nitrogen gas or air insulation was used to electrically isolate the field cage from surrounding ground structures. This design choice requires more space than solid insulators, but it has two significant advantages. One advantage is to reduce multiple scattering and secondary particle production. The second advantage is the insulator is not vulnerable to permanent damage. The IFC gas insulation is air and it is 40 cm thick without any detectors inside the IFC. The OFC has a nitrogen layer 5.7 cm thick isolating it from the outer shell of the TPC structure. The field cage surfaces facing the gas insulators are the same as the surfaces facing the TPC drift volume. This design avoids uncontrolled dielectric surfaces, which can distort the electric field. The outermost shell of the TPC is a structure that is a sandwich of material with two aluminum skins separated by an aluminum honeycomb. The skins are a multi-layer wraps of aluminum. The innermost layer, facing the OFC, is electrically isolated from the rest of the structure.

2.5.1.3 End Caps

The end-cap readout planes of STAR is similar to the designs used in other TPCs but adjusted to accommodate the high track density at RHIC. The readout planes, MWPC chambers with pad readout, are modular units mounted on aluminum support wheels. The readout modules, or sectors, are arranged as on a clock with 12 sectors around the circle. Only 3 mm spaces between the sectors is to reduce the dead area between the chambers. Each sector is divided into two sub-sectors. An inner radius sector and an outer radius sector (see Figure 2.7). The construction and maintenance of the sectors is greatly simplified by their modular nature and their manageable size. As illustrated in Figure 2.8, the MWPC chambers consists of four elements, a pad plane and three wire planes. The anode wire plane, with wires of 20 μm in thickness, along with the



pad plane on one side and the ground wire on the other side, comprise the amplification layer. The anode wires are biased on a high voltage to provide the necessary electric field to avalanche the electrons from the track ionization.

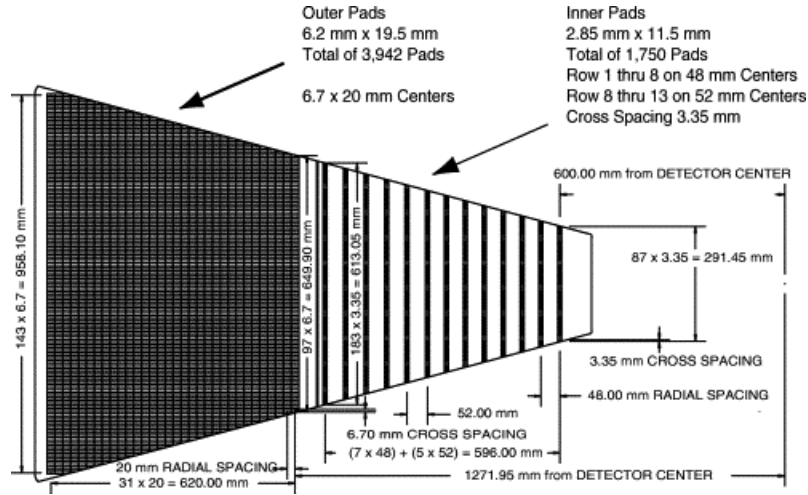


Figure 2.7: Full sector pad plane of TPC end caps. The inner sub-sector is shown on the right and the outer sub-sector is shown on the left.

The gating grid is the third wire plane and its purpose is to establish the boundary conditions defining the electric field in the TPC drift volume at the ends of the TPC. The gating grid also functions as a gate to control the passage of electrons from the active volume of the TPC into the MWPC. The gating grid allows drift electrons to pass through to the MWPC only while an event is being recorded. Otherwise, it is electrostatically opaque to electrons. More importantly, it also prevents ions produced in the MWPC from entering the active TPC volume. The drift velocity of ions is much slower than electrons, so they are too slow to move into the active TPC volume while the gating grid is "open". Furthermore, ions produced in the MWPC are drifted to cathode and gating grid electrodes while the gating grid is "closed".

2.5.1.4 TPC Material

The design emphasis was to limit material at the inner radius where multiple coulomb scattering is most important for accurate tracking and accurate momentum reconstruction. For this reason, aluminum was used in the IFC, limiting it to only 0.5% radiation

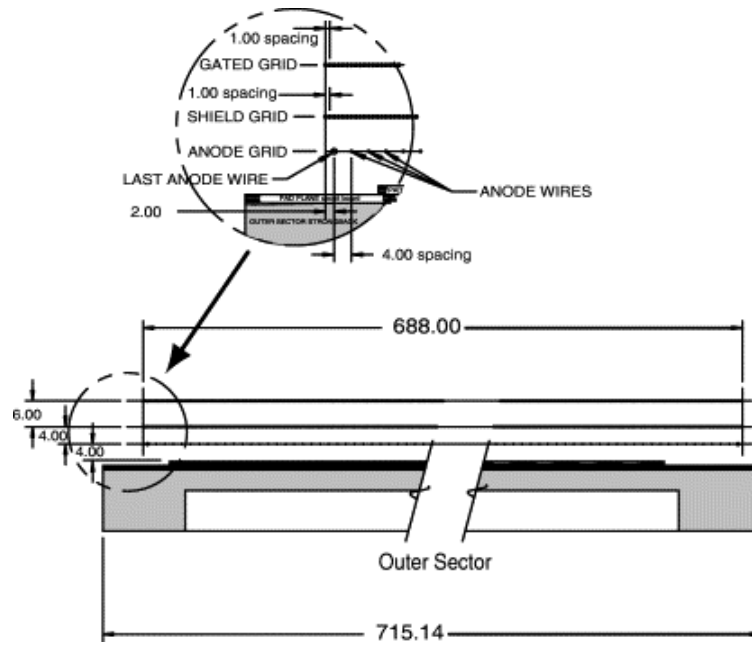


Figure 2.8: Outer sub-sector wire geometry of TPC end-caps.

length (X_0) and copper was used for the OFC, limiting it to 1.3% X_0 .



CHAPTER 3

Analysis Method

The techniques for reconstructing K_S^0 and Λ candidates with STAR TPC are well developed. The onset of K_S^0 and Λ v_2 results during RHIC Run II shed light on the origin of v_2 at low p_T and intermediate p_T region. The high statistics data are available from the RHIC Run IV. This allows us to study the centrality dependence of K_S^0 and Λ v_2 in details. Non-flow correlation, which is not correlated to the reaction plane will be the significant systematic uncertainty of K_S^0 and Λ v_2 measurements.

In this chapter, we discuss the selection criteria for events and tracks, reconstruction of K_S^0 and Λ , their v_2 extraction techniques and different flow methods. A quick and efficient way of choosing V0 cuts will be given. The v_2 versus invariant mass method used for extracting signal v_2 will be presented. Flow methods including Event Plane method, Sub-event method and Lee-Yang Zero method will be discussed.

3.1 Event and Track Selection

Trigger Setup Name	Run No.	Vertex Cut	Trigger ID	Events No.
productionLowMidHigh	≥ 5042040	$ V_z < 30$ cm	15007	6.3 M
productionMinBias	≥ 5023099	$ V_z < 30$ cm	15007	13.4 M
productionMinbias	< 5023099	$-10 < V_z < 50$ cm	15003	6.2 M

Table 3.1: Run IV trigger and events selection for minimum bias in Au + Au collisions at $\sqrt{s_{NN}} = 200$ GeV

During RHIC Run IV, the STAR experiment collects the minimum bias events for



Au + Au collisions at $\sqrt{s_{NN}} = 200$ GeV from three minimum bias triggers. The Run IV trigger and event selection for minimum bias in Au + Au at $\sqrt{s_{NN}} = 200$ GeV are summarized in Table 3.1. Each minimum bias trigger is specified by the combination of the trigger setup name, useful Run No. and the trigger ID. Events, for which no primary vertex is found were discarded. For the triggers listed in the first two rows of Table 3.1, events with z-vertex further than 30 cm from the main TPC center were discarded. For the trigger listed in the last row of Table 3.1, the asymmetric offline z-vertex cut should be applied since the events were taken before the vertex window was identified as being offset by 20 cm. Events useful for our analysis are listed in the most right column. The total number of minimum bias events are 25.9 million which is larger than that of Run II Au + Au 200 GeV data by more than a factor of 10.

Centrality Bin	Multiplicity	Geometric Cross Section
1	14-31	70%-80%
2	31-57	60%-70%
3	57-96	50%-60%
4	96-150	40%-50%
5	150-222	30%-40%
6	222-319	20%-30%
7	319-441	10%-20%
8	441-520	5%-10%
9	> 520	0%-5%

Table 3.2: Run IV centrality bins in Au + Au collisions at $\sqrt{s_{NN}} = 200$ GeV.

There are two kind of reconstructed tracks. One is the global track, other is the primary track. The global track is defined by the helix fit to the TPC points one by one. The collision vertex can be identified from all the reconstructed global tracks. The primary track is defined by the helix fit to the TPC points along with the vertex. The number of tracks (i.e. multiplicity) measured by the main TPC is used to define the STAR's centrality intervals. The TPC reference multiplicity is the number of the primary tracks in the TPC with the 15 or more fit points having the pseudo-rapidity



from -0.5 to 0.5 and a distance of closet approach (DCA) to the primary vertex less than 3 cm. The nine centrality bins and the corresponding geometric cross section are listed in Table 3.2. A part of low multiplicity events are rejected due to a lower cut on CTB to reject the non-hadronic events. The total number of events should be corrected by the Glauber model. The geometric cross section listed in Table 3.2 is the fraction of the corrected total number of events.

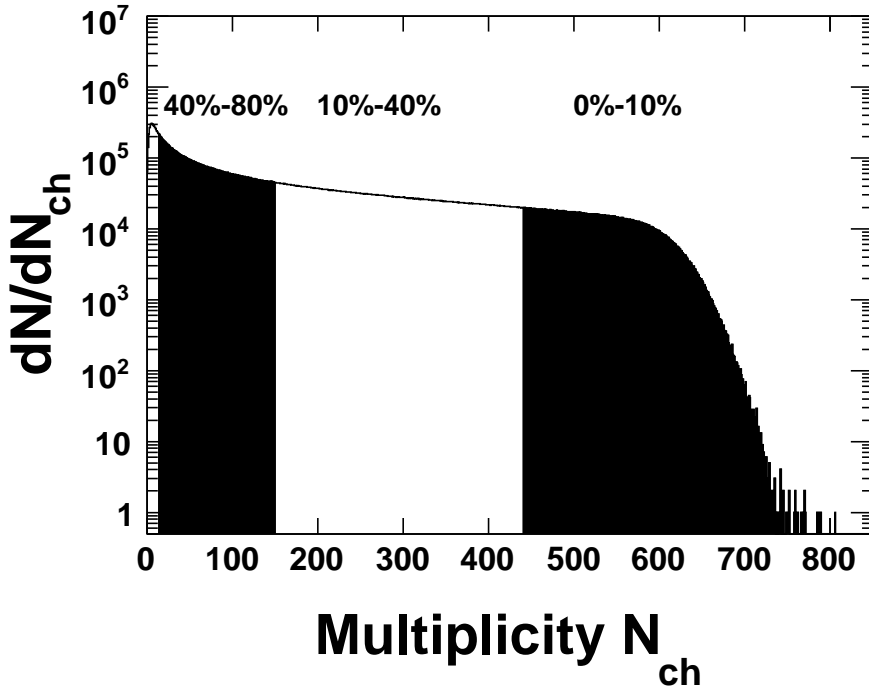


Figure 3.1: The TPC charged particle multiplicity distribution in Au + Au collisions at $\sqrt{s_{NN}} = 200$ GeV. N_{ch} is the number of the reference multiplicity. The geometry cross section used for v_2 analysis is combined into three centrality intervals shown in the Figure.

Figure 3.1 shows charged particle multiplicity distribution without the Glauber correction. Events below 80% centrality are not used in the analysis. The three combined centrality bins used in the analysis are 0%-10%, 10%-40% and 40%-80%, which are indicated in the Figure 3.1.



3.2 V0 Reconstruction

We reconstruct K_S^0 , Λ and $\bar{\Lambda}$ through their weak decay channel: $K_S^0 \rightarrow \pi^+ + \pi^-$, $\Lambda \rightarrow p + \pi^-$ and $\bar{\Lambda} \rightarrow \bar{p} + \pi^+$. The properties of these decays are summarized in Table 3.3. The identification of K_S^0 , Λ and $\bar{\Lambda}$ is based on statistics-wise invariant mass distribution. The charged p and π tracks are identified by the energy loss in TPC. We define the four-momentum of p and π by assigning their mass and momentum measured from the helix in TPC and then calculate the invariant mass of all possible pairs of positive and negative charged particles.

Particle Type	Decay Channel	Branching Ratio (%)	$c\tau$ (cm)	Mass (GeV/ c^2)
K_S^0	$\pi^+ + \pi^-$	68.95	2.68	0.497
$\Lambda(\bar{\Lambda})$	$p + \pi^- (\bar{p} + \pi^+)$	63.9	7.89	1.115

Table 3.3: K_S^0 and $\Lambda(\bar{\Lambda})$ weak decay properties

There are many fake decay vertex among the reconstructed decay vertex known as the combinatorial background. Many reasons could lead to the combinatorial background such as the misidentification of daughter track, the decay vertex close to the primary vertex and daughter tracks of a pair from different V0.

We utilize decay geometry to reject fake pairs. $c\tau$ of K_S^0 and Λ is 2.68 cm and 7.89 cm. Most of them will decay in the TPC of 2 m radius. In the laboratory frame, the decay vertex is in the order of a few centimeter further than primary vertex with several hundreds microns. So the decay vertex is well separated from the primary vertex. The decay topology is shown in Figure 3.2. The V0 is named after the "V" topology with the "0" net charge. The dca (distance of closet approach) between two daughter tracks is the parameter to determine the point of the decay vertex. The real decay vertex should distribute at smaller dca than fake decay vertex. Dca1 (Dca2) is the dca of the daughter to the primary vertex. The decay daughters should distribute at larger values than primary tracks. b is the dca from the primary vertex to the direction of V0 momentum. Ideally, b is equal to zero. rv is the distance which V0 travels in TPC (decay length).

To reduce the combinatorial backgrounds, we develop a new and quick method to

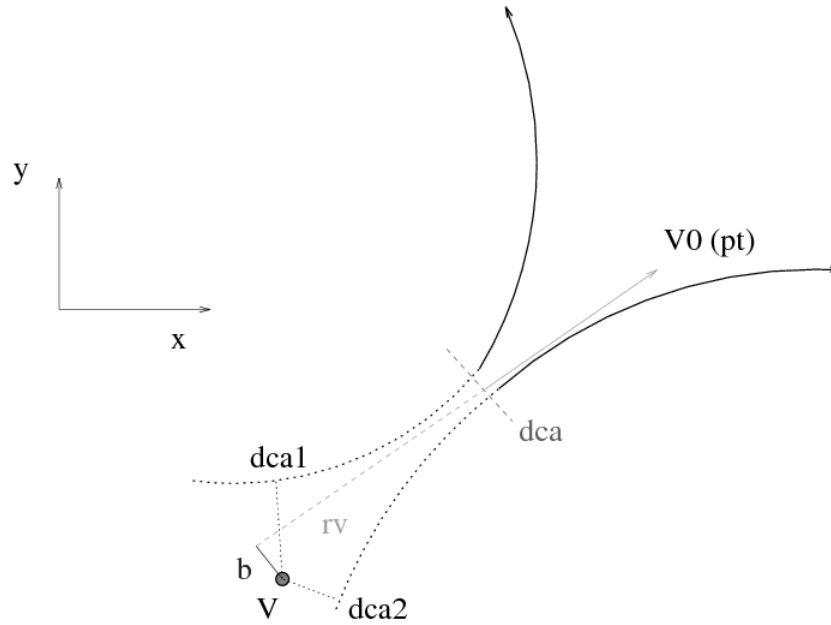


Figure 3.2: V0 decay topology, Figure from [Mar98a]

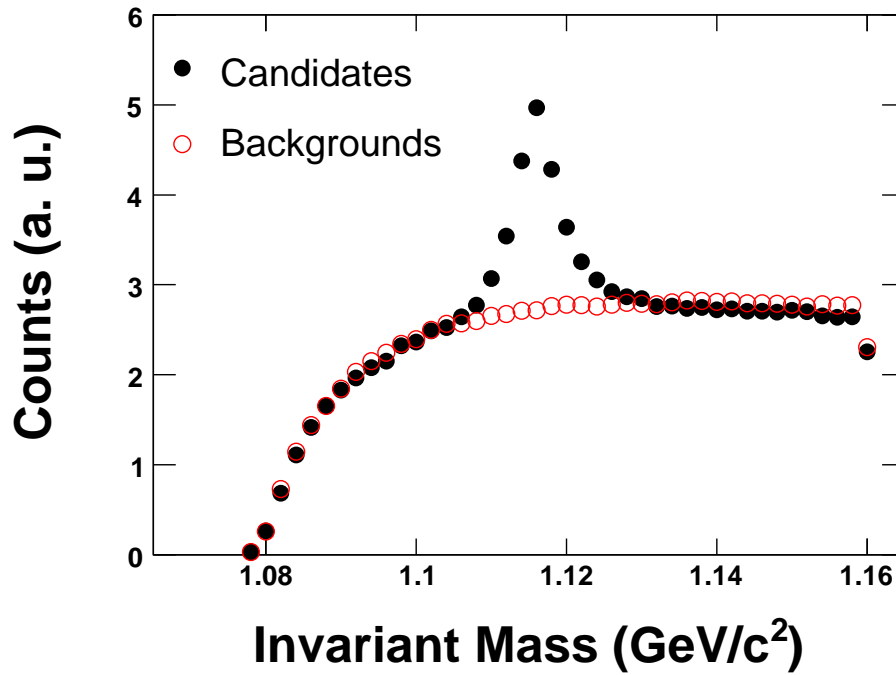


Figure 3.3: Invariant mass distribution of $\Lambda + \bar{\Lambda}$ candidates and combinatorial backgrounds for $p_T > 3.6$ GeV/c in minimum bias Au + Au collisions at $\sqrt{s_{NN}} = 200$ GeV. Combinatorial backgrounds are reconstructed from rotating π by 180 degrees and normalized to match background level.



choose the cuts on various $V0$ parameters. To illustrate this method, first let us have a look at the invariant mass distribution of $V0$ candidates and combinatorial backgrounds. We take $\Lambda + \bar{\Lambda}$ for p_T above 3.6 GeV/ c as an example. In Figure 3.3, the reconstructed $\Lambda + \bar{\Lambda}$ candidates and backgrounds with very loose cuts are represented by solid circles and open circles, respectively. The reconstructed backgrounds are estimated by rotating one daughter by 180 degrees. In this way, the angular correlation are destroyed for some degrees. There are large combinatorial backgrounds with loose cuts. The backgrounds from rotation can be used for cut studies though they don't exactly match the backgrounds far from the peak.

The cuts are studied one by one while others are fixed with loose values. We start with the dca of π from $\Lambda + \bar{\Lambda}$ decay. In the Figure 3.4 (a), the dca distribution of π from $\Lambda + \bar{\Lambda}$ candidates and backgrounds from rotation method are represented by solid line and dashed line, respectively. Here, we assume background dca from rotation method has the same distribution as the real background dca. At small dca, solid line and dashed line are nearly overlapped. In this region, the candidates are mostly dominated by the backgrounds. As we go to the larger dca, the difference between two lines tells you the real π dca from $\Lambda + \bar{\Lambda}$ contributes in this region. Figure 3.4 (b) show the distribution of solid line subtracting dashed line in Figure 3.4 (a) i.e. the dca distribution of π from real $\Lambda + \bar{\Lambda}$. We can do it more quantitatively. Figure 3.4 (c) shows the significance ($\frac{Sig}{\sqrt{Sig+Bg}}$) as a function of π dca. The large significance is achieved at relative large dca. The vertical line marks the final cut chosen for the v_2 analysis. Similarly, we can optimize the other cuts with the similar processes. The other two important cuts, the dca between two daughters and the decay length are illustrated in (d)-(f) and (g)-(i), respectively.

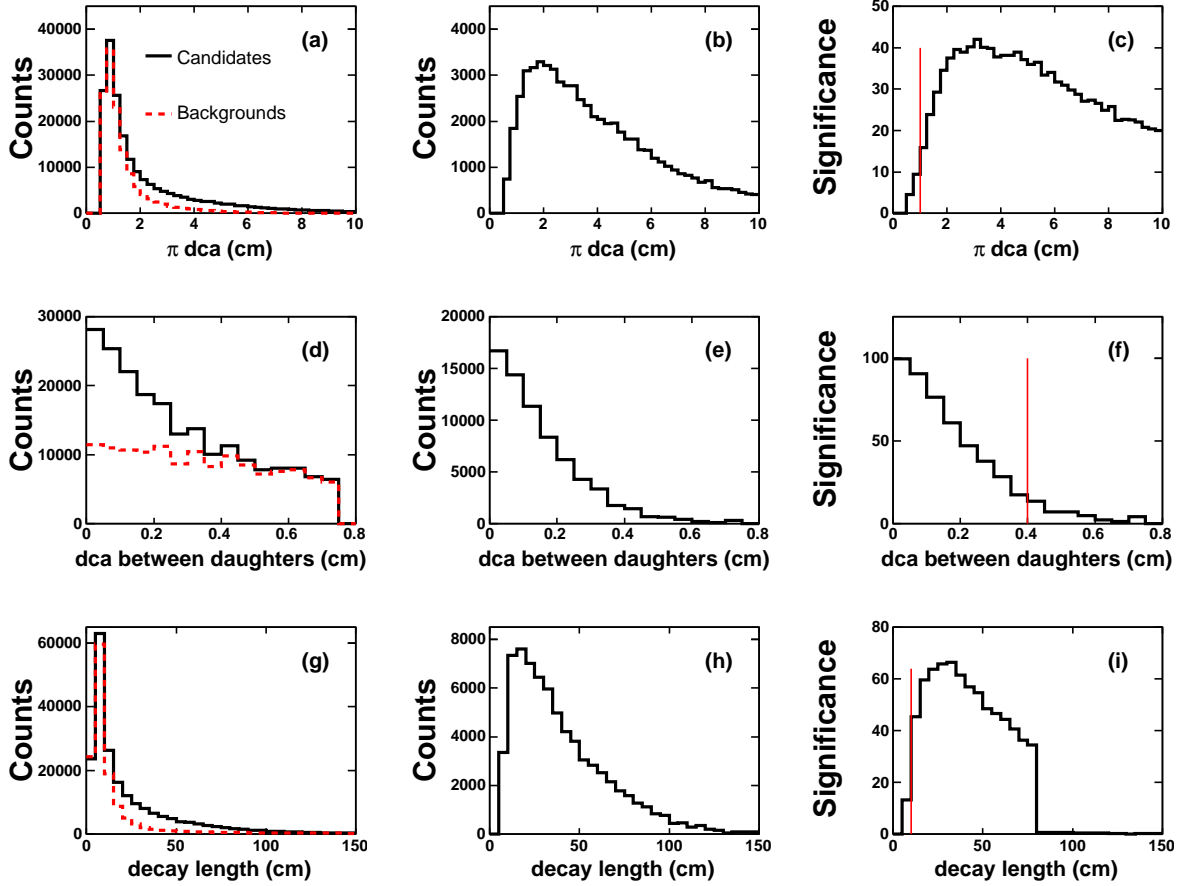


Figure 3.4: V0 cuts selection method. The example shown is the selection of π dca, dca between daughters and decay length for $p_T > 3.6$ GeV/c in minimum bias Au + Au collisions at $\sqrt{s_{NN}} = 200$ GeV. For example, as for π dca. (a) shows the dca distribution of π from candidates and backgrounds, represented by solid line and dashed line, respectively. Backgrounds are reconstructed from rotating one daughter. (b) shows the distribution of solid line subtracting dashed line in (a) i.e. the dca distribution of π from real V0s. (c) Significance ($\frac{Sig}{\sqrt{Sig+Bg}}$) as a function of π dca. The vertical line marks the final cut for π dca.



p_T (GeV/c)	< 0.8	0.8-3.6	> 3.6
π dca to primary vertex (cm)	> 1.5	> 1.0	> 0.5
dca between daughters (cm)	< 0.7	< 0.75	< 0.5
dca from primary vertex to V0	< 0.7	< 0.75	< 0.5
decay length (cm)	4-150	4-150	10-120

Table 3.4: Cuts selection criteria for K_S^0 in Au + Au collisions at $\sqrt{s_{NN}} = 200$ GeV.

p_T (GeV/c)	< 0.8	0.8-3.6	> 3.6
π dca to primary vertex (cm)	> 2.5	> 2.0	> 1.0
p dca to primary vertex (cm)	> 1.0	> 0.75	> 0
dca between daughters (cm)	< 0.7	< 0.75	< 0.4
dca from primary vertex to V0	< 0.7	< 0.75	< 0.75
decay length (cm)	4-150	4-150	10-125

Table 3.5: Cuts selection criteria for $\Lambda + \bar{\Lambda}$ in Au + Au collisions at $\sqrt{s_{NN}} = 200$ GeV.

Table 3.4 and Table 3.5 list the V0 optimized cuts for K_S^0 and $\Lambda + \bar{\Lambda}$ in Au + Au collisions at $\sqrt{s_{NN}} = 200$ GeV, respectively. These cuts are used for this v_2 analysis. Applying these cuts, the signal over background ratio will be significantly enhanced. Figure 3.5 and Figure 3.6 show K_S^0 and $\Lambda + \bar{\Lambda}$ invariant mass distribution in Au + Au collisions at $\sqrt{s_{NN}} = 200$ GeV for selected p_T and centrality bins. The selected p_T bins are $0.6 \text{ GeV}/c < p_T < 0.8 \text{ GeV}/c$, $3.2 \text{ GeV}/c < p_T < 3.6 \text{ GeV}/c$ and $4.4 \text{ GeV}/c < p_T < 5.0 \text{ GeV}/c$, which are typically p_T bins for low p_T , intermediate p_T and high p_T , respectively. For each p_T bin, 40%-80%, 10%-40% and 0%-10% centrality bins used for v_2 analysis are shown. Very clear K_S^0 and $\Lambda + \bar{\Lambda}$ peaks are observed. The cuts, especially dca efficiently remove most of the combinatorial backgrounds. The central collisions have smaller signal over background ratio than the peripheral collisions due to larger multiplicity in central collisions. At higher p_T , the helix of decay daughter track with larger p_T more likely points back to the primary vertex. The dca distribution of daughters from V0 at higher p_T is more similar to that of backgrounds coming from the



primary vertex than at lower p_T . This is why signal over background ratio at higher p_T is smaller than lower p_T .

The remaining backgrounds are estimated from the fit to the invariant mass distribution with functions describing signals and backgrounds. The fit function is two gaussian plus a polynomial. We use two gaussian functions with the same mass peak parameter to describe signal and use a polynomial function to describe the backgrounds. The fourth and second order polynomial functions are used in order to estimate the systematic errors from background uncertainties. The systematic error is a few percent, we will discuss in details later. The background distribution is estimated from the polynomial in the fit. The signal distribution is estimated by data minus polynomial. The signal over total ratio distribution and background over total ratio distribution (fit over data) will be used to extract K_S^0 and $\Lambda + \bar{\Lambda}$ signal v_2 .

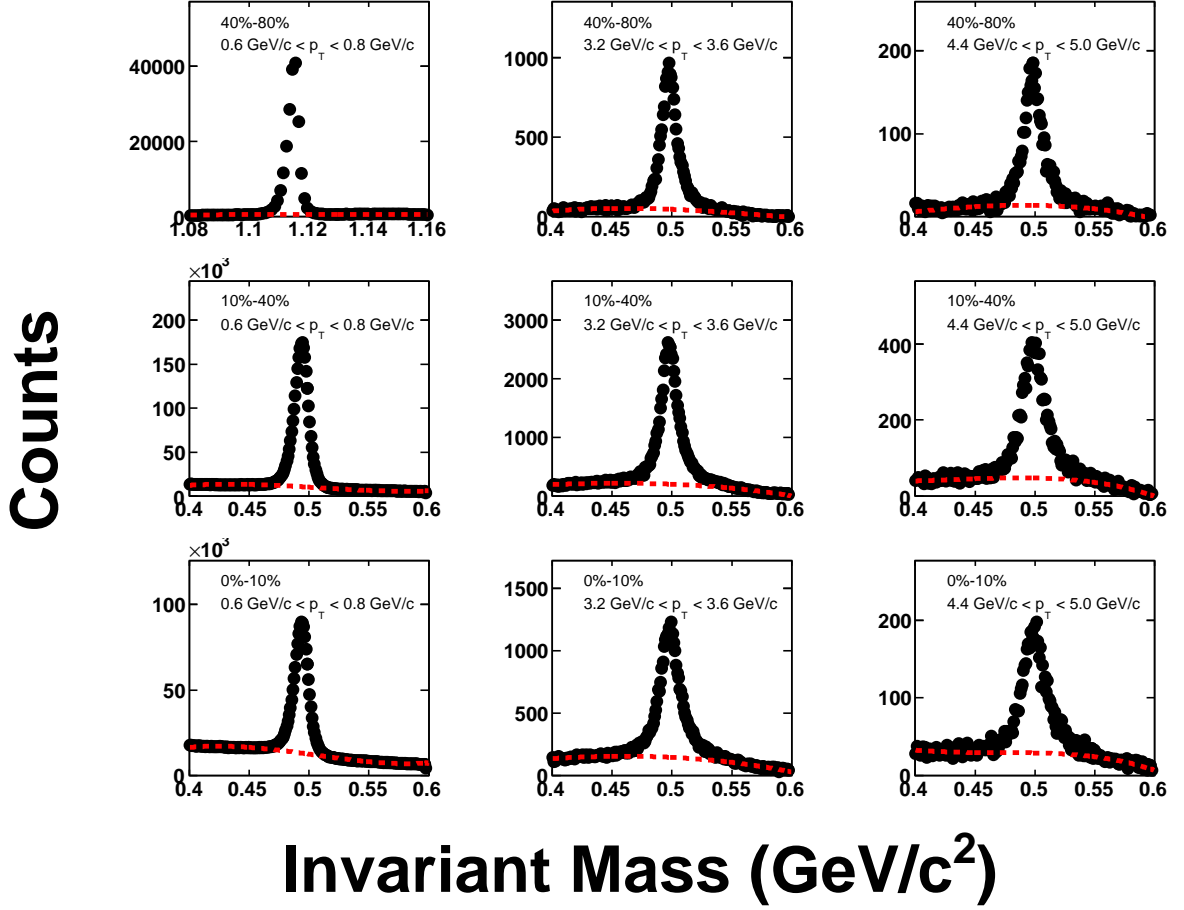


Figure 3.5: Invariant mass distribution of K_S^0 in Au + Au collisions at $\sqrt{s_{NN}} = 200$ GeV for different selected centrality and p_T bins. The left column, the middle column and the right column show the selected low p_T bin, intermediate p_T bin and high p_T bin, respectively. The top row, the middle row and the bottom row show the peripheral bin, mid-central bin and central bin, respectively. The circles represent the invariant mass distribution applying V0 cuts. The dashed lines are fit to the remaining combinatorial backgrounds.

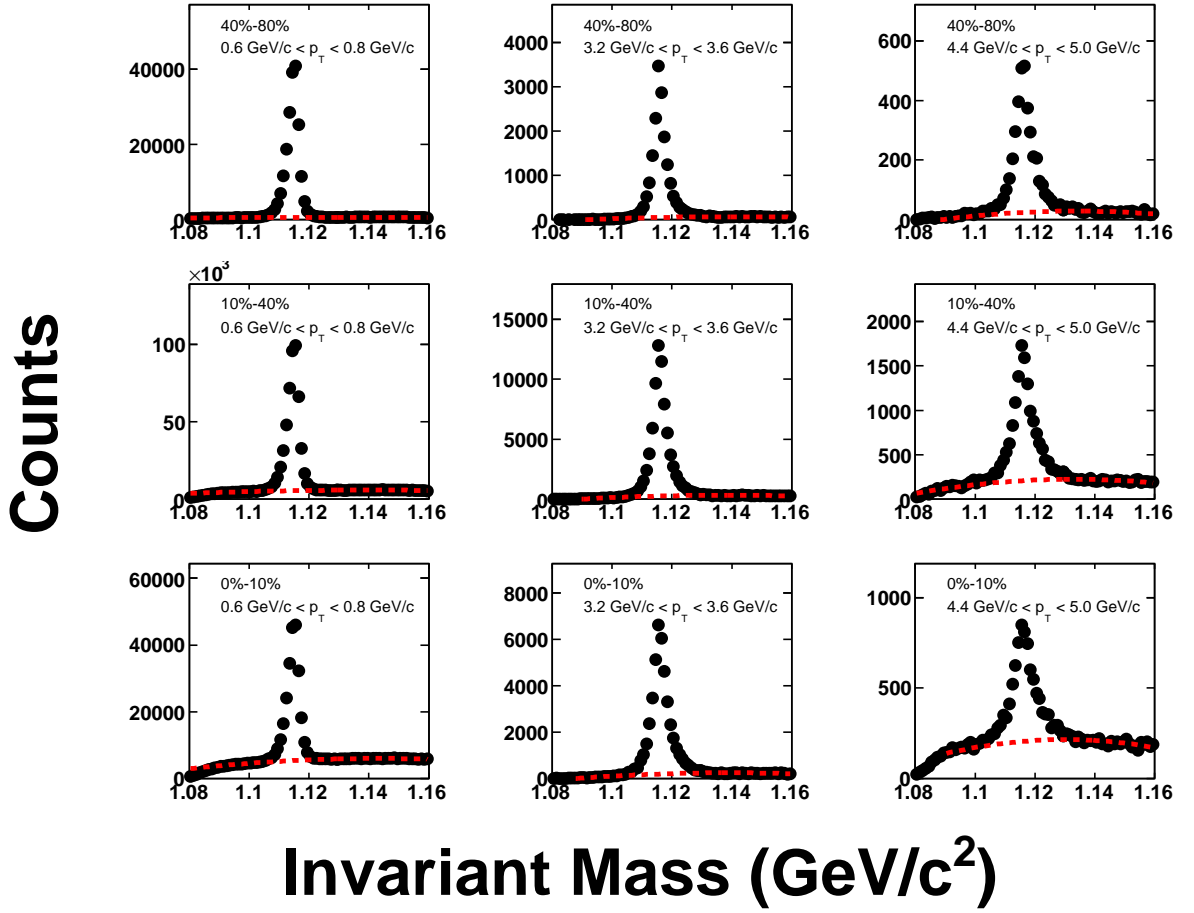


Figure 3.6: Invariant mass distribution of $\Lambda + \bar{\Lambda}$ in Au + Au collisions at $\sqrt{s_{NN}} = 200$ GeV for different selected centrality and p_T bins. The left column, the middle column and the right column show the selected low p_T bin, intermediate p_T bin and high p_T bin, respectively. The top row, the middle row and the bottom row show the peripheral bin, mid-central bin and central bin, respectively. The circles represent the invariant mass distribution applying V0 cuts. The dashed lines are fit to the remaining combinatorial backgrounds.



3.3 Event Plane Method

At RHIC, the collision energies are very high. The time necessary to build up the initial spatial anisotropy is believed to be short because the two colliding nuclei are highly Lorentz contracted. The global picture of flow governed by the hot and dense matter is appropriately decoupled into two components: transverse flow and longitudinal flow. The transverse flow is perpendicular to the beam direction while the longitudinal flow is along with the beam direction. Based on the assumption that transverse flow and longitudinal flow are well decoupled, we study the transverse expansion by the azimuthal distribution of emitted particles with respect to the reaction plane, which can be conveniently described by the Fourier expansion [Oll92a, Oll93a, Vol96a]:

$$E \frac{d^3 N}{d^3 p} = \frac{1}{2\pi} \frac{d^2 N}{p_T dp_T dy} \left(1 + \sum_{n=1}^{\infty} 2v_n \cos[n(\phi - \Psi_r)] \right) \quad (3.1)$$

where Ψ_r denotes the (true) reaction plane angle, and the sine terms vanish due to the reflection symmetry with respect to the reaction plane. The coefficients v_n is equal to $\langle \cos[n(\phi - \Psi_r)] \rangle$, where $\langle \rangle$ indicates average over all particles in all events. The second harmonic v_2 is the largest component, so-called elliptic flow representing the almond shape of momentum space anisotropy.

Event Plane method for measuring flow include several steps. Firstly, the essence is to estimate the reaction plane. The estimated reaction plane is called event plane. Secondly, the estimated Fourier coefficients in the expansion of the azimuthal distribution of emitted particles is evaluated with respect to the event plane. Thirdly, the Fourier coefficients are evaluated by correcting estimated coefficients by the event plane resolution. The event plane resolution is the limited resolution in angle of measured event plane. The corrected coefficients are relative to the real reaction plane.

3.3.1 Event Plane Reconstruction

The event plane is reconstructed by anisotropy flow itself. This means that the event plane can be determined independently for each harmonic of the anisotropic flow. In



case of elliptic flow, n is equal to 2. The Equation 3.2, 3.3 and 3.4 define the event flow vector Q_2 and the event plane angle Ψ_2 :

$$Q_2 \cos(2\Psi_2) = X_2 = \sum_i w_i \cos(2\phi_i) \quad (3.2)$$

$$Q_2 \sin(2\Psi_2) = Y_2 = \sum_i w_i \sin(2\phi_i) \quad (3.3)$$

$$\Psi_2 = \left(\tan^{-1} \frac{\sum_i w_i \sin(2\phi_i)}{\sum_i w_i \cos(2\phi_i)} \right) / 2 \quad (3.4)$$

The sum goes over the particles used in the event plane calculation, which is called flow tracks. The flow track selection criteria are listed in Table 3.6. The w_i is weights. Usually the weights are assigned with the transverse momentum. This choice of weights is to make the reaction plane resolution the best by maximizing the flow contributions to the flow vector. Note that the event plane angle Ψ_2 is in the range $0 < \Psi_2 < \pi$.

Flow track selection criteria	
nHits	> 15
nHits/nMax	> 0.52
dca	< 2 cm
transverse momentum	$0.1 < p_T < 2.0$ GeV/c
pseudo-rapidity	$ \eta < 1.0$

Table 3.6: Selection criteria for flow tracks used in the event plane reconstruction

3.3.2 Flattening Event Plane Distribution

The azimuthal distribution of the reaction plane would be isotropic in the laboratory system. If the detector is perfect: isotropic and one hundred percent efficient of detecting particles, the measured event plane should be isotropic. The real detectors have the limitation of the coverage and efficiency. The finite acceptance of the detector will lead the particles to be azimuthally anisotropic, which will introduce a bias in the estimation



of event plane. We remove the detector bias by applying ϕ weights to the tracks. The ϕ weights are generated by inverting the normalized ϕ distribution of detected tracks for a large events sample. When other weights are applied in the event plane calculation, they are also included into the ϕ weights. The ϕ weights compensate the inefficiency of detecting tracks for either limitations. So after ϕ weights are applied, the event plane distribution should be isotropic.

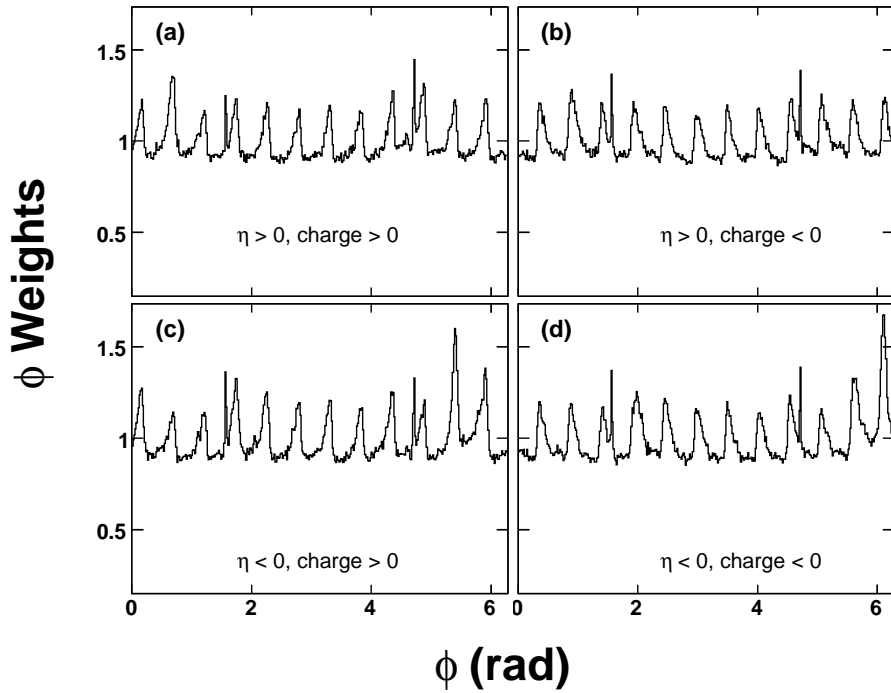


Figure 3.7: An example of ϕ weights used to flatten the event plane distribution taking acceptance effects into account. The weights shown are for the most central 5% of cross section in Au + Au collisions at $\sqrt{s_{NN}} = 200$ GeV .

The acceptance of the STAR detector depends on both particle-wise and event-wise quantities. The particle-wise quantity includes pseudo-rapidity η , azimuth angle ϕ , transverse momentum p_T and the sign of the charge of a particle. The event-wise quantity includes the position of the collision vertex, multiplicity of the event. To take these variables into account, we generate the ϕ weights separately for positive or negative η , for positive or negative charge, for nine different centrality bins and for each day.



Figure 3.7 shows an example of ϕ weights in Au + Au collisions at $\sqrt{s_{NN}} = 200$ GeV. The 12-fold periodic structure reflects the structure of TPC acceptance. TPC has twelve sectors and vacancies between two sectors. The probability of particles hitting the middle of the sector is higher than that of particles hitting the edges of the sector. The observed periodic structure is easily understood in this way. The peak positions shift for particles with opposite charges. This is because the particles starting at the same ϕ have a high probability to hit the TPC on one side with the positive charge and on the other side with the negative charge.

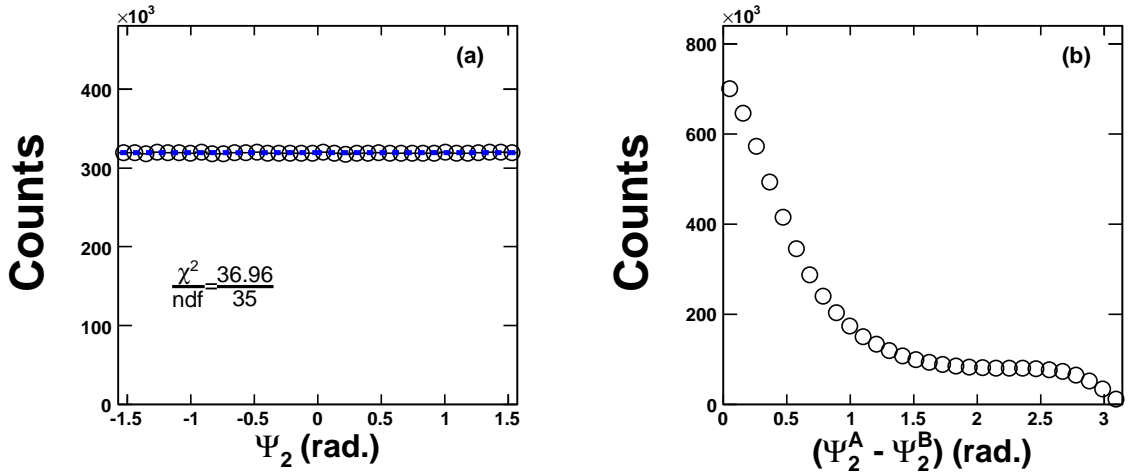


Figure 3.8: (a) Azimuthal distribution of Event Plane angle. The dashed line is a constant fit to it. (b) The distribution of the differences between two random sub-event Event Plane angles.

Figure 3.8 (a) shows the second harmonic event plane azimuthal distribution after ϕ weights are applied. To show how flat it is, we do a constant fit to the event plane azimuthal distribution. The χ^2/ndf is around 1. As the event plane is flat, the acceptance effects will not bias the measurements of v_2 .

3.3.3 Event Plane Resolution

The observed v_2 is correlated to the event plane. Due to finite multiplicity in the event plane calculation, there are some uncertainties between the event plane and real reaction plane. The observed v_2 has to be corrected by the event plane resolution, which is given



by Equation 3.5 [Vol98a].

$$v_2 = \frac{v_2^{obs}}{\langle \cos[2(\Psi_2 - \Psi_r)] \rangle} \quad (3.5)$$

The mean cosine sums over the whole event sample. Where v_2 , v_2^{obs} , Ψ_2 and Ψ_r are the real v_2 , observed v_2 , the event plane angle and the real reaction plane angle. It is found that $\langle \cos[2(\Psi_2 - \Psi_r)] \rangle$ is the reaction plane resolution. To calculate it, we divide a full event into two random sub-sets of tracks (sub-events). According to Equation 3.4, we calculate the event plane of two sub-events separately. The differences between the two sub-event plane angles ($\Psi_2^A - \Psi_2^B$) are shown in Figure 3.8 (b). The event plane resolution for the sub-event is given by Equation 3.6.

$$\langle \cos[2(\Psi_2^A - \Psi_r)] \rangle = \sqrt{\langle \cos[2(\Psi_2^A - \Psi_2^B)] \rangle} \quad (3.6)$$

This is based on the assumption that there are no other correlations except flow effects. Taking into account that the multiplicity dependence of event plane resolution, the full event plane resolution can be calculated from the sub-event event plane resolution by Equation 3.7, where C is a constant. In case of low resolution, C is equal to $\sqrt{2}$.

$$\langle \cos[2(\Psi_2 - \Psi_r)] \rangle = C \times \langle \cos[2(\Psi_2^A - \Psi_r)] \rangle \quad (3.7)$$

Figure 3.9 shows the event plane resolution for K_S^0 and $\Lambda + \bar{\Lambda}$. The resolution depends on the number of tracks used and the magnitude of the event asymmetry. For the most peripheral collisions, the small multiplicity reduces the resolution while for the most central collisions, the small v_2 weakens it. As a consequence, the resolution reaches its maximum at the centrality of 20%-30% of the collision cross section. K_S^0 and $\Lambda + \bar{\Lambda}$ have the same event plane resolution for these narrow centrality intervals.

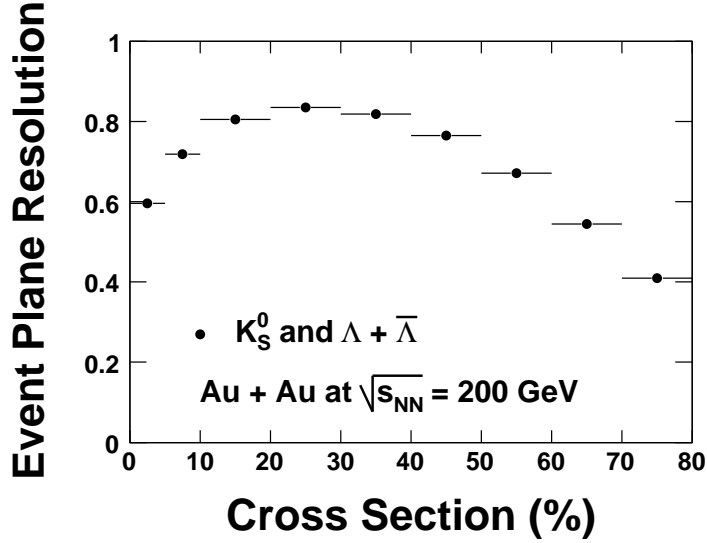


Figure 3.9: Event plane resolution for 200 GeV Au + Au collisions. The resolution corrects the effect that finite multiplicity leads to the uncertainty of determining the Event Plane. For the narrow centrality bins, K_S^0 and $\Lambda + \bar{\Lambda}$ have the same values of Event Plane resolution.

3.4 Sub-event Method

Sub-event method has the similar procedures to measure v_2 as standard Event Plane method. Sub-event method divides all tracks for a full event into two sub-set track groups (i.e. two sub-events) according to η or charge sign instead of randomly choosing flow tracks. The event plane of two sub-events are reconstructed according to Equation 3.2, 3.3 and 3.8, however the sum goes over all tracks in each sub-event instead of the full event. For η sub-event method, sub-event plane reconstructed using tracks with $0.15 < \eta < 1$ and $-1 < \eta < -0.15$ are represented by $\Psi^A(0.15 < \eta < 1)$ and $\Psi^B(-1 < \eta < -0.15)$, respectively. For charge sub-event method, sub-event plane reconstructed using tracks with charge > 0 and charge < 0 are represented by $\Psi^A(q > 0)$ and $\Psi^B(q < 0)$, respectively.

To calculate v_2^{obs} , tracks correlate with the sub-event event plane. For η sub-event method, a track with $\eta > 0$ or $\eta < 0$ correlates with $\Psi^B(-1 < \eta < -0.15)$ or $\Psi^A(0.15 < \eta < 1)$, respectively. The η sub-event method attempts to reduce the contribution from



non-flow effects (mostly due to short range correlations) by correlating particles separated in space coordinates. A η gap between positive and negative pseudorapidity subevents is introduced in order to guarantee that non-flow effects are reduced by enlarging the separation in space between the correlated particles. For charge sub-event method, a track with $q > 0$ or $q < 0$ correlates with $\Psi^B(q < 0)$ or $\Psi^A(q > 0)$. The v_2^{obs} should be corrected by the event plane resolution for the sub-event, Equation 3.6.

The non-flow effects (correlations) are reduced in both the observed flow and the event plane resolution. Depending on the nature of the remaining non-flow effects, v_2 measured this way may have values which are either lower or higher than those obtained with the standard method.

3.5 Lee-Yang Zero Method

The essence of measuring flow from Event Plane method is to correlate a particle with respect to an estimation of event plane using all particles. It is susceptible to the correlation, which is not related to the reaction plane (i.e. non-flow correlation) such as resonance decays, jets. This motivated the development of methods based on multi-particle correlations. Non-flow correlations generally involve only a small number of particles (typically two or three in the case of resonance decays, possibly more in the case of minijets). Anisotropic flow, which is a genuine flow effect, in principal involves correlations between a larger number of particles. Lee-Yang Zero method suppresses non-flow by using genuine correlations among all particles [Bha03a].

The recipe for extracting genuine collective flow proceeds in two successive steps. The first one is to estimate how the flow vector is correlated with the true reaction plane. More precisely, it is to estimate the mean projection of flow vector on the true reaction plane. This quantity is a weighted sum of the individual flow v_2 of all particles over phase space, which is called "integrated flow". The second step is to use integrated flow as a reference to analyze "differential flow" i.e. flow in a given phase-space window.



3.5.1 Integrated Flow

The flow vector is defined as:

$$Q_{2x} = \sum_i^M w_i \cos(2\phi_i), Q_{2y} = \sum_i^M w_i \sin(2\phi_i) \quad (3.8)$$

where the sum runs over all particles, M is the multiplicity of the event. ϕ_j is the azimuthal angle of the j th particle in laboratory frame. The flow vector is also used in the Event Plane method. The selection criteria for flow tracks is the same as Event Plane method listed in Table 3.6. For simplicity, the weights w_j are chosen to 1.

Integrated flow is defined as the average value of the flow vector projected on the unit vector with angle $2\Psi_r$, Ψ_r is the real reaction plane:

$$V_2 \equiv \langle Q_{2x} \cos(2\Psi_r) + Q_{2y} \sin(2\Psi_r) \rangle \quad (3.9)$$

With the unit weights, the integrated flow scales like the multiplicity:

$$V_2 = M v_2 \quad (3.10)$$

where v_2 is to be understood as an average over the phase space covered by the detector acceptance, we neglect the fluctuation of the multiplicity M . This shows the integrated flow is the sum of v_2 over all particles.

Experimentally, the estimate of V_2 is essentially to determine the first minimum of modulus of a complex generating function. The sum generating function is based on Q_2^θ , which is the flow vector projected on an arbitrary laboratory angle, θ .

$$Q_2^\theta \equiv \langle Q_{2x} \cos(2\theta) + Q_{2y} \sin(2\theta) \rangle = \sum_{j=1}^M w_j \cos(2(\phi_j - \theta)) \quad (3.11)$$

The sum generating function is given by:

$$G_2^\theta(ir) = \{e^{irQ_2^\theta}\} \quad (3.12)$$



where $\langle \dots \rangle$ denote an average over a large number of events for a given centrality. The sum generating function has the symmetry properties

$$G_2^{\theta+\pi/2}(ir) = G_2^\theta(-ir) \quad (3.13)$$

$$[G_2^\theta(ir)]^* = G_2^\theta(-ir) \quad (3.14)$$

where the star denotes complex conjugation. In order to obtain the integrated flow, one must evaluate $G_2^\theta(ir)$ for a large number of r bins. Then one must take the modulus of $|G_2^\theta(ir)|$ and plot it as a function of r . Taking the modulus, due to symmetry properties of sum generating function, this yields:

$$|G_2^{\theta+\pi/2}(ir)| = |G_2^\theta(-ir)| = |G_2^\theta(ir)| \quad (3.15)$$

This means one can restrict θ to the interval $[0, \pi/2]$ and r to the positive values. Figure 3.10 (a) illustrates an example of the modulus of sum generating function as a function r . It starts with 1 at $r = 0$, decreases rapidly to its first minimum called r_0^θ and then oscillates as r increases. The vertical arrow marks the position of r_0^θ . The square of the modulus is taken for good determination of the minimum from the numerical point of view since the modulus varies rapidly near its minimum. Normally, the first minimum is taken for several equally spaced θ in each centrality bin (i.e. $\theta = (k/p)(\pi/2)$) with $k = 0, 1, \dots, p-1$) in order to average out acceptance effects. In this analysis, we use 5 equally spaced θ (i.e. $p = 5$).

The r_0^θ is directly related to the integrated flow by

$$V_2^\theta\{\infty\} \equiv \frac{j_{01}}{r_0^\theta} \quad (3.16)$$

where $j_{01} \simeq 2.405$ is the first zero of the Bessel function J_0 .

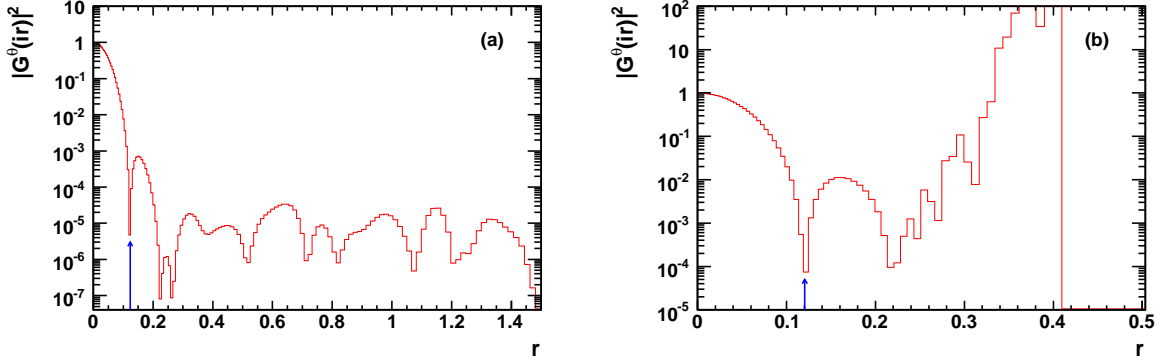


Figure 3.10: Examples of the modulus of generating functions as a function of the imaginary axis coordinate, r . The sum generating function and the product generating function are shown in (a) and (b), respectively. The vertical arrow indicates the first minimum, called r_0^θ .

3.5.2 Differential Flow

Using an estimate of r_0^θ and integrated flow V_2^θ , one can analyze the differential flow as following Equation:

$$\frac{v_2^\theta\{\infty\}}{V_2^\theta\{\infty\}} \equiv \text{Re} \left(\frac{\{\cos[2(\psi - \theta)]e^{ir_0^\theta Q_2^\theta}\}}{\{Q_2^\theta\}e^{ir_0^\theta Q_2^\theta}} \right) \quad (3.17)$$

where ψ denotes the azimuthal angle of the particle under study, Re denotes the real part. The numerator is an average over all particles belonging to a given phase space. The denominator is an average over all events.

Finally, $v_2\{\infty\}$ is obtained by averaging $v_2^\theta\{\infty\}$ over θ :

$$v_2\{\infty\} \equiv (1/5) \sum_{k=0}^4 v_2^{(k/5)(\pi/2)} \quad (3.18)$$

If correlations among all particles are pure from collective flow effect, r_0^θ should not depend on θ .

The Event Plane method requires that the flow vector has an isotropic distribution in azimuth. Since the real detector is not perfect, flattening the flow vector distribution is needed to remove acceptance effects. Lee-Yang Zero method isolates physical correlations by subtracting out the contribution of detector asymmetries as like cumulant expansion



[Bor01a], so flattening procedure is not needed. Since the drift of the beam in the detector over time might stimulate the effect of anisotropic flow, run-by-run re-centering of the Q vector was done for some of analysis.

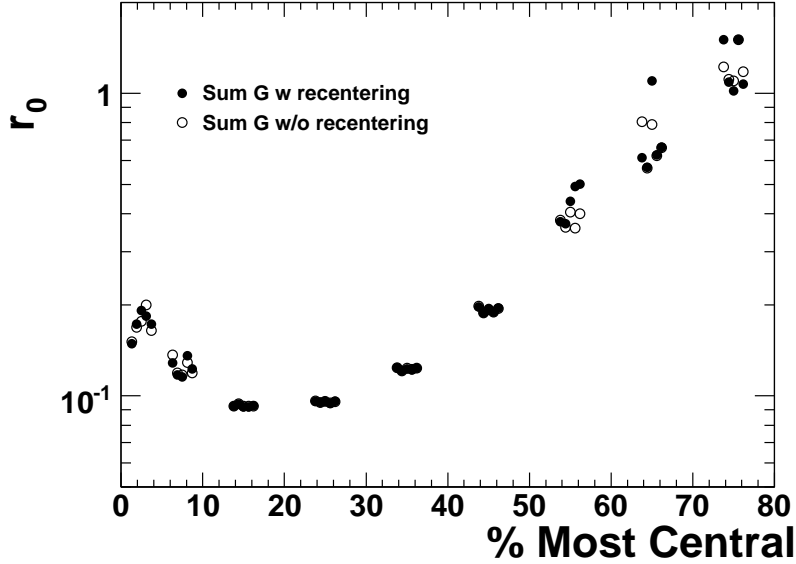


Figure 3.11: The first minimum r_0 for the sum generating function as a function of centrality. r_0 with recentering flow vector and without recentering are represented by solid circles and open circles, respectively. In each centrality, the first minimum taken from five θ are shown as a group.

Figure 3.11 shows the first minimum r_0 of the sum generating function from five equally spaced θ in Au + Au collisions at $\sqrt{s_{NN}} = 200$ GeV. r_0 with recentering flow vector and without recentering are represented by solid circles and open circles, respectively. In middle centrality corresponding to 10%-50% of cross section, r_0^θ with and without recentering shows good consistency. This indicates r_0 is not sensitive to the shift of the beam over time. r_0 for these centrality bins is independent on θ . In peripheral and central centrality bins, r_0 randomly fluctuates with θ for both with recentering and without recentering. Thus, the v_2 results scatter over θ and get large errors. The Lee-Yang Zero method only works for sufficient signal-to-noise ratio. Since the signal is v_2 and the noise is proportional to $1/\sqrt{M}$, the parameter $\chi = v_2\sqrt{M}$ determines the



applicability of the method. We find that the errors get large when $\chi < 0.8$, which is consistent with difficulties in determining r_0 for peripheral and central collisions. So Lee-Yang Zero method with sum generating function works for 10%-50% centrality bin and fails for more central collisions because v_2 is small and for more peripheral collisions because the multiplicity is small.

3.5.3 Product Generating Function

Alternatively, Lee-Yang Zero method has another generating function, which is based on the product of all particles. The product generating function is

$$G_2^\theta(r) = \prod_{j=1}^N [1 + irw_j \cos(2(\phi_j - \theta))] \quad (3.19)$$

This takes a lot more computer time because the product over all particles has to be done for each value of r . An example is shown in Figure 3.10 (b). It can be seen that the sum generating function oscillates after the first minimum, but the product generating function rises very fast. Thus, for the product generating function, the calculation was halted when $|G_2^\theta(r)|^2$ got larger than 1000. For the product generating function the differential flow is given by

$$v_2^\theta(\eta, p_t) = V_2^\theta \text{Re} \left(\frac{\left\langle G_2^\theta(ir_0^\theta) \frac{\cos(2(\psi-\theta))}{1+ir_0^\theta w_j \cos(2(\phi_j-\theta))} \right\rangle}{\left\langle G_2^\theta(ir_0^\theta) \sum_j \frac{w_j \cos(2(\psi-\theta))}{1+ir_0^\theta w_j \cos(2(\phi_j-\theta))} \right\rangle} \right) \quad (3.20)$$

3.6 v_2 versus m_{inv} Method

v_2 versus m_{inv} method is used to measure K_S^0 and $\Lambda + \bar{\Lambda}$ v_2 . K_S^0 and $\Lambda + \bar{\Lambda}$ candidates are identified on statistical basis. The invariant mass m_{inv} distributions show there are some remaining combinatorial backgrounds for K_S^0 and $\Lambda + \bar{\Lambda}$. The purpose of v_2 versus m_{inv} method is to extract signal v_2 .

The essence of v_2 versus m_{inv} method is based on the following Equation:



$$v_2^{Sig+Bg}(m_{inv}) = v_2^{Sig} \frac{Sig}{Sig+Bg}(m_{inv}) + v_2^{Bg}(m_{inv}) \frac{Bg}{Sig+Bg}(m_{inv}) \quad (3.21)$$

If we know signal plus background v_2 as a function of m_{inv} on left side of Equation 3.21, signal over total ratio as a function of m_{inv} and background over total ratio as a function of m_{inv} on right side of Equation 3.21, signal v_2 and background v_2 as a function of m_{inv} remain to be determined. With parameterizing $v_2^{Bg}(m_{inv})$ as a certain function, v_2^{Sig} can be extracted by fit to $v_2^{Sig+Bg}(m_{inv})$ with Equation 3.21.

To illustrate this method, Figure 3.12 shows an example for K_S^0 and $\Lambda + \bar{\Lambda}$ in Au + Au collisions at $\sqrt{s_{NN}} = 200$ GeV. Panel (a) and (c) shows invariant mass distribution for K_S^0 and $\Lambda + \bar{\Lambda}$, respectively. A 4th order polynomial fit to describe the background distribution is shown as solid line. $\frac{Bg}{Sig+Bg}(m_{inv})$ is calculated by dividing fit line by data. $\frac{Sig}{Sig+Bg}$ is calculated by $(1 - \frac{Bg}{Sig+Bg})$. v_2 of K_S^0 and $\Lambda + \bar{\Lambda}$ candidates represented by open circles are calculated and plotted in panel (b) and (d), respectively. The fit to v_2 of K_S^0 and $\Lambda + \bar{\Lambda}$ candidates with Equation 3.21 is shown in solid line. The background contributions and the signal contributions are shown as dashed line and dot-dashed line for K_S^0 and $\Lambda + \bar{\Lambda}$ plotted in (e) and (f) along with the total fit, respectively.

This method gives robust results: We fit a set of data points over wide m_{inv} region. Data points far from the mass peak region are only from background contributions since $\frac{Bg}{Sig+Bg}$ is equal to 1. v_2^{Sig+Bg} data points in this region have strong constraints on v_2^{Bg} when doing the fit. v_2^{Sig+Bg} data points in the mass region under peak constraint v_2^{Sig} with given $\frac{Sig}{Sig+Bg}$ and $\frac{Bg}{Sig+Bg}$ ratios. A large variation of v_2^{Sig} would lead to a strong disagreement of the fit curves with the measured data. Thus the shape of dip or bump of v_2^{Sig+Bg} in the mass region under peak is not necessary to measure v_2 . The systematic uncertainty of this method lies in the estimate of $\frac{Sig}{Sig+Bg}$ and $\frac{Bg}{Sig+Bg}$ ratio as a function of m_{inv} . This systematic uncertainty is studied by using different functions to fit the background, which is discussed in systematics section.

v_2 versus m_{inv} method is a method to measure v_2 and has nothing to do with flow correlations. Event Plane method and Lee-Yang Zero method are flow methods measuring flow correlations. In this analysis, v_2 versus m_{inv} method is applied with either

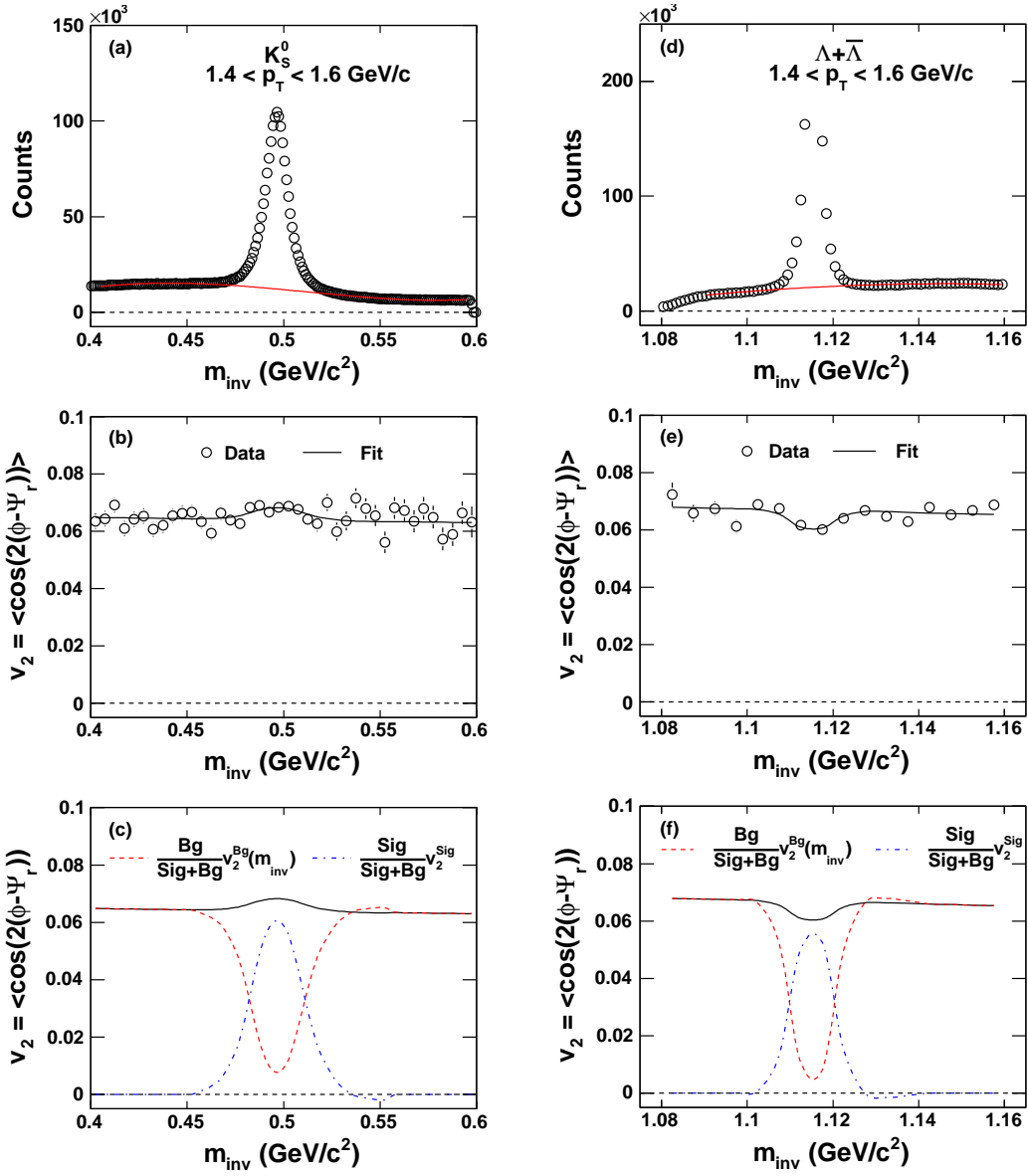


Figure 3.12: An example of using v_2 versus m_{inv} method to extract v_2 of K_S^0 and $\Lambda + \bar{\Lambda}$.



Event Plane method or Lee-Yang Zero method.

3.7 Systematic Errors

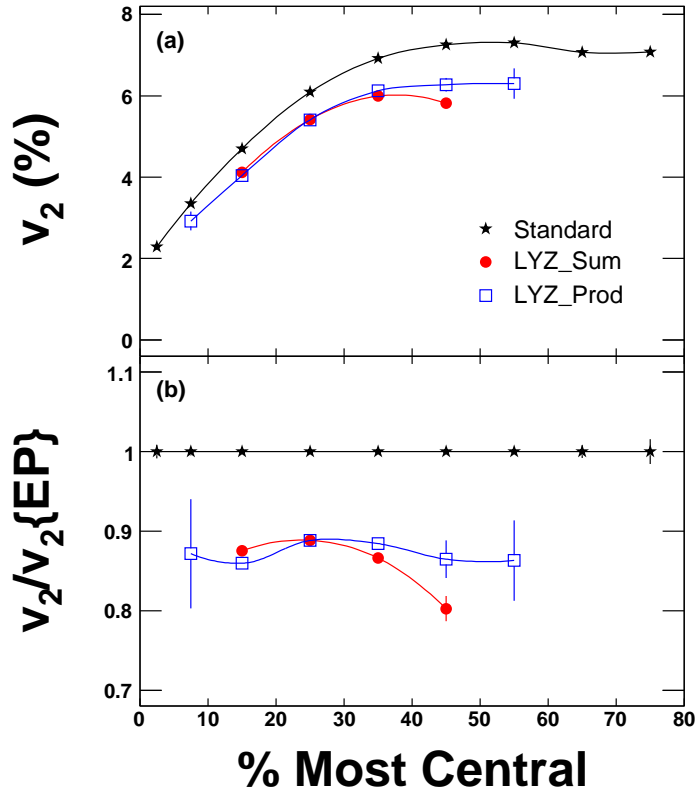


Figure 3.13: (a) p_T -integrated charge hadron v_2 as a function of geometrical cross section. Solid stars, solid circles and open squares represent Event Plane method, Lee-Yang Zero method with sum generating function and Lee-Yang Zero method with product generating function, respectively. (b) v_2 divided by $v_2\{EP\}$ as a function of geometrical cross section. The results are from Au + Au collisions at $\sqrt{s_{NN}} = 200$ GeV.

The non-flow systematic errors is estimated using Lee-Yang Zero method and Event Plane method. Figure 3.13 (a) show p_T -integrated charge hadron v_2 as a function of geometrical cross section in Au + Au collisions at $\sqrt{s_{NN}} = 200$ GeV. The Lee-Yang Zero method with sum generating function (solid circles) and with generating function (open squares) are consistent with each other. The Event Plane method (solid stars) is



larger than Lee-Yang Zero method, which is only presented in middle centrality for its applicability. The v_2 scaled by Event Plane method are shown in Figure 3.13 (b). From the ratio, the systematic errors between Event Plane method and Lee-Yang Zero method are in order of 10%.

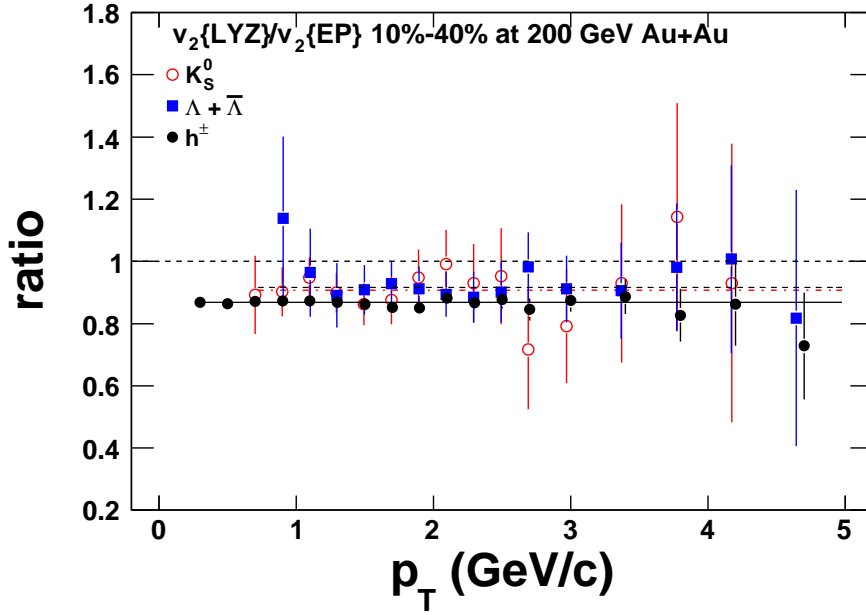


Figure 3.14: $v_2\{LYZ\}/v_2\{EP}$ ratio as a function of p_T . Sum generating function is used for $v_2\{LYZ\}$. Charged particle, K_S^0 and $\Lambda + \bar{\Lambda}$ are represented by solid circles, open circles and solid squares, respectively. Constant fits to the ratio are shown as lines.

Figure 3.14 shows v_2 ratio of Lee-Yang Zero method over Event Plane method as a function of p_T for 10%-40% centrality bin at 200 GeV Au + Au collisions. Charged particle, K_S^0 and $\Lambda + \bar{\Lambda}$ are represented by solid circles, open circles and solid squares, respectively. The ratios for charged particle, K_S^0 and $\Lambda + \bar{\Lambda}$ are separately fitted with a line. The χ^2/ndf for three fits are less than 1. The fits give 0.868 ± 0.003 for charged particle, 0.907 ± 0.026 for K_S^0 and 0.916 ± 0.027 for $\Lambda + \bar{\Lambda}$. The non-flow systematic errors estimated from Event Plane method and Lee-Yang Zero method with sum generating function are in order of 10% independent of p_T up to 5 GeV. The jet non-flow may significantly contribute to higher p_T region. K_S^0 and $\Lambda + \bar{\Lambda}$ seem to subject to the same amount of non-flow. The results of $v_2\{LYZ\}$ as a function of p_T will be presented in



Results chapter.

The systematic errors in K_S^0 and $\Lambda + \bar{\Lambda}$ v_2 measurement from background uncertainty, summing centrality and V0 cuts are estimated using Event Plane method. The background uncertainty is estimated by fitting the background with second and fourth order polynomial. The systematic error from background uncertainty is less than 3% below 6 GeV/c. The systematic uncertainty from summing centrality origins from $\frac{\langle v_2^{obs} \rangle}{\langle r \rangle} \neq \langle \frac{v_2^{obs}}{r} \rangle$. This effect is less than 5% below 6 GeV/c. The systematic uncertainty from V0 cuts is estimated by varying particle identification (PID) cuts, which change signal over background ratios by a factor of 3. This effect is about 5% below 4 GeV/c. From 4 GeV/c to 6 GeV/c, 40%-80% centrality bin is about 10% and 0%-10% centrality bin is about 25%.



CHAPTER 4

Results

In this chapter, we present the measurements of v_2 at mid-rapidity $|Y| < 1$ from Au + Au collisions at $\sqrt{s_{NN}} = 200$ GeV. v_2 results from Event Plane method are presented for K_S^0 and $\Lambda + \bar{\Lambda}$ in 0%-80%, 0%-10%, 10%-40% and 40%-80% centrality bins. v_2 results from Lee-Yang Zero method are presented for charged particle, K_S^0 and $\Lambda + \bar{\Lambda}$ in 10%-40%, 10%-20%, 20%-30% and 30%-40% centrality bins.

4.1 Glauber calculations

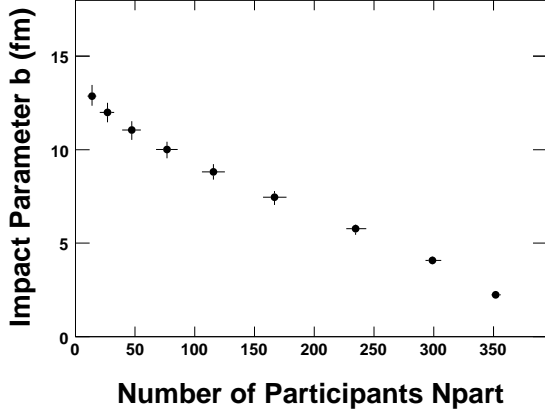
	0-80%	40-80%	10-40%	0-10%
$\langle \epsilon_{part} \rangle$	0.3843 ± 0.0001	0.5343 ± 0.0002	0.2829 ± 0.0001	0.1054 ± 0.0001
$\langle N_{part} \rangle$	126 ± 8	42 ± 7	173 ± 10	326 ± 6
$\langle N_{bin} \rangle$	293 ± 36	57 ± 14	393 ± 47	939 ± 72

Table 4.1: Glauber calculations in Au + Au collisions at $\sqrt{s_{NN}} = 200$ GeV. The nucleon-nucleon interaction cross section σ_{NN} of 42mb is used in the calculation.

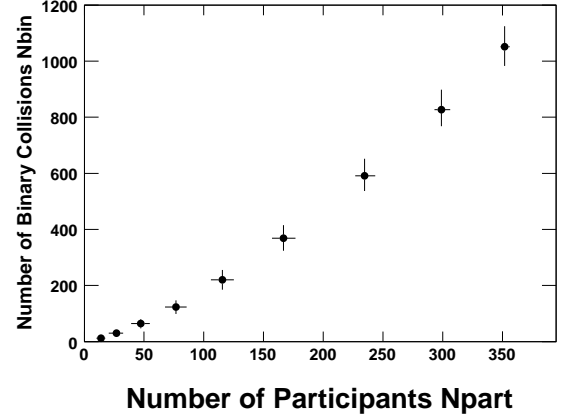
Quantities such as the average number of binary collisions, average number of participating nucleons and average number of eccentricity are related to the centrality dependence of v_2 measurements. They can not be directly measured. In STAR, the average value of these quantities was determined by the implementation of a Monte Carlo Glauber (MCG) model of relativistic heavy ion collisions. In the MCG model, many body interactions are approximated as the simple superposition of elementary nucleon-nucleon interactions. A detailed treatment of Glauber calculations in STAR can be found in Appendix E of Reference [Mil03a]. The average number of binary collisions, participants



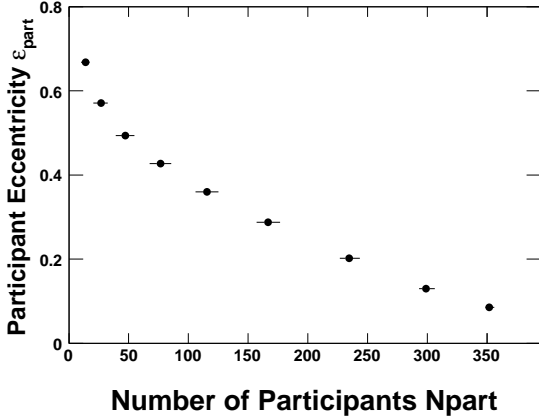
and participant eccentricity for centralities used in this analysis are listed in Table 4.1. The impact parameter, the number of binary collisions and the participant eccentricity versus the number of participants are shown in Figure 4.1 (a), (b), (c), respectively.



(a)



(b)



(c)

Figure 4.1: (a) Impact parameter b , (b) number of binary collisions N_{bin} and (c) participant eccentricity ϵ_{part} versus number of participants N_{part} from glauber calculation in Au + Au collisions at 200 GeV.

4.2 Elliptic Flow

4.2.1 Event Plane Method Results

Figure 4.2 shows minimum bias v_2 for K_S^0 and $\Lambda + \bar{\Lambda}$ at mid-rapidity $|Y| < 1$ in Au + Au collisions at $\sqrt{s_{NN}} = 200$ GeV. The open circles and open squares represent K_S^0 and $\Lambda + \bar{\Lambda}$, respectively. The Event Plane method is used for this analysis. The error bars are



statistical errors. The bands on data points are the systematic errors from background uncertainty, combining centrality and V0 cuts. The curves show the hydrodynamical calculations for π , K , p , Λ , Ξ and Ω [Huo05a]. With the high statistics from RHIC Run IV data set, the strange particle v_2 is measured up to $p_T \sim 7$ GeV/c for the first time. K_S^0 and $\Lambda + \bar{\Lambda}$ v_2 increase with p_T and then saturate/decrease at higher p_T . At low p_T ($p_T < 1.5$ GeV/c), the heavier $\Lambda + \bar{\Lambda}$ has smaller v_2 than the lighter K_S^0 . The hydrodynamical calculations are in good agreement with the mass and p_T dependence of v_2 in this p_T region. At intermediate p_T ($2 < p_T < 5$ GeV/c), hydrodynamical prediction breaks down. The p_T -scale where v_2 starts to deviate from hydrodynamical calculations is ~ 1 GeV/c for K_S^0 and ~ 2 GeV/c for $\Lambda + \bar{\Lambda}$. v_2 continues to increase and reach its maximum for K_S^0 at $p_T \sim 3$ GeV/c with the v_2 value of ~ 0.15 and $\Lambda + \bar{\Lambda}$ at $p_T \sim 4$ GeV/c with the v_2 value of ~ 0.2 . The particle type dependence is established up to $p_T \sim 6$ GeV/c. Above $p_T \sim 4$ GeV/c, v_2 shows a decreasing trend for K_S^0 .

Figure 4.3 shows v_2 of K_S^0 and $\Lambda + \bar{\Lambda}$ as a function of p_T at mid-rapidity for Au + Au collisions at $\sqrt{s_{NN}} = 200$ GeV for (a) 40%-80%, (b) 10%-40% and (c) 0%-10%. The same analysis method (i.e. the Event Plane method) is used as the minimum bias v_2 shown in Figure 4.2. Symbols, statistical errors and systematic errors are presented in the same way as minimum bias data in Figure 4.2. The hydrodynamical calculations are also shown for these three centralities. The three centrality bins have the similar p_T dependence of v_2 observed from the minimum bias: v_2 increases at low p_T , and then saturates at intermediate p_T . The mass dependence predicted by hydro models and the particle-type dependence of saturation are also observed for these three centrality bins. The values of v_2 in peripheral collisions is larger than that in central collisions.

4.2.2 Lee-Yang Zero Method Results

Figure 4.4 shows v_2 from the Lee-Yang Zero method as a function of p_T at mid-rapidity for 10%-40% in Au + Au collisions at $\sqrt{s_{NN}} = 200$ GeV. K_S^0 , $\Lambda + \bar{\Lambda}$ and charged particle are presented by open circles, open squares and open crosses, respectively. For comparisons, the v_2 of K_S^0 and $\Lambda + \bar{\Lambda}$ from the Event Plane method are shown as solid

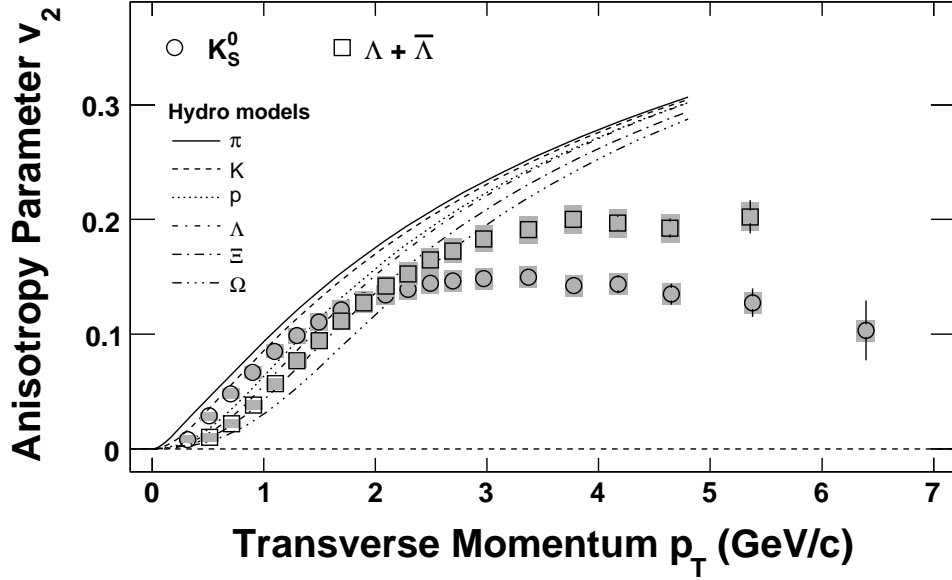


Figure 4.2: Elliptic flow v_2 as a function of transverse momentum p_T at mid-rapidity $|Y| < 1$ for minimum bias (0%-80% geometrical cross section) in Au + Au collisions at $\sqrt{s_{NN}} = 200$ GeV. The open circles and open squares represent K_S^0 and $\Lambda + \bar{\Lambda}$, respectively. The Event Plane method are used to measure v_2 shown in the plot. The error bars are statistical errors. The bands on data points are the systematic errors from background uncertainty, combining centrality and V0 cuts. Hydrodynamical calculations for π , K , p , Λ , Ξ and Ω are also shown for comparisons [Huo05a].

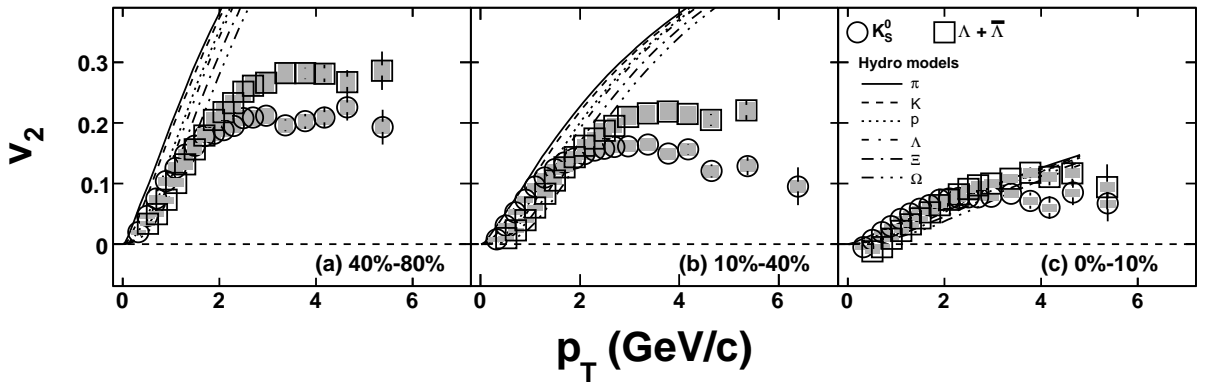


Figure 4.3: v_2 of K_S^0 and $\Lambda + \bar{\Lambda}$ as a function of p_T for (a) 40%-80%, (b) 10%-40% and (c) 0%-10% of collision geometry in Au + Au collisions at $\sqrt{s_{NN}} = 200$ GeV. Event Plane method is used to calculate v_2 values. Symbols, statistical errors and systematic errors are presented in the same way as minimum bias data in Figure 4.2.



and dashed line, respectively. The Lee-Yang Zero method is supposed to suppress the known non-flow effects such as jets, resonances [Bha03a]. However, the Lee-Yang Zero method yields larger statistical errors, which can be seen in the figure. Results for mid-central collisions are presented only since the Lee-Yang Zero method only works in these centrality bins for large signal-to-noise ratio. We can see that v_2 from the Lee-Yang Zero method is systematically smaller than v_2 from the Event Plane method by 10% up to 5 GeV, which can be seen in $v_2\{LYZ\}/v_2\{EP\}$ ratios (Figure 3.14). The mass ordering at low p_T and particle-type dependence of saturation at intermediate p_T are also observed with these measurements.

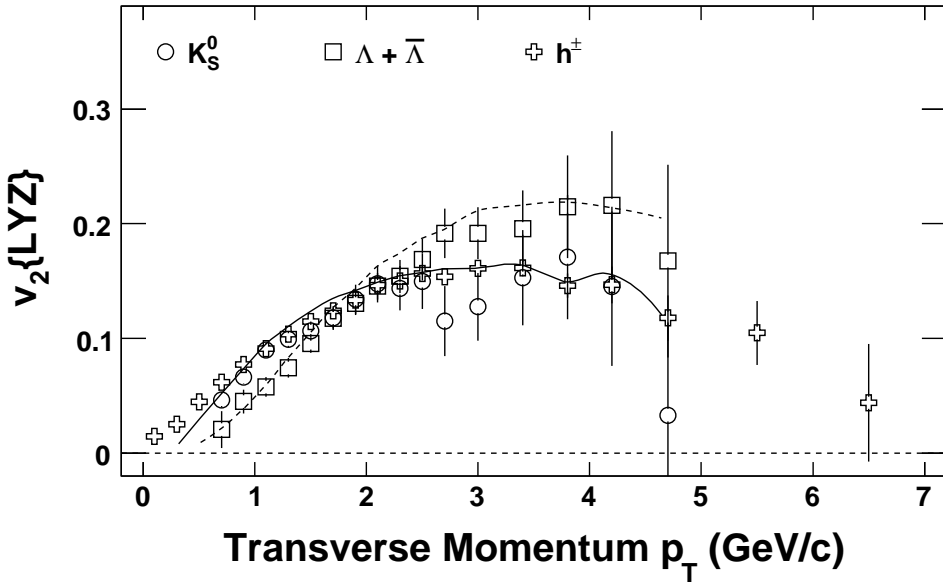


Figure 4.4: Elliptic flow v_2 as a function of transverse momentum p_T at mid-rapidity for mid-central collisions (10%-40% geometrical cross section) in Au + Au collisions at $\sqrt{s_{NN}} = 200$ GeV. The open circles, open squares and open crosses represent K_S^0 , $\Lambda + \bar{\Lambda}$ and charged particle, respectively. The Lee-Yang Zero method is used to calculate the values of v_2 in the plot. The error bars are shown for statistical errors only. For comparisons, the v_2 of K_S^0 and $\Lambda + \bar{\Lambda}$ from the Event Plane method are shown as solid and dashed line, respectively.

Figure 4.5 shows the centrality dependence of v_2 from Lee-Yang Zero method as a function of p_T for K_S^0 , $\Lambda + \bar{\Lambda}$ and charged particle at mid-rapidity in Au + Au collisions at $\sqrt{s_{NN}} = 200$ GeV. The centrality bins are shown for (a) 30%-40%, (b) 20%-30% and (c) 10%-20%. The magnitude of v_2 in these three centrality bins is similar. The mass

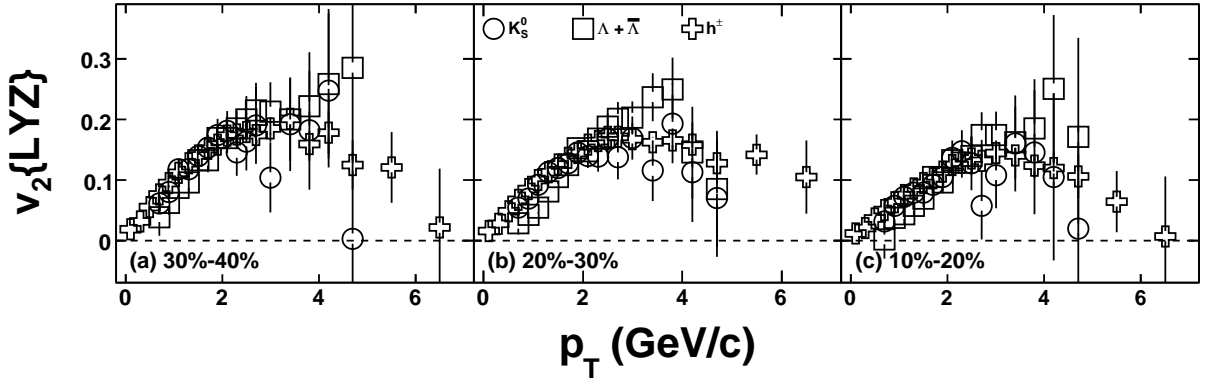


Figure 4.5: v_2 of K_S^0 , $\Lambda + \bar{\Lambda}$ and charged particle as a function of p_T for (a) 30%-40%, (b) 20%-30% and (c) 10%-20% of collision geometry in Au + Au collisions at $\sqrt{s_{NN}} = 200$ GeV. The error bars are shown for statistical errors only. The Lee-Yang Zero method is used to calculate the values of v_2 .

ordering at low p_T and particle-type dependence of saturation at intermediate p_T are observed in these three centrality bins.



CHAPTER 5

Discussion

5.1 Collective Flow

The measurements of disappearance of back-to-back high p_T hadron correlations indicate that the dense matter are produced in Au + Au collisions at RHIC energy [Adl03a]. The interactions among the constituents of the matter will lead to the collective effects such as collective motions if these strong interactions occur frequently enough. The collective motions are accumulative throughout the whole evolution of the system (i.e. both prehadronic stage and hadronic stage). The nature of interactions between the constituents at a certain stage should mark and reflect the properties of the system at this stage. In non-central collisions, the rescatterings/reinteractions convert the initial spatial anisotropy to final state momentum space anisotropy of freeze-out hadrons. Elliptic flow v_2 characterizes this momentum space anisotropy. The generated elliptic flow will reduce the spatial anisotropy of the system and quench its own origin. The quenching effect makes elliptic flow a unique probe to understand the properties of the early stage of such collisions. Again, elliptic flow is the largest component of the final state momentum space anisotropy, this may reveal that the development of elliptic flow is dominant at the early stage since the interactions of early hot and dense stage is much stronger than that of the hadronic stage.

Early dynamic information might be washed out by later hadronic rescatterings. Multi-strange baryons with their large mass and small hadronic cross sections [Hec98a, Bas99b, Dum99a, Bas00a, Bia81a, Che03a, Mul72a] should be less sensitive to hadronic rescatterings in the later stages of the collision and therefore a good probe of the early



stage of the collision. Recently, a systematic study from hadron p_T spectra, using the hydrodynamically motivated Blast Wave model, show the multi-strange baryons thermally freeze-out close to the the point where the chemical freeze-out occurs with $T_{ch} \sim 160$ MeV. This implies that multi-strange baryons are not or much less, affected by hadronic rescatterings during the later stage of heavy-ion collisions. So we extend our discussion to strange and multi-strange particle v_2 .

5.1.1 p_T Dependence

Figure 5.1 (a) shows the v_2 of K_S^0 , $\Lambda + \bar{\Lambda}$, $\Xi + \bar{\Xi}$ and $\Omega + \bar{\Omega}$ as a function of p_T for minimum bias in Au + Au collisions at $\sqrt{s_{NN}} = 200$ GeV. K_S^0 and $\Lambda + \bar{\Lambda}$ have one s quark, $\Xi + \bar{\Xi}$ have two s quarks and $\Omega + \bar{\Omega}$ have three s quarks. The hadron mass hierarchy is observed at low p_T (below ~ 2 GeV/c) with heavier particles having smaller v_2 than that of lighter particles as expected from the hydrodynamical calculations, which assume zero mean-free-path between interactions and local thermalization [Huo05a]. The hydro-like mass ordering for strange and multi-strange baryons extends to $p_T \sim 3$ GeV/c. $\Omega + \bar{\Omega}$ v_2 shows clear p_T dependence of sizable v_2 consistent with the mass ordering and saturates at $p_T \sim 3$ GeV/c with a value of $v_2 \sim 0.2$, which is similar to $\Lambda + \bar{\Lambda}$ and $\Xi + \bar{\Xi}$. This is an important improvement of $\Omega + \bar{\Omega}$ v_2 from Run IV statistics which is about 10 times larger than Run II where $\Omega + \bar{\Omega}$ has not clear p_T dependence [Ada05b]. In the scenario where multi-strange baryons are not or much less, affected by the hadronic stage, the mass ordering observed for strange and multi-strange hadrons, especially including $\Omega + \bar{\Omega}$ indicates the partonic collectivity generated at RHIC. At intermediate p_T region, v_2 deviates from hydro calculations and then saturates. Strange baryon $\Lambda + \bar{\Lambda}$ saturate at higher p_T with larger v_2 values than strange meson K_S^0 as first observed in reference [Ada04b]. v_2 of multi-strange baryon $\Xi + \bar{\Xi}$ and $\Omega + \bar{\Omega}$ are similar to that of strange baryon $\Lambda + \bar{\Lambda}$ and larger than that of strange meson K_S^0 . $\Omega + \bar{\Omega}$ shows the clear baryon behavior at intermediate p_T region (p_T above 3 GeV/c) for the first time. Again, due to its small hadronic cross section, measurements of $\Omega + \bar{\Omega}$ v_2 at intermediate p_T region may provide us information on the origin of v_2 at partonic stage for this p_T region.

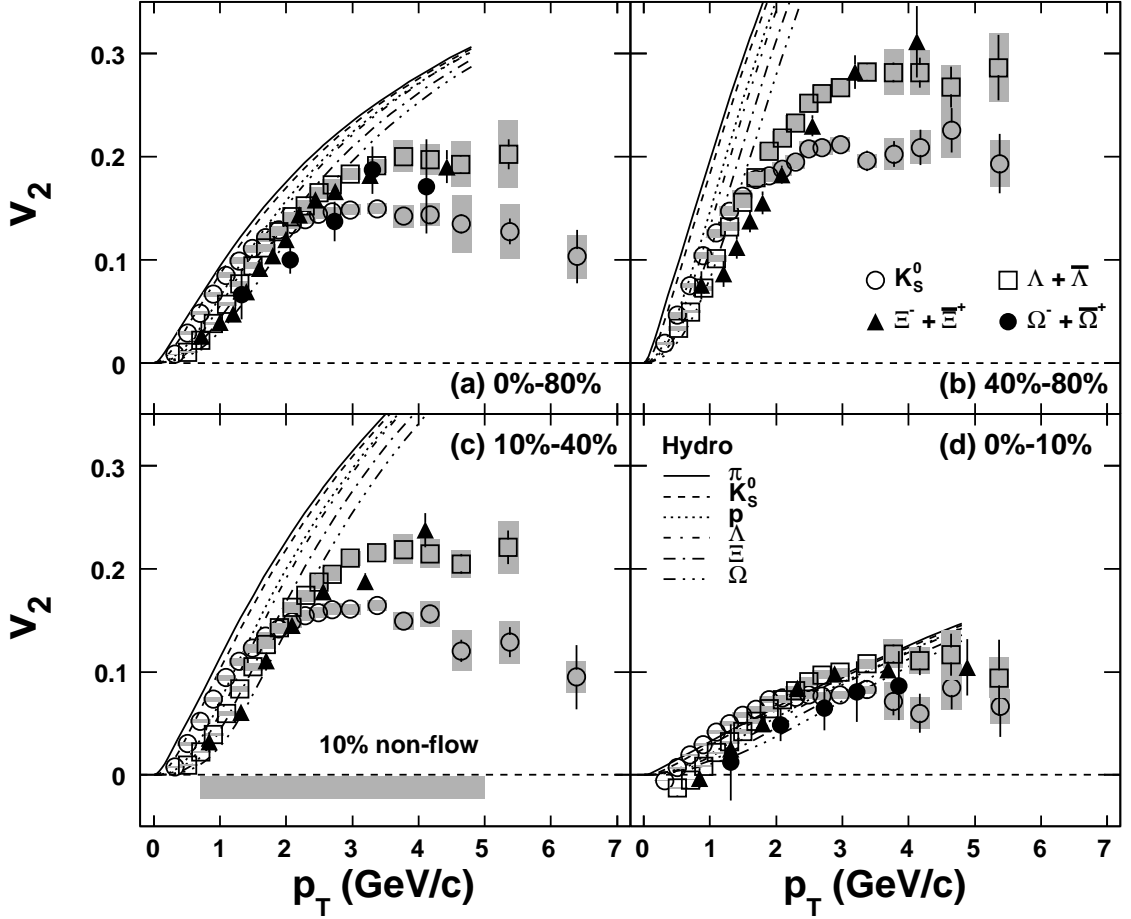


Figure 5.1: v_2 as a function of p_T for (a) 0%–80%, (b) 40%–80%, (c) 10%–40% and (d) 0%–10% in Au + Au collisions at $\sqrt{s_{NN}} = 200$ GeV. Open circles, open squares, solid triangles and solid circles represent K_S^0 , $\Lambda + \bar{\Lambda}$, $\Xi + \bar{\Xi}$ and $\Omega + \bar{\Omega}$, respectively. The error bars on the data points represent statistical uncertainties. The bands on the data points represent systematic uncertainties taking into account effects from background estimation, combining centralities and different cuts. The systematic uncertainty of non-flow for 10%–40% is separately shown as a band below $v_2 = 0$, which represents the asymmetric negative error. Hydro calculations are shown for comparison [Huo05a].



5.1.2 Centrality Dependence

Figure 5.1 (b), (c) and (d) show the centrality dependence of v_2 as a function of p_T for K_S^0 , $\Lambda + \bar{\Lambda}$, $\Xi + \bar{\Xi}$ and $\Omega + \bar{\Omega}$. (b), (c) and (d) represent 40%-80%, 10%-40% and 0%-10% centrality interval, respectively. $\Omega + \bar{\Omega}$ is only measured in 0%-10% centrality bin due to limited statistics. Hydrodynamical calculations [Huo05a] for these centrality bins are also drawn for comparison. Similarly, hydro-like mass-ordering at low p_T and baryon-meson difference at intermediate p_T are observed for different centralities as well as minimum bias. The p_T -scale where $\Lambda + \bar{\Lambda}$ and K_S^0 v_2 cross over is very similar for these three centrality intervals, which is ~ 1.8 GeV/c. The magnitude of v_2 shows strong centrality dependence: larger v_2 values in peripheral collisions than in central collisions.

5.1.3 $m_T - m$ Scaling

Figure 5.2 shows v_2 of strange and multi-strange particles as a function of $m_T - m$ for (a) 0%-80%, (b) 40%-80%, (c) 10%-40% and (d) 0%-10% in Au + Au collisions at $\sqrt{s_{NN}} = 200$ GeV. $\Omega + \bar{\Omega}$ is only shown for 0%-80% and 0%-10%. $m_T - m$ is the transverse kinetic energy, which is the same variable as the KE_T used in [Ada06a]. There, it shows v_2 as a function of $m_T - m$ is a linear function at $(m_T - m) < 0.8$ GeV/c² and independent of hadron mass. Here, we observe the same $m_T - m$ scaling for central, mid-central and peripheral collisions. $\Omega + \bar{\Omega}$ is also consistent with the $m_T - m$ scaling for minimum bias and central collisions. For comparison, the hydro calculations for hadrons with different mass are also shown in corresponding centrality bins. Changing from p_T to $m_T - m$ variable, hydro change from mass-ordering to the distribution, in which no scalings are observed. This is particularly clear at the higher $m_T - m$ region. At intermediate $m_T - m$, baryon v_2 saturates at higher value than meson v_2 as observed in p_T dependence since only the horizontal axis variable changes.

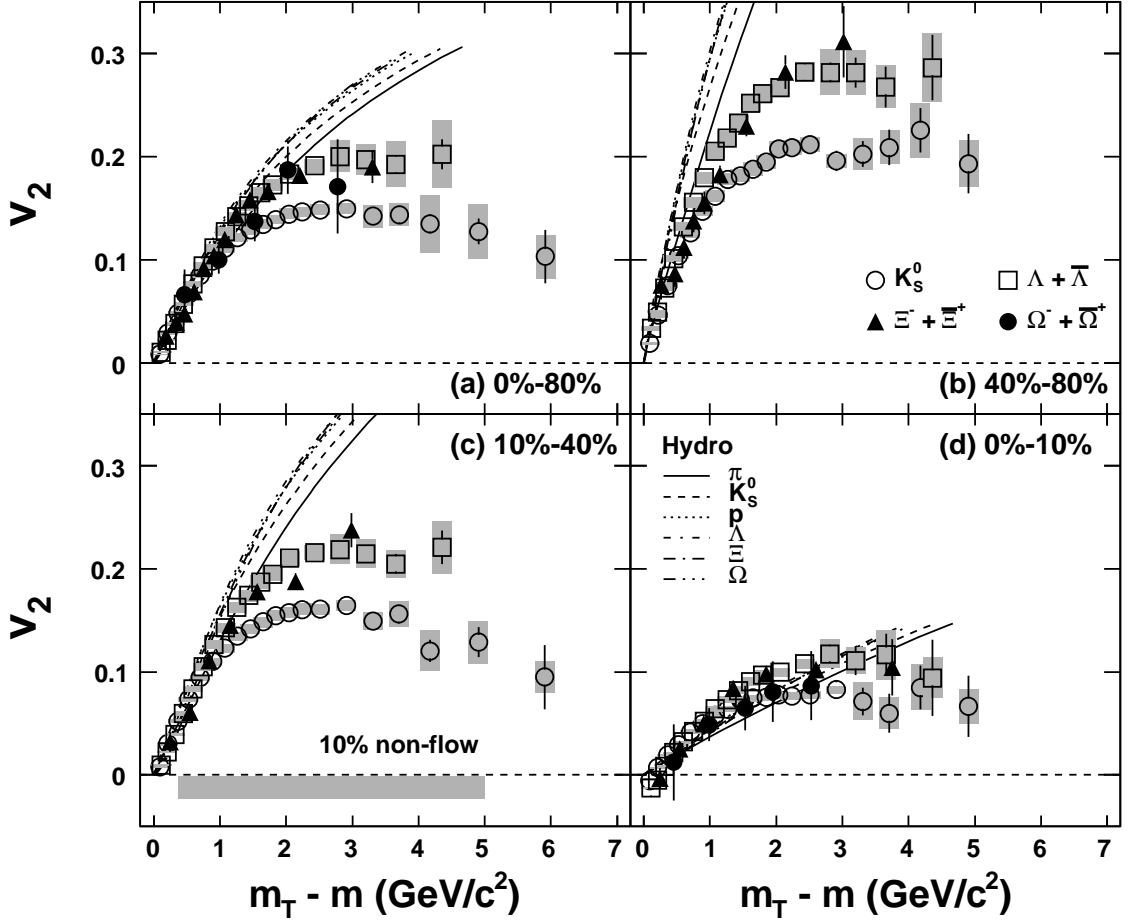


Figure 5.2: v_2 as a function of $m_T - m$ for (a) 0%–80%, (b) 40%–80%, (c) 10%–40% and (d) 0%–10% in Au + Au collisions at $\sqrt{s_{NN}} = 200$ GeV. Open circles, open squares, solid triangles and solid circles represent K_S^0 , $\Lambda + \bar{\Lambda}$, $\Xi + \bar{\Xi}$ and $\Omega + \bar{\Omega}$, respectively. Hydro calculations are shown for comparison [Huo05a].



5.1.4 NQ Scaling

Recently, many models try to explain meson-baryon differences in v_2 at intermediate p_T region, such as coalescence/recombination models. In these models, hadrons are formed at hadronization by combining two or three co-moving quarks. According to these models, the hadron $v_2(v_2^h)$ is related to the quark $v_2(v_2^q)$ by the relationship:

$$v_2^h(p_T) \simeq n_q v_2^q(p_T/n_q) \quad (5.1)$$

where n_q is equal to 2 for meson and 3 for baryon. Thus, v_2 may follow the Number-of-Quark scaling. This scaling is observed in Au + Au collisions at RHIC energies [Ada04b].

With high statistics, we can test the NQ scaling to high precision. Figure 5.3 shows v_2 from minimum bias Au + Au collisions at $\sqrt{s_{NN}} = 200$ GeV scaled by the number of constituent quarks (n_q) as a function of p_T/n_q (a) and $(m_T - m)/n_q$ (b) for K_S^0 , $\Lambda + \bar{\Lambda}$, $\Xi + \bar{\Xi}$ and $\Omega + \bar{\Omega}$. In order to investigate the scaling, a polynomial function has been fit to the scaled values of v_2 for all hadron species. The n_q -scaled v_2 in top panel is divided by the polynomial function. The ratios are plotted in the bottom panel as a function of p_T/n_q (c) and $(m_T - m)/n_q$ (d). Look at the (c), at low p_T/n_q region, the values of ratios from the top to the bottom have the mass ordering of low- p_T v_2 , which is seen for hydro models. As p_T/n_q increases, the difference of ratios between different particles becomes smaller and smaller and then ratios for baryons and mesons are close to 1 for $1 \text{ GeV}/c < p_T/n_q < 2 \text{ GeV}/c$ showing the NQ-scaling. The ratios for meson are systematically above one while the ratios for baryons are systematically lower than one. The current statistical errors do not exclude some strangeness content dependence for differences observed between $\Lambda + \bar{\Lambda}$, $\Xi + \bar{\Xi}$ and $\Omega + \bar{\Omega}$. The v_2 follows the NQ-scaling for p_T scale. In panel (d), the ratios as a function of $(m_T - m)/n_q$ are consistent with unit. NQ-scaling seems to work better for $(m_T - m)$ scale than p_T scale. Panel (b) combines $m_T - m$ scaling and NQ scaling together. This combined scaling works because in the range where v_2 is linear as a function of $m_T - m$, the v_2 scaled by n_q does not change the shape of the curves. Once we observed that all particles v_2 is a linear function of

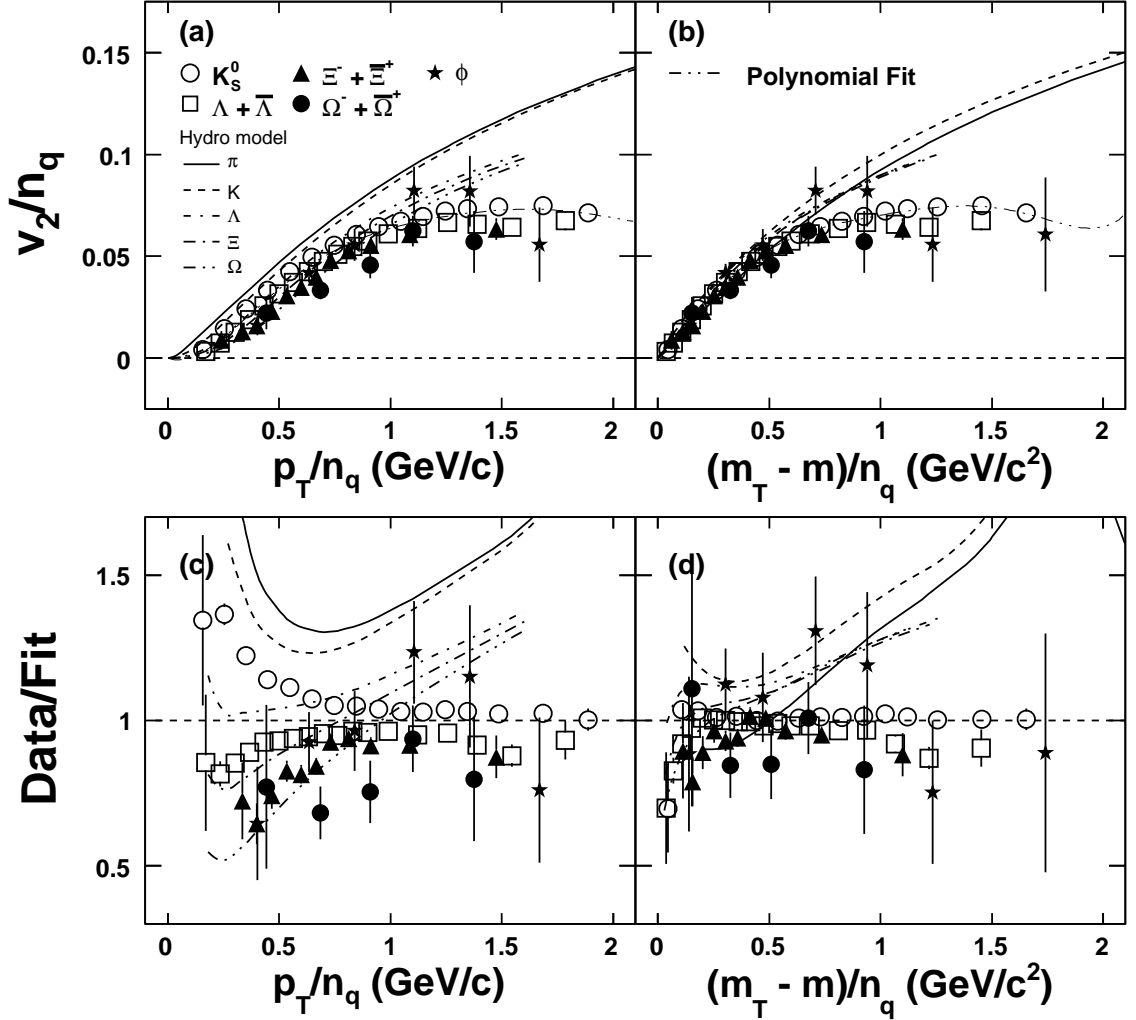


Figure 5.3: Identified particle v_2 from minimum bias Au + Au collisions at $\sqrt{s_{NN}} = 200$ GeV scaled by the number of quarks in the hadron (n_q) versus (a) p_T/n_q and (b) $(m_T - m)/n_q$. For each case, a polynomial fit to all particles is shown in dashed line. The ratio of v_2/n_q from data and hydro model to the fit function are shown in the (c) and (d).

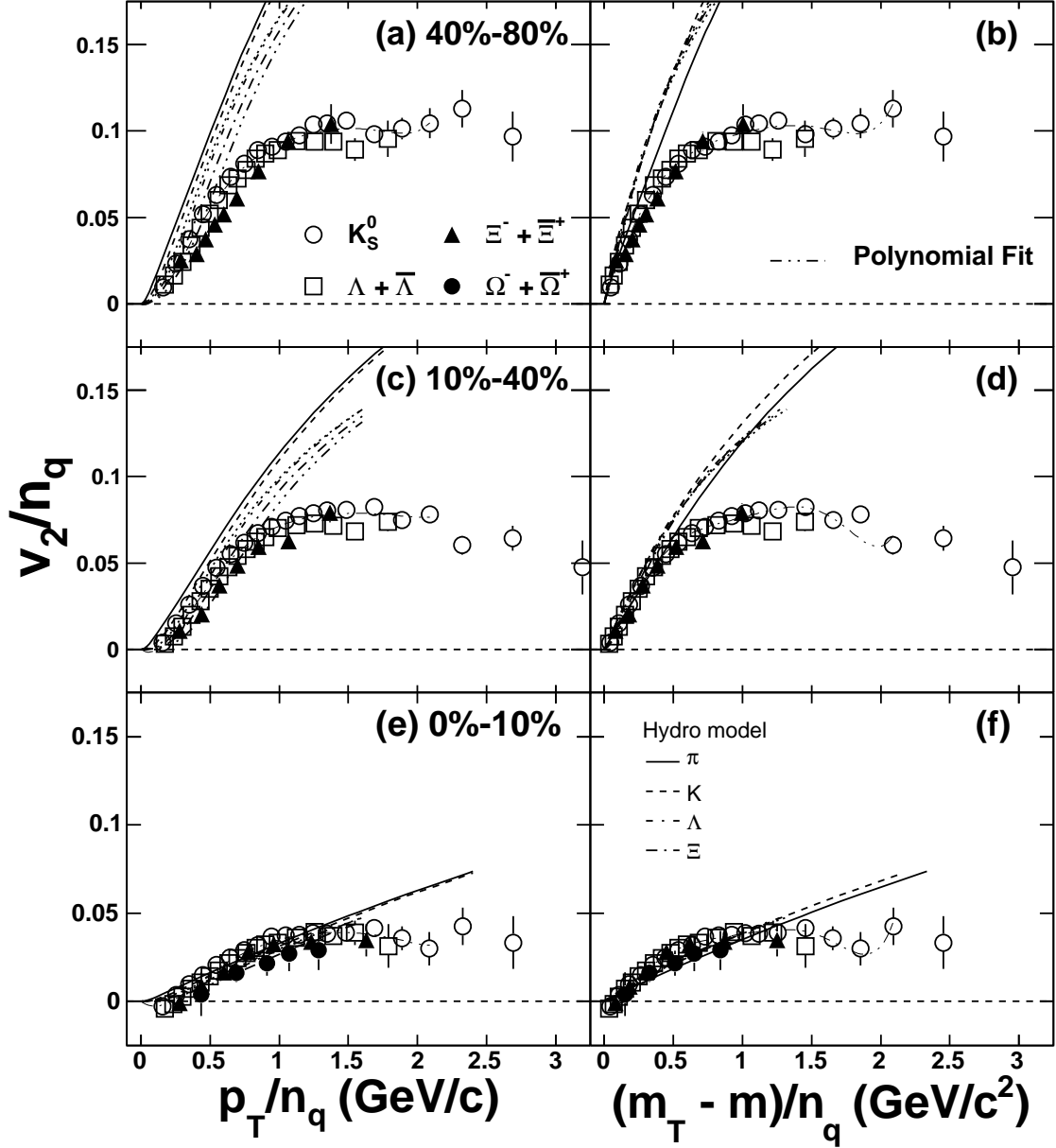


Figure 5.4: Centrality dependence of v_2/n_q versus p_T/n_q (left column) and $(m_T - m)/n_q$ (right column) for identified particles in Au + Au collisions at $\sqrt{s_{NN}} = 200$ GeV. The highest panels (a) and (b) are for 40%-80%. The middle panels (c) and (d) are for 10%-40%. The lowest panels (e) and (f) are for 0%-10%. The polynomial fit to all particles is done for p_T and $m_T - m$ scale, separately. Hydro results are drawn for comparisons.

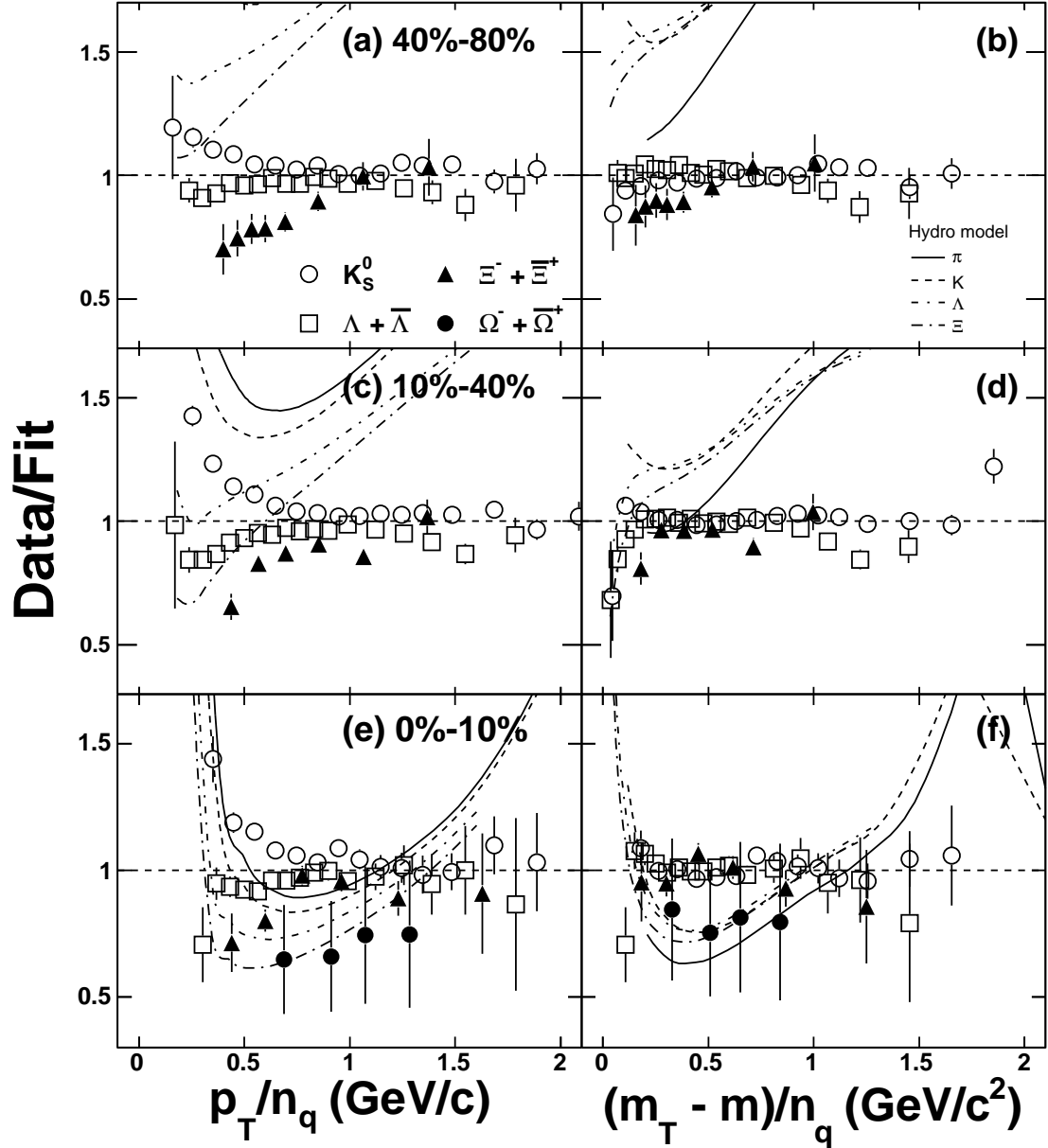


Figure 5.5: Centrality dependence of the ratio of v_2/n_q to the fitted polynomial function as a function of p_T/n_q (left column) and $(m_T - m)/n_q$ (right column) in Au + Au collisions at $\sqrt{s_{NN}} = 200$ GeV. Ratios from data and hydro models are shown as symbols and lines, respectively. The highest panels (a) and (b) are for 40%-80%. The middle panels (c) and (d) are for 10%-40%. The lowest panels (e) and (f) are for 0%-10%.

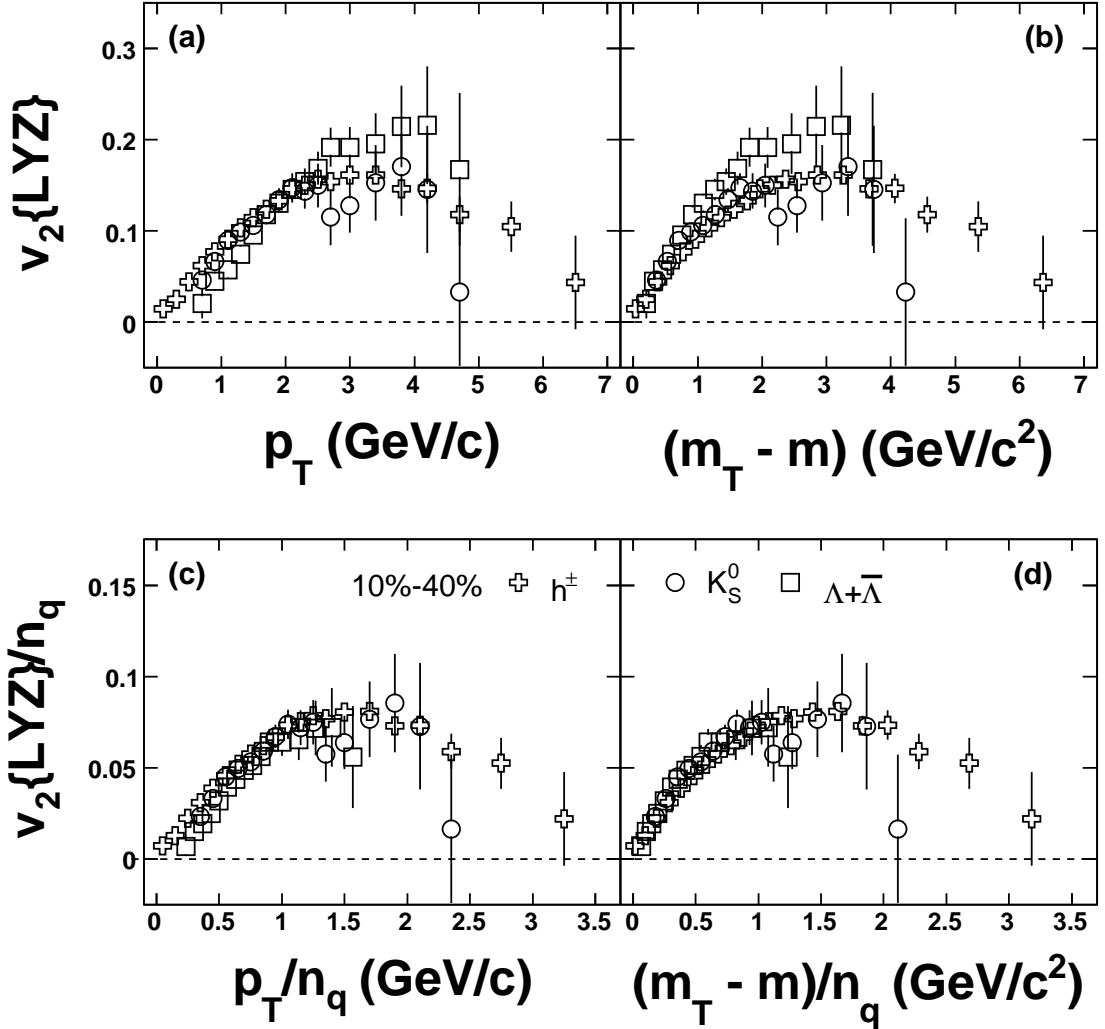


Figure 5.6: v_2 results from Lee-Yang Zero method for 10%-40% centrality bin in Au + Au collisions at $\sqrt{s_{NN}} = 200$ GeV. Circles, squares and crosses represent K_S^0 , $\Lambda + \bar{\Lambda}$ and charged particle respectively. (a): p_T dependence, (b): $m_T - m$ dependence, (c): n_q -scaling for p_T scale and (d): n_q -scaling for $m_T - m$



$m_T - m$, v_2 can be scaled by any number. At low $m_T - m$ region, v_2 scaled by n_q tells us nothing about coalescence or recombination.

Now let us look at the NQ-scaling for different centralities. Figure 5.4 shows centrality dependence of NQ-scaling in Au + Au collisions at $\sqrt{s_{NN}} = 200$ GeV. The left column shows v_2/n_q versus p_T/n_q . The right column shows v_2/n_q versus $(m_T - m)/n_q$. The top panel, middle panel and bottom panel are shown for 40%-80%, 10%-40% and 0%-10%, respectively. To investigate the scaling, a polynomial function has been fit to the n_q -scaled v_2 for all particles in each centrality interval for p_T and $m_T - m$ scale, separately. The v_2/n_q scaled by the polynomial fit are plotted in Figure 5.5 in corresponding centrality. We observe similar behaviors for different centralities as minimum bias: 1. hydro-like mass ordering at low v_2/n_q . 2. at intermediate p_T , v_2 is consistent with NQ-scaling. 3. $m_T - m$ scale shows better scaling behavior than p_T scale.

Lee-Yang Zero method is supposed to suppress non-flow effects. We should test all these observations with Lee-Yang Zero method. v_2 from Lee-Yang Zero method for 10%-40% centrality bin in Au + Au collisions at $\sqrt{s_{NN}} = 200$ GeV is shown in Figure 5.6. Circles, squares and crosses represent K_S^0 , $\Lambda + \bar{\Lambda}$ and charged particle, respectively. The n_q and mass of charged particle is assumed to be equal to 2 and 0.13 GeV/ c^2 as pion, respectively. Only 10%-40% centrality bin is presented since Lee-Yang Zero method has large errors in more peripheral and more central collisions due to small signal-to-noise ratio. We can see that the $m_T - NQ$ scaling holds for K_S^0 , $\Lambda + \bar{\Lambda}$ and charged particle at 10%-40% centrality bin.

The conclusions from above results are:

1. There is a clear number-of-quark scaling at intermediate p_T and better scaling in K_T for all hadrons studied here but no scaling is observed at low p_T .
2. The hydrodynamic model results do not show any scaling over the region $0.2 \leq p_T \leq 5$ GeV/ c .
3. These results are true for all centrality bins.



5.1.5 ε_{part} Scaled v_2

In order to analyze the centrality dependence of the scaling properties, we further normalize the n_q -scaled elliptic flow v_2 by the participant eccentricity ε_{part} to remove the initial geometry effect. Figure 5.7 (a) and (b) show v_2/n_q scaled by the mean eccentricity of the initial overlap region as a function of p_T/n_q and $(m_T - m)/n_q$ for K_S^0 , $\Lambda + \bar{\Lambda}$ and $\Xi + \bar{\Xi}$ in 0%-10%, 10%-40% and 40%-80% Au + Au collisions at $\sqrt{s_{NN}} = 200$ GeV, respectively. This eccentricity is referred to the participant eccentricity (ε_{part}). ε_{part} is calculated from the spatial distribution of participating nucleons using the Monte-Carlo Glauber model. The coordinate system is shifted to the (0,0) of the center-of-mass frame and rotated to make the eccentricity as maximum as possible. ε_{part} is calculated from the mean x and y positions of the participating nucleons in the shifted and rotated coordinate system.

Both plots show an initial rise and a turn over to a flat region in the higher p_T region. It is interesting to see that at a given centrality, the elliptic flow of all hadrons are scaled as observed in the minimum bias case. More interestingly, the turn-over to the flat region of the doubly scaled quantities occurs at a higher transverse momentum for more central collisions. After the geometric effect is removed, the build up of a stronger collective motion in more central collisions becomes obvious in the measured elliptic flow. This is consistent with the hydrodynamic model calculations, shown as lines in the right plot, although the model results are much closer together. However, neither our data nor the model results indicate the universal ε_{part} scaling claimed by PHENIX [Ada06a].

To further clarify the issue, instead of dividing the measured v_2 by the corresponding eccentricity ε_{part} , we plot $v_2(m_T - m)/(n_q \times \langle v_2 \rangle)$ for K_S^0 , Λ , and Ξ , in Fig. 5.7 (c). The values of $\langle v_2 \rangle$ are obtained by averaging v_2 as a function of transverse momentum weighted with the measured spectra. As one can see in the figure, for a given hadron, this scaling seems to work better. However, different hadrons seem to have different values of v_2 , especially for the top 10% centrality bin at the higher m_T .

Figure 5.7 (d) shows the doubly scaled v_2 again. But this time, the integrated values of v_2 are extracted from the measurements of unidentified charged hadrons $\langle v_2 \rangle_{ch}$ at the

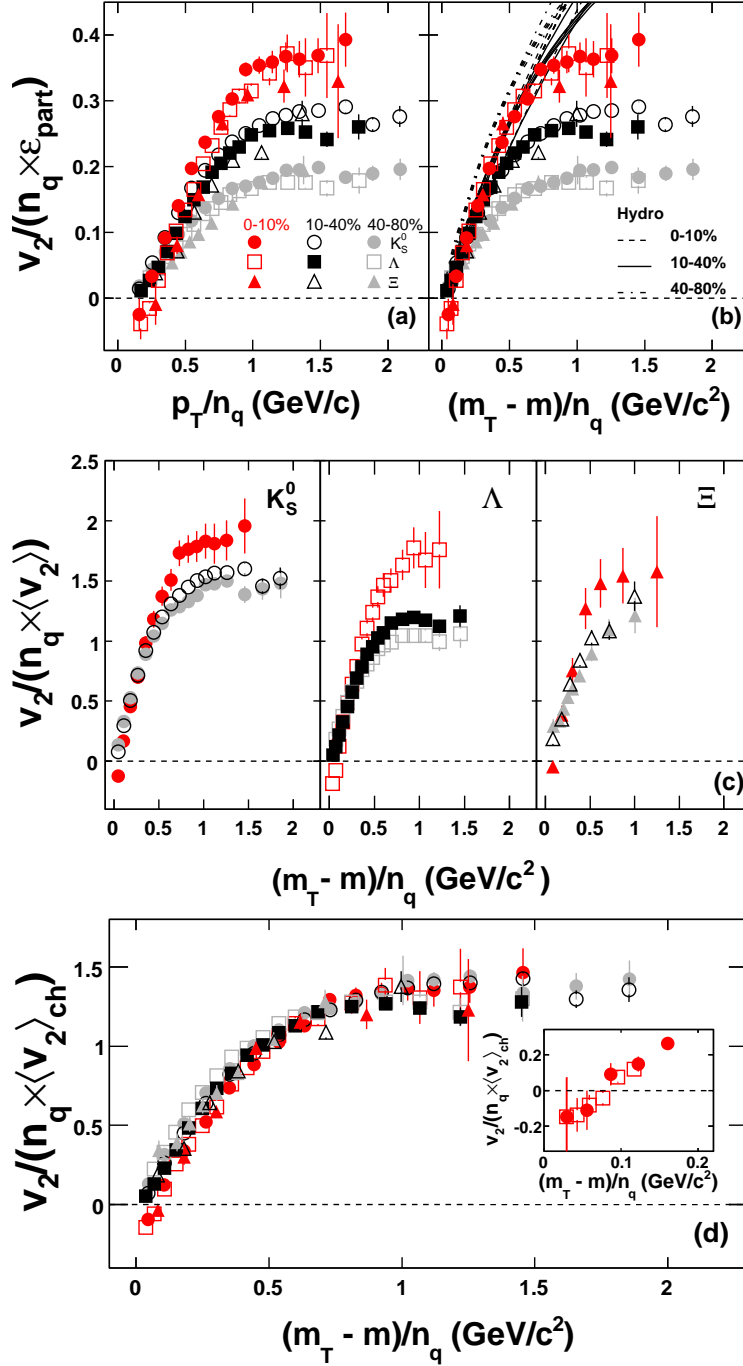


Figure 5.7: v_2 scaled by the number of quarks (n_q) and participant eccentricity (ϵ_{part}) ($v_2/(n_q \epsilon_{part})$) of identified particles versus (a) the scaled p_T/n_q and (b) $(m_T - m)/n_q$ for three centrality bins. For comparison, hydrodynamic model calculations [Pas06a] are shown as lines in (b). In (c) is shown the data from (b) scaled by the integrated v_2 of each particle, instead of ϵ_{part} . In (d) is shown the data from (a) scaled by the integrated v_2 of all charged hadrons. The insert in (d) expands the low p_T region.



corresponding centrality bins. In this case, it appears that the scaling works better. It is interesting to point out that at the most central bin, see inset in Fig. 5.7 (d), the values of v_2 become negative at low p_T for all hadrons. This is most likely caused by the strong radial flow developed in central Au+Au collisions [Pas01a]. Similar behavior has also been observed in v_2 of \bar{d} and Λ at RHIC [Liu06a] and SPS [Alt07a].

Whether the system is thermalized is one of issues in terms of QGP formation. Both theory and experiment draw attention to this issue. The values of integrated v_2 increases when collision centrality decreases. This is because the eccentricity ε is the largest for most peripheral collisions. In case of local thermalization, the centrality dependence in v_2/ε should disappear.

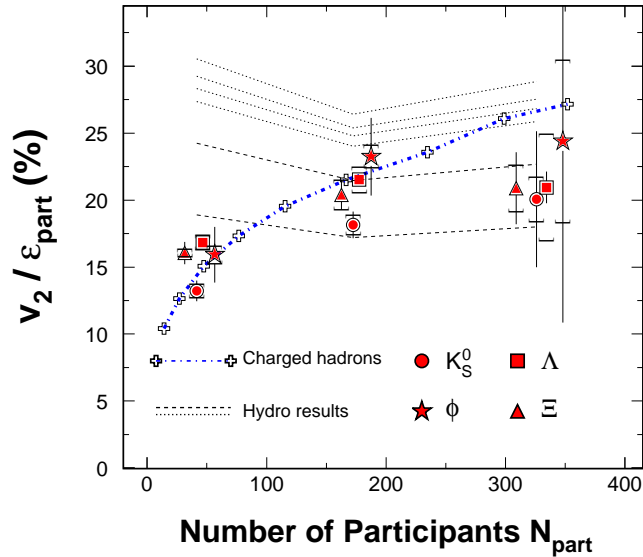


Figure 5.8: v_2/ε_{part} versus number of participants for charged hadrons (crosses), K_S^0 (circles), ϕ (stars), Λ (squares) and Ξ (triangles). Both charged and identified hadron v_2 were analyzed with the standard event plane method. All data are from 200 GeV Au+Au collisions. The data points are displaced slightly horizontally for clarity. The statistical uncertainties and the systematic uncertainties are shown as bars and brackets, respectively. Hydrodynamic model calculations are also shown as dashed lines [Pas06a] for, from top to bottom, Ω , Ξ , Λ , K , and π .

The centrality dependence of the ratio of the integrated elliptic flow over the eccen-



tricity (v_2/ε_{part}) for charged hadrons, K_S^0 , ϕ -meson and Λ are shown in Fig. 5.8. All these results are from the event-plane method and the number of participants is the average in the centrality bin. For comparison, results from a hydrodynamic calculation [Pas06a] are also shown as dashed lines. This ratio, to some extent reflects the strength of the collective expansion. At more central collision, one would expect a stronger expansion, hence the larger value of the ratio. This is what one sees in Fig. 5.8 for charged hadrons. For identified hadrons, the increasing trend as a function of N_{part} is there despite the large error bars. In the hydrodynamic calculations [Pas06a], the first order phase transition and freeze-out temperatures are set to be 165 MeV and 130 MeV, respectively. With these parameters, the hydrodynamical model results describe the produced pion, kaon and proton transverse momentum spectra [Pas06a]. In a pure hydrodynamic model, one deals with energy-momentum cells rather than any specific type of hadrons, thus the initial condition, the equation of state and the freeze-out conditions used in the calculation are the same for all hadrons. Such assumptions may not be applicable to all hadrons since some of them will continue to interact even after hydrodynamic freeze-out [Hir07a].

As expected in an equilibrium scenario, the model results show little sensitivity to the collision centrality. However, it is interesting to note that there is a clear hadron mass dependence of v_2 normalized by ε_{part} from the model calculations which is not seen in the data. It is not clear whether the mass dependence is from the collective motion at early time or is the effect of the hadronization process in the calculation. On the data side, the errors are too large to allow comparisons with model results. As one can see in Fig. 5.8, after $N_{part} \sim 170$, the measured ratios for the strange particles approach that from the hydrodynamic model calculations. The consistency between model results and data indicates that the system created in 200 GeV Au+Au collisions reaches local thermalization in central collisions when the number of participants is larger than ~ 170 .

5.1.6 Energy Dependence

The energy dependence of Λ and K_S^0 v_2 from minimum bias Au + Au collisions is depicted in Figure 5.9(a). All error bars are statistical only. Filled- and open-symbols



are from 200 GeV and 62.4 GeV collisions, respectively. Polynomial fits to both Λ and $K_S^0 v_2$ is performed and the results are shown as dashed lines in plot (a). The transverse momentum dependence of the ε -scaled v_2 ratios are shown in Figure 5.9(b). For the 0-80% Au+Au collision collisions, the values of the participant eccentricity from 62.4 and 200 GeV are 0.392 and 0.384, respectively. The ratios from ε -scaled v_2 and unscaled v_2 are similar due to the similarity in the participant eccentricity.

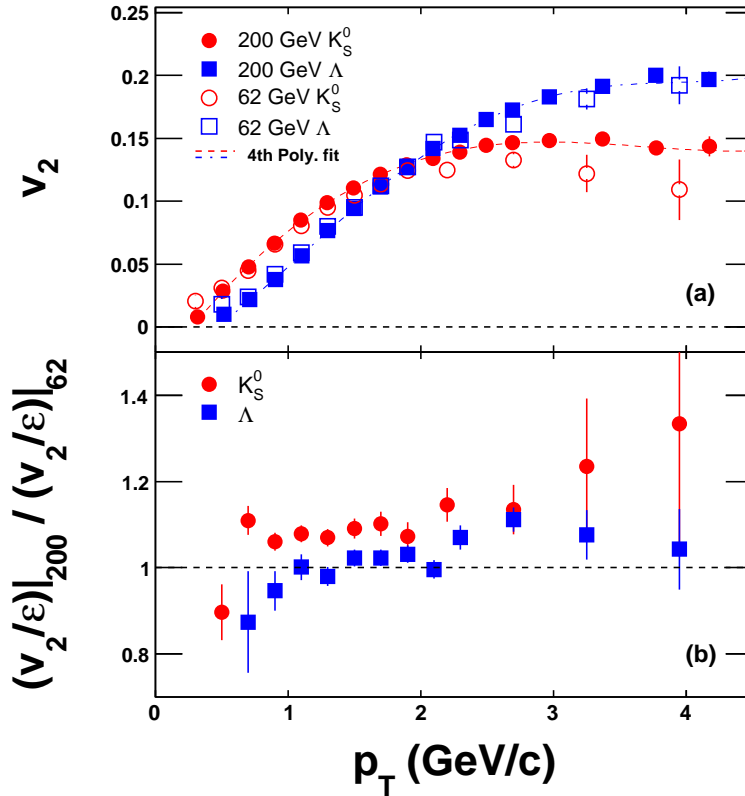


Figure 5.9: (a) Energy dependence of v_2 as a function of p_T . Polynomial fits (4^{th} order) to 200 GeV data are implemented in order to take ratios over 62.4 GeV. (b) ε scaled v_2 ratio of 200 GeV over 62.4 GeV as a function of p_T . Error bars are statistical only. The 62.4 GeV data is from [Abe07a].

It has been observed [Bac05a] that the charged multiplicity production is proportional to the squared root of the CM energy $dN/d\eta/\langle N_{part}/2 \rangle \propto \sqrt{s_{NN}}$. This implying a stronger flow is expected from higher energy collisions according to [Vol00a]. In Fig-



ure 5.9, the ratios for K_S^0 are about 5% larger than unity while the ratios for Λ are consistent with unity within error bars. PHOBOS experiment reported that the differences of v_2 between these two beam energies for charged hadrons are within a few percent [Alv06a]. According to [Vol00a], the multiplicity density at mid-rapidity defines the probability to collide among constituent particles. As discussed in [Bac05a], from 62 GeV to 200 GeV, the participant normalized charged hadron density at mid-rapidity increased by about 50%. However, we do not observe a strong change in v_2 expected from the huge increase in density at the similar size in the participant eccentricity. This indicates that a large fraction of the particle production occurred at the later stage of heavy ion collisions at these beam energies.

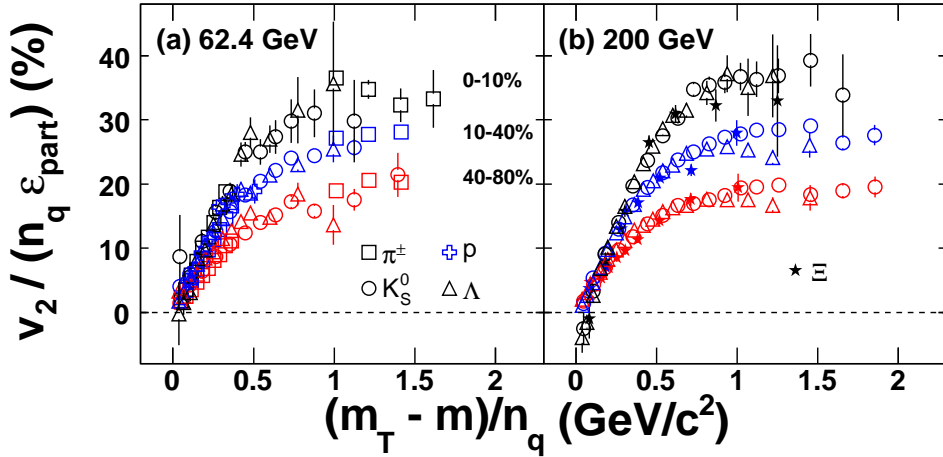


Figure 5.10: Centrality dependence of $v_2/(n_q \times \epsilon_{part})$ for identified hadrons from 62.4 GeV [Abe07a] (a) and 200 GeV (b) Au + Au collisions. Error bars are statistical only.

Figure 5.10 shows the centrality dependence of the number of quark and eccentricity normalized $v_2/(n_q \times \epsilon_{part})$ for identified hadrons from 62.4 GeV [Abe07a] (a) and 200 GeV (b) Au + Au collisions. Within error bars, data from both energy are similar. At the low transverse energy region, the scaled v_2 show almost a linear increase and then become flat. For more central collisions, the turning point occurs at a higher value of $(m_T - m)/n_q$. Recently, PHENIX has reported a charged hadron scaling with eccentricity, system size,



and the transverse kinetic energy $(m_T - m) \sim 1$ GeV [Ada06a]. As one can see from the figure, at given centrality, independent of the collision energy, there is a clear scaling: all values of $v_2/(n_q \times \epsilon_{part})$ clap into a single distribution. On the other hand, it is clear in the figure that at different centrality the shape of the distributions are different, meaning that there is no scaling in the measured v_2 with the eccentricity, especially in the higher transverse kinetic energy region.



CHAPTER 6

Summary and Outlook

In this thesis, we analyze 22,000,000 minimum bias events from Au + Au collisions at $\sqrt{s_{NN}} = 200$ GeV collected from STAR experiment at RHIC. We present results on elliptic flow v_2 of charged hadrons, K_S^0 and $\Lambda + \bar{\Lambda}$ from Au + Au collisions at $\sqrt{s_{NN}} = 200$ GeV. v_2 of K_S^0 and $\Lambda + \bar{\Lambda}$ from Au + Au collisions at $\sqrt{s_{NN}} = 62.4$ GeV are also presented. The results of v_2 from Lee-Yang Zero method for charged hadrons, K_S^0 and $\Lambda + \bar{\Lambda}$ are studied. The detailed study of centrality dependence of v_2 over a broad transverse momentum range is presented. The non-flow systematic errors are estimated from Lee-Yang Zero method and Event Plane method. We compare these results with multi-strange hadrons ϕ , Ξ and Ω for a complete study of strange and multi-strange hadron v_2 . Results from hydrodynamical calculations are discussed in detail. The energy dependence of v_2 as a function of centrality are also discussed.

In the low p_T region ($p_T < 2$ GeV/c), hydro-like mass ordering and a scaling with $m_T - m$ are observed for identified hadrons in each centrality bin. In the higher p_T region (2 GeV/c $< p_T < 5$ GeV/c), number-of-quark scaling is observed for all hadrons under study in each centrality bin. For the multi-strange hadron Ω , which does not suffer appreciable hadronic interactions, the values of v_2 are consistent with mass ordering, $m_T - m$ scaling at low p_T and number-of-quark scaling at intermediate p_T .

Participant eccentricity ε_{part} is scaled in order to remove the initial geometry effect. We do not observe $v_2(p_T)/\varepsilon_{part}$ scaling for different centrality bins. As a function of collision centrality, an increase in v_2/ε_{part} has been observed indicating a stronger collective flow in more central Au + Au collisions.

For hydrodynamical calculations with assumptions of local thermalization, v_2/ε shows



little sensitivity to centrality bins. The rate of increase in v_2/ε_{part} for data appears to slow down when $N_{part} > 170$ and approach that from the hydrodynamic model calculations. This indicates that the system created in 200 GeV Au + Au collisions reached local thermalization in central collisions when the number of participants is larger than 170. Further, the observed collectivity, $m_T - m$ scaling and number-of-quark scaling do not depend on local thermalization.

Full Time-of-Flight upgrade and construction of Heavy Flavor Tracker are two important upgrades of STAR detectors. They will significantly extend the STAR detection capabilities and physics program.

TOF upgrade will extend particle identification capability to the full azimuthal coverage and two units in pseudo-rapidity $-1.0 < \eta < 1.0$. This will benefit reconstruction of strange resonances especially Ω and ϕ . Systematic study of Λ , Ξ , Ω and ϕ will help us to understand strangeness production mechanism. Their v_2 measurements will further help us to determine s quark flow.

The primary motivation of HFT is to extend STAR's capability to measure heavy flavor production by the measurement of displaced vertices and to do the direct topological identification of open charm hadrons. A precise measurement of the spectra of D meson will shed light on several open questions in heavy ion collisions. From the spectra and production rate of D meson, we will be able to extrapolate to the total yield for charm quark production at RHIC. Due to high open charm production rate at RHIC, the coalescence process becomes relevant for charm production. Total charm cross section will serve as a baseline for J/Ψ measurements. This will help us to answer the question of whether J/Ψ mesons are suppressed or enhanced at RHIC. Due to the large mass, the heavy quark can be used to probe the properties of the medium created in heavy ion collisions. Due to the dead cone effect, heavy flavor should radiate less gluons, hence lose less energy in the dense medium. Currently, indirect measurements of non-photonic electrons as a measurement of the abundance of charm and bottom hadrons indicate unexpected high energy loss for heavy quarks and show inconsistency with pQCD models. Measurements of charmed meson R_{AA} will be very important with HFT. Another important measurement is a measurement of the elliptic flow of D mesons down to very



low p_T values. Flow of charm quarks can be taken as a probe of frequent re-scatterings of light quarks. Measurements of D meson v_2 will gain information on the thermalization among u , d , s quarks.



APPENDIX A

Anisotropic Flow at RHIC: How Unique is the Number-of-Constituent-Quark Scaling?

How much does the effect of hadronic cross sections, kinematics etc. contribute to the particle type dependence of v_2 ? To study this, we employ two independent hadron-string transport models RQMD(v2.4) and UrQMD(v2.2) [Sor95a, Ble99a].

Within the framework of the hadronic transport approach, a typical heavy ion collision proceeds schematically in three stages, i.e. the pre-hadronic (strings and constituent (di-)quarks) stage, the hadronic pre-equilibrium stage, the evolution towards hadronic kinetic equilibrium and freeze-out. The pre-hadronic stage involves the initial excitation and fragmentation of color strings and ropes. At the highest RHIC energy, this stage lasts for about 0.5-1.5 fm/c and the effective transverse pressure/EOS is rather soft. During the late hadronic stage, the hadronic system approaches local kinetic equilibrium followed by an approach to free-streaming, where the system escapes equilibrium due to dilution of the hadronic gas: the mean free path of the hadrons exceeds the finite size of the system [Sor95a, Ble99a, Hec98a], the free streaming hadrons decay and feed down to the lightest species.

Figure A.1 presents the model results on the centrality dependence of the charged hadron v_2 -values along with measurements from the STAR collaboration [Ack01a, Ada05c]. Both hadronic transport models (UrQMD v2.2 and RQMD v2.4) reach about 60% of the measured v_2 values only, although the centrality dependencies are very similar to the data. There is a small variance between the two models, which we consider as an estimate of the systematic errors in such model calculations. Although the v_2 values from the hadronic transport model also depend on the formation-time of hadrons from

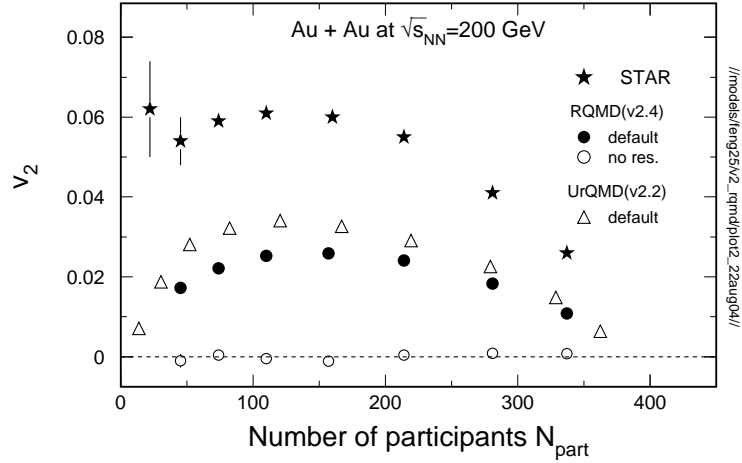


Figure A.1: Charged hadron v_2 versus the number of participating nucleons in Au+Au interactions at $\sqrt{s_{NN}} = 200$ GeV. Experimental data [Ack01a, Ada05c] from the 4-particle cumulant method is shown as stars. RQMD results are depicted by filled circles (full calculation) and open circles (without rescattering). The UrQMD calculations are shown as open triangles.

strings [Ble02a], the failure of both hadronic transport models to describe quantitatively the magnitude of v_2 is a strong indication that there are interactions amongst pre-hadronic constituents (partons) present in nature (but not in the hadron-string models discussed here), which are responsible for the large v_2 values observed in the experiments [Bur04a, Bra04a]. When rescattering between the hadrons is turned off (full circles), v_2 vanishes completely, because repulsive vector interactions are not included into the present simulations [Sto81a, Sto86a, Ble02a].

How much of the observed NCQ-scaling features can be reproduced by the hadronic models? In both dynamical approaches, finite (vacuum) cross sections are used to model the strong interactions in the hadron-string cascade. Unlike the simplistic Cooper-Frye freeze-out treatment in most hydrodynamic calculations, the transition from strongly interacting matter to free-streaming is determined here by the interplay of the local particle density and the energy dependent cross section of the individual hadrons. It is well known that a proper treatment of the gradual freeze-out is crucial for the finally observed hadron distributions. It was pointed out that the hydrodynamical results on



flow depend strongly on the proper kinetic treatment of the freeze-out process and can not be approximated by isotherms [Hun98a, And99a, Mag99a].

However, the major shortcoming of the present hadron-string approach is the lack of the early partonic interactions which are important for the early dynamics in ultra-relativistic heavy ion collisions [Bas99a, Sto81a, Sto86a, Ble02a, Hir05a]. In order to take care of both partonic and hadronic interactions in high-energy nuclear collisions, a combination of the hydrodynamic model for the early stage dynamics (the “perfect” fluid stage) with a hadronic transport model for the later stage plus freeze-out has been proposed [Bas99b, Dum99a, Bas00a, Tea01a, Non05a, Hir05b]. Fig. A.2 shows the collision centrality dependence of the p_T -dependent v_2 values for π , K , p , and Λ . Both, the hydrodynamic behavior (in the low p_T region) and a hadron-type dependence (in the intermediate p_T region) are clearly predicted in all centrality bins. This “crossing and subsequent splitting” between meson- and baryon elliptic flow as well as the breakdown of the hydrodynamical mass scaling at high transverse momenta was first predicted within the UrQMD model [Ble02a] and has later been observed in the experimental data. It is important to note that the more recent explanations of this effect (the suggested “number-of-constituent-quark” scaling) is not a unique feature of the “quark recombination/coalescence” assumption: hadronic interactions alone have quantitatively (at the correct p_T -values) predicted this hadron type dependence.

Let us explore the p_T -dependence of the event anisotropy parameters in detail. Figure A.3 shows the calculated unscaled and scaled v_2 values of various hadrons versus the unscaled and scaled transverse momenta, p_T , of the various hadrons. On the left hand side (Figure A.3(a)) one can see that at lower transverse momenta, $p_T \leq 1.5$ GeV/c, the heavier hadrons exhibit smaller v_2 values than the lighter hadrons: Hadron transport theory predicts mass ordering. The Ξ and Ω v_2 values from the UrQMD calculations are also included. They are the lowest of all v_2 values for $p_T \leq 2$ GeV/c. Such mass ordering is exactly what is observed in the experimental data [Ada04b] and is in accord with hydrodynamic calculations [Huo03a]. Hence, hadronic interactions, which do take place at later stages of the collisions, also do contribute to the observed collective motion.

At higher p_T values, this mass dependence gives way to the $v_2(p_T)$ -dependence on

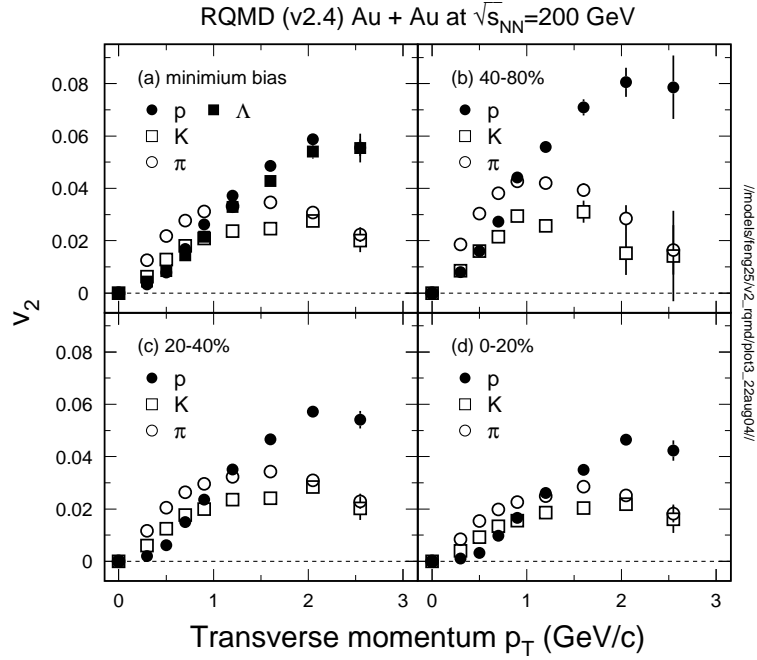


Figure A.2: RQMD results of π , K , p , and Λ v_2 from Au+Au collisions at $\sqrt{s_{NN}} = 200$ GeV. (a) Minimum bias collisions: At about $p_T \sim 1.2$ GeV/c, baryon and meson v_2 are crossing each other; (b) 40-80%; (c) 20-40%; (d) 0-20%.

the hadron type (i.e. meson or baryon). Here, it is interesting to note that the Ω -baryons seemingly acquire a significant amount of v_2 in the model calculations. In addition, there is also clear, but small difference for kaons and pions in v_2 values at $p_T \geq 1.5$ GeV/c. This particle type dependence, rather than the otherwise dominating particle mass dependence, is also observed in the data [Ada04b]. It is important to note that the ϕ meson has a mass that is very close to the mass of the baryons p and Λ , and, indeed, recent experimental results on the ϕ 's v_2 values are similar to other mesons [Old05a]. However, in the hadronic transport model, about 2/3 of the ϕ -mesons are formed via $K\bar{K}$ -coalescence, which is not necessarily the dominant process in heavy ion collisions [Ada05d]. Therefore, the v_2 values of ϕ meson are not shown in Figure A.3. It should also be noted that in the high p_T region, $p_T \geq 2.5$ GeV/c, all v_2 values start to decrease. This indicates that the system is deviating from an ideal hydrodynamic behavior. This trend is best seen in the right, “scaled”, plot in Fig. A.3. Such a drop

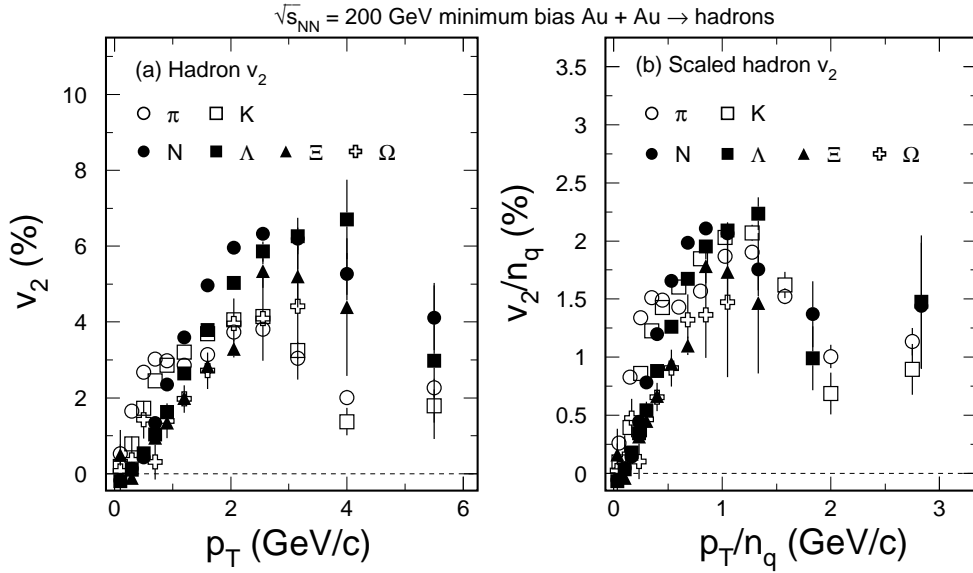


Figure A.3: (a) Hadron v_2 from minimum bias Au+Au collisions at $\sqrt{s_{NN}} = 200$ GeV; (b) Scaled hadron v_2 results are shown. The n_q refers to the number of constituent quarks. Symbols represent results from the UrQMD (v2.2) model for various hadron species. At low $p_T/n_q \leq 0.5$ GeV/c, π does not follow the scaling perhaps caused by the resonance decay [Don04a]. In higher p_T region, K meson seems to fall off the scaling curve due to the comparatively small hadronic cross sections in the model.

has been observed in the data.

The test of the NCQ scaling hypothesis is shown in Figure A.3(b), which depicts the scaled hadron values, v_2/n_q . The scaling factor is the number of constituent quarks (NCQ) in accord with the coalescence approach [Vol02a, Fri04a, Hwa04a]. For mesons and baryons, $n_q = 2$ and $n_q = 3$, respectively. The NCQ-scaling is clearly observed in both RQMD (not shown here) and UrQMD model calculations except for the pions. This surprising result and its implications for the frequently invoked recombination/coalescence hypothesis will be discussed in the last section.

However, one should note that there are experimentally distinguishable differences (when differential Ω elliptic flow data with good statistics becomes available) between “real” NCQ scaling from coalescence and the approximate NCQ scaling due to the cross section hierarchy discussed here. In the coalescence approach one expects identical elliptic flow of all baryons irrespective of their type. In contrast, the present AQM scaling



picture, leads to an observable ordering of the elliptic flow at fixed p_T according to the strangeness content. This can indeed be observed in Fig. A.3, where an ordering of the elliptic flow values can be observed: $v_2(N) > v_2(\Lambda) > v_2(\Xi) > v_2(\Omega)$.

The particle and energy density is highest at the center of the created fireball in relativistic nuclear collisions - initially, there is an angular dependent matter density gradient. The repulsive interactions among the constituents will therefore push matter to move outwards. In this way, the collective flow develops in nucleus-nucleus collisions [Bas99a, Sto81a, Sto86a, Sor97b, Oll92a, Rei04a]. We would like to stress that flow means matter and energy flow. It is independent of the type of particles, either partons or hadrons, or different kinds of hadrons. Hence, by studying the collective motion of the produced hadrons one can, in principle, extract the information of early collision dynamics [Sor97b, Oll92a, Xu04a]. In general, one expects that the final elliptic flow,

$$v_2(p_T) \propto \int_t \int_\Sigma \sigma(\rho, p_T) \otimes \rho_\Sigma(t, x, y, p_T) d\vec{A}_\Sigma(x, y) dt, \quad (\text{A.1})$$

where Σ denotes the hyper-surface where hadrons are emitted, will depend on σ , i.e. the interaction cross section, which, in principle, depends on the particle type, cm angle and relative momenta. The specific particle density depends on the collision time t , location, and momentum. For short mean free paths, the transverse flow is intimately related to the pressure, which in turn depends on the density and temperature of the matter under study [Bas99a, Sto81a, Sto86a, Sor97b, Oll92a, Rei04a, Ble02a]. Indeed, the frequent rescatterings among the hadrons can lead to hydrodynamic-like mass ordering in the low p_T region.

At the higher transverse momenta, $p_T \geq 1.5$ GeV/c, the particles escape quickly from the system to low density, in effect leading to early freeze-out and lack of development of the hydrodynamics and the details of the interaction cross-sections are most important. As the cross sections depend on the particle type, for mesons or baryons to first approximation given by the constituent quark model [Vol02a], we do expect roughly a 2:3 scaling of the meson-to-baryon elliptic flow from transport calculations.

The hadronic models underpredicted the strength of v_2 at RHIC, because early partonic interactions (except from quark coalescence during the string break-up) are not



included in the model. The early stage with highest density and smallest mean free paths is “missing”. This shortcoming of the hadronic models clearly demonstrates the need for the early, dense partonic interactions in heavy ion collisions at RHIC.



References

- [Abe03a] J. Abele et al. *Nucl. Instru. Methd A*, **499** 692, 2003.
- [Abe07a] B. I. Abelev et al. *Phys. Rev. C*, **75** 054906, 2007.
- [Ack01a] K. H. Ackermann et al. *Phys. Rev. Lett.*, **86** 402, 2001.
- [Ack03a] K. Ackermann et al. *Nucl. Instru. Methd A*, **499** 624, 2003.
- [Ack03b] K. Ackermann et al. *Nucl. Instru. Methd A*, **499** 709, 2003.
- [Ada03a] M. Adamczyk et al. *Nucl. Instru. Methd A*, **499** 437, 2003.
- [Ada03b] J. Adams et al. *Phys. Rev. Lett*, **91** 072304, 2003.
- [Ada04a] J. Adams et al. *Phys. Rev. Lett.*, **92** 182301, 2004.
- [Ada04b] J. Adams et al. *Phys. Rev. Lett.*, **92** 052302, 2004.
- [Ada05a] J. Adams et al. *Nucl. Phys. A*, **757**, 102, 2005.
- [Ada05b] J. Adams et al. *Phys. Rev. Lett.*, **95** 122301, 2005.
- [Ada05c] J. Adams et al. *Phys. Rev. C*, **72** 014904, 2005.
- [Ada05d] J. Adams et al. *Phys. Lett. B*, **612** 181, 2005.
- [Ada06a] A. Adare et al. *nucl-ex/0608033*
- [Adc03a] K. Adcox et al. *Nucl. Instru. Methd A*, **499** 469, 2003.
- [Adl02a] C. Adler et al. *Phys. Rev. Lett.*, **89** 202301, 2002.
- [Adl03a] C. Adler et al. *Phys. Rev. Lett.*, **90** 082302, 2003.
- [Agg03a] M. M. Aggarwal et al. *Nucl. Instr. Method A*, **499** 751, 2003.
- [All03a] C. E. Allgower et al. *Nucl. Instr. Method A*, **499** 740, 2003.
- [Alt07a] C. Alt et al. (NA49 Collaboration). *Phys. Rev. C*, **75** 044901, 2007.
- [Alv06a] B. Alver et al. *nucl-ex/0610037*
- [And99a] C. Anderlik et al. *Phys. Rev. C*, **59** 3309, 1999.
- [And03a] M. Anderson et al. *Nucl. Instr. Method A*, **499** 659, 2003.
- [Arn03a] L. Arnold et al. *Nucl. Instr. Method A*, **499** 652, 2003.
- [Bac03a] B. B. Back et al. *Nucl. Instr. Methd A*, **499** 603, 2003.
- [Bac05a] B. B. Back et al. *Nucl. Phys. A*, **757** 28, 2005.



- [Bar04a] O. Barannikova et al. *nucl-ex/0403014*.
- [Bas99a] S. A. Bass, M. Gyulassy, H. Stöcker, W. Greiner. *J. Phys. G*, **25** R1, 1999.
- [Bas99b] S. A. Bass et al. *Phys. Rev. C*, **60** 021902, 1999.
- [Bas00a] S. A. Bass, A. Dumitru. *Phys. Rev. C*, **61** 064909, 2000.
- [Bed03a] M. Beddo et al. *Nucl. Instr. Methd A*, **499** 725, 2003.
- [Bei03a] F. S. Beiser et al. *Nucl. Instr. Methd A*, **499** 762, 2003.
- [Bel03a] R. Bellwied, et al. *Nucl. Instr. Method A*, **499** 636, 2003.
- [Ber03a] F. Bergsma, et al. *Nucl. Instr. Method A*, **499** 629, 2003.
- [Bha03a] R. S. Bhalerao, N. Borghini, J.-Y. Ollitrault. *Nucl. Phys. A*, **727** 373, 2003.
- [Bia81a] S. F. Biagi et al. *Nucl. Phys. B*, **186** 1, 1981.
- [Ble99a] M. Bleicher et al. *J. Phys. G*, **25** 1859, 1999.
- [Ble02a] M. Bleicher, H. Stöcker. *Phys. Lett. B*, **526** 309, 2002.
- [Bon03a] B. Bonner et al. *Nucl. Instru. Method A*, **508** 181, 2003.
- [Bor01a] N. Borghini, P. M. Dinh, J.-Y. Ollitrault. *Phys. Rev. C*, **63** 054906, 2001.
- [Bra95a] P. Braun-Munzinger, J. Stachel, J. Wessels and N. Xu. *Phys. Lett. B*, **344** 43, 1995.
- [Bra99a] P. Braun-Munzinger, I. Heppe, J. Stachel. *Phys. Lett. B*, **465** 15, 1995.
- [Bra03a] P. Braun-Munzinger, K. Redlich, J. Stachel, in *Quark Gluon Plasma 3*, eds.
- [Bra04a] E. L. Bratkovskaya et al. *Phys. Rev. C*, **69** 054907, 2004.
- [Bre69a] M. Breidenbach et al. *Phys. Rev. Lett*, **23** 935, 1969.
- [Bur04a] G. Bureau, J. Bleibel, C. Fuchs, A. Faessler, L. V. Bravina, E. E. Zabrodin. *Phys. Rev. C*, **71** 054905, 2005.
- [Che03a] Y. Cheng, F. Liu, Z. Liu, K. Schweda, N. Xu. *Phys. Rev. C*, **68** 034910, 2003
- [Coo74a] F. Cooper and G. Frye. *Phys. Rev. D*, **10** 186, 1974.
- [Don04a] X. Dong et al. *Phys. Lett. B*, **597** 328, 2004.
- [Dum99a] A. Dumitru et al. *Phys. Lett. B*, **460** 411, 1999.
- [Eid04a] S. Eidelman et al. *Phys. Lett. B*, **592**, 2004.
- [Fri03a] R. J. Fries, B. Müller, C. Nonaka, S. A. Bass. *Phys. Rev. Lett.*, **90** 202303, 2003.



- [Fri04a] R. J. Fries. *J. Phys. G*, **31** S379, 2005.
- [Gel64a] M. Gell-Mann. *Phys. Letters*, **8** 214, 1964.
- [Gre03a] V. Greco, C. M. Ko, P. Levai. *Phys. Rev. Lett.*, **90** 202302, 2003.
- [Hec98a] H.van Hecke, H.Sorge, and N. Xu. *Phys. Rev. Lett.*, **81** 5764, 1998.
- [Hir05a] T. Hirano, M. Gyulassy. *nucl-th/0506049*
- [Hir05b] T. Hirano. *nucl-th/0510005*
- [Hir07a] T. Hirano, U.W. Heinz, D. Kharzeev, R. Lacey, and Y. Nara. *nucl-th/0701075*
- [Hua88a] K. Huang. *Statistical Mechanics*, John Wiley and Sons, 1988.
- [Hun98a] C. M. Hung, E. V. Shuryak. *Phys. Rev. C*, **57** 1891, 1998.
- [Huo01a] P. Huovinen, P. F. Kolb, U. Heinz, P. V. Ruuskanen and S. A. Voloshin. *Phys. Lett. B*, **503** 58, 2001.
- [Huo03a] P. Huovinen. “Private Communication (2003).”
- [Huo05a] P. Huovinen. *Nucl. Phys. A*, **761** 296, 2005.
- [Huo06a] P. Huovinen and P.V. Ruuskanen. Submitted to *Ann. Rev. Nucl. Part. Sci.*, May 2006.
- [Hwa03a] R. C. Hwa, X. N. Wang. *World Scientific, Singapore*, 2003.
- [Hwa04a] R. C. Hwa and C.B. Yang. *Phys. Rev. C*, **70** 024904, 2004.
- [Kar02a] F. Karsch. *Nucl. Phys. A*, **698** 199, 2002.
- [Kol03a] P. F. Kolb, U. Heinz. *nuch-th/0305084*.
- [Leb02a] A. Lebedev. *Nucl. Instru. Method A*, **478** 163, 2002.
- [Lin02a] Z. W. Lin, C. M. Ko. *Phys. Rev. Lett.*, **89** 202302, 2002.
- [Liu06a] H. Liu et al. (STAR Collaboration). proceedings of Quark Matter 2006 Conference, Shanghai, November 2006; *nucl-ex/0701057*.
- [Mag99a] V. K. Magas et al. *Heavy Ion Phys.*, **9** 193, 1999.
- [Mar98a] S. Margetis. *STAR Note 0367*, 1998.
- [Mat03a] H. S. Matis et al. *Nucl. Instru. Method A*, **499** 802, 2003.
- [Mil03a] M. Miller. *PhD thesis*, Yale University, 2003.
- [Mul72a] R. A. Muller. *Phys. Lett. B*, **38** 123, 1972.
- [Non05a] C. Nonaka, S. A. Bass. *nucl-th/0510038*



- [Old04a] M. Oldenburg et al. *J. Phys. G*, **31** S437, 2004.
- [Old05a] M. Oldenburg et al. *nucl-ex/0510026*
- [Oll92a] J.-Y. Ollitrault. *Phys. Rev. D*, **46** 229, 1992.
- [Oll93a] J.-Y. Ollitrault. *Phys. Rev. D*, **48** 1132, 1993.
- [Pas01a] P. Huovinen, P. Kolb, U. Heinz, P.V. Ruuskanen, and S.A. Voloshin. *Phys. Lett. B*, **503** 58, 2001.
- [Pas06a] P. Huovinen and P.V. Ruuskanen. Submitted to *Ann. Rev. Nucl. Part. Sci.*, May 2006.
- [Rei04a] W. Reisdorf, H.G. Ritter. *Ann. Rev. Nucl. Part. Sci.*, **47** 663, 1997.
- [Rut11a] E. Rutherford. *Phil. Mag*, **21** 669, 1911
- [Rut14a] E. Rutherford. *Phil. Mag*, **27** 488, 1914
- [Sat00a] H. Satz. *Rept. Prog. Phys.*, **63** 1511, 2000.
- [Sch93a] E. Schnedermann, J. Sollfrank, and U. Heinz. *Phys. Rev. C*, **48** 2462, 1993.
- [Sor95a] H. Sorge. *Phys. Rev. C*, **52** 3291, 1995.
- [Sor97a] H. Sorge. *Phys. Lett. B*, **402** 251, 1997.
- [Sor97b] H. Sorge. *Phys. Rev. Lett.*, **78** 2309, 1997.
- [Sto81a] H. Stöcker, M. Gyulassy, J. Boguta. *Phys. Lett. B*, **103** 269, 1981.
- [Sto86a] H. Stöcker and W. Greiner. *Phys. Rept.*, **137** 277, 1986.
- [Tea01a] D. Teaney, J. Lauret, E. Shuryak. *nucl-th/0110037*
- [Tho897] J. J. Thomas. *Phil. Mag.*, **44** 293, 1897.
- [Tho02a] J. H. Thomas. *Nucl. Instru. Method A*, **478** 166, 2002.
- [Vol96a] S. Voloshin and Y. Zhang. *Z. Phys. C*, **70** 665, 1996.
- [Vol98a] A. M. Poskanzer and S. A. Voloshin. *Phys. Rev. C*, **58** 1671, 1998.
- [Vol00a] S. A. Voloshin and A. M. Poskanzer. *Phys. Lett. B*, **474** 27, 2000.
- [Vol02a] D. Molnar, S. Voloshin. *Phys. Rev. Lett.*, **91** 092301, 2003.
- [Vol06a] S. A. Voloshin. *arXiv: nucl-ex/0701038*, 2006.
- [Wan92a] X. N. Wang, M. Gyulassy. *Phys. Rev. Lett.*, **68** 1480, 1992.
- [Wan98a] X. N. Wang. *Phys. Rev. C*, **58** 2321, 1998.
- [Wan05a] X. N. Wang. *Nucl. Phys. A*, **750** 98, 2005.



- [Wil74] K. G. Wilson. *Phys. Rev. D*, **10** 2455, 1974.
- [Wie06a] H. Wieman et al. *Technical Report*, 2006.
- [Xu02a] N. Xu, M. Kaneta. *Nucl. Phys. A*, **698** 306c, 2002.
- [Xu04a] N. Xu. *Prog. Part. Nucl. Phys.*, **53** 165, 2004.
- [Zwe64a] G. Zweig. *CERN preprints Th.*, 401 and 412, 1964.



Presentations and publication List

Presentations

1. Centrality dependence of K_S^0 and Λv_2 in Au + Au collisions at $\sqrt{s_{NN}} = 200$ GeV (poster)
2005 Gordon Research Conference on Nuclear Chemistry, Colby-Sawyer College, New Hampshire, USA, June 26 - July 1, 2005.
2. Centrality dependence of K_S^0 and Λv_2 in Au + Au collisions at $\sqrt{s_{NN}} = 200$ GeV (poster)
Strangeness in Quark Matter 2006, University of California, Los Angeles, USA, March 26 - March 31, 2006.
3. Centrality dependence of K_S^0 and Λv_2 in Au + Au collisions at $\sqrt{s_{NN}} = 200$ GeV (poster)
Hard Probe 2006, Asilomar, California, USA, June 9 - June 16, 2006.
4. Centrality dependence of strange and multi-strange hadron v_2 in Au + Au collisions at $\sqrt{s_{NN}} = 200$ GeV (oral)
2006 Fall Meeting of the Division of Nuclear Physics of the APS, Nashville, Tennessee, USA, October 25 - October 28, 2006.

Publication list

1. **Y. Lu**, M. Bleicher, F. Liu, Z. Liu, P. Sorensen, H. Stöcker, N. Xu, X. Zhu. “Anisotropic Flow at RHIC: How Unique is the Number-of-Constituent-Quark Scaling?”, *J. Phys. G*, **32** 1121, 2006.
2. B. I. Abelev *et al.*, STAR Collaboration. “Mass, Quark-number, and $\sqrt{s_{NN}}$ Dependence of the Second and Fourth Flow Harmonics in Ultra-Relativistic Nucleus-Nucleus Collisions. ”, *Phys. Rev. C*, **75** 054906, 2007.



Primary authors: Yuting Bai, Javier Castillo, Xin Dong, Kirill Filimonov, Hui Long, **Yan Lu**, Markus Oldenburg, Kai Schweda, Ilya Selyuzhenkov, Paul Sorensen

3. F. Liu, **Y. Lu**. “Elliptic Flow in a Hadron Transport Model.”, *J. Phys. G*, **34** 1, 2007.
4. B. I. Abelev *et al.*, STAR Collaboration. “Centrality Dependence of Charged and Strange Hadron Elliptic Flow from Au + Au Collisions at $\sqrt{s_{NN}} = 200$ GeV.”
STAR internal review
Primary authors: **Yan Lu**, Markus Oldenburg, Art Poskanzer, Kai Schweda, Ilya Selyuzhenkov, Paul Sorensen, Nu Xu
5. J. Adams *et al.*, STAR Collaboration. “Pion, Kaon, Proton and Anti-proton Transverse Momentum Distributions from p + p and d + Au Collisions at $\sqrt{s_{NN}} = 200$ GeV.”, *Phys. Lett. B*, **616** 8, 2005.
6. J. Adams *et al.*, STAR Collaboration. “Production of $e^+ e^-$ Pairs Accompanied by Nuclear Dissociation in Ultra-peripheral Heavy Ion Collision. ”, *Phys. Rev. C*, **70** 031902, 2004.
7. J. Adams *et al.*, STAR Collaboration. “Centrality and Pseudorapidity Dependence of Charged Hadron Production at Intermediate $p(T)$ in Au + Au Collisions at $\sqrt{s_{NN}} = 130$ GeV. ”, *Phys. Rev. C*, **70** 044901, 2004.
8. J. Adams *et al.*, STAR Collaboration. “Hadronization Geometry and Charge-dependent Number Autocorrelations on Axial Momentum Space in Au + Au Collisions at $\sqrt{s_{NN}} = 130$ GeV. ”, *Phys. Lett. B*, **634** 347, 2006.
9. J. Adams *et al.*, STAR Collaboration. “Transverse Momentum Dependent Modification of Dynamic Texture in Central Au + Au Collisions at $\sqrt{s_{NN}} = 200$ GeV. ”, *Phys. Rev. C*, **71** 031901, 2005. D
10. J. Adams *et al.*, STAR Collaboration. “Measurements of Transverse Energy Distributions in Au + Au Collisions at $\sqrt{s_{NN}} = 200$ GeV. ”, *Phys. Rev. C*, **70** 054907, 2004.



11. J. Adams *et al.*, STAR Collaboration. “Open Charm Yields in d + Au Collisions at $\sqrt{s_{NN}} = 200$ GeV. ”, *Phys. Rev. Lett.*, **94** 062301, 2005.
12. J. Adams *et al.*, STAR Collaboration. “Azimuthal Anisotropy and Correlations at Large Transverse Momenta in p + p and Au + Au Collisions at $\sqrt{s_{NN}} = 200$ GeV. ”, *Phys. Rev. Lett.*, **93** 252301, 2004.
13. J. Adams *et al.*, STAR Collaboration. “Transverse Momentum Correlations and Minijet Dissipation in Au + Au Collisions at $\sqrt{s_{NN}} = 130$ GeV. ”, *arXiv: nucl-ex/0408012*.
14. J. Adams *et al.*, STAR Collaboration. “Pseudorapidity Asymmetry and Centrality Dependence of Charged Hadron Spectra in d + Au Collisions at $\sqrt{s_{NN}} = 200$ GeV. ”, *Phys. Rev. C*, **70** 064907, 2004.
15. J. Adams *et al.*, STAR Collaboration. “Azimuthal Anisotropy in Au + Au Collisions at $\sqrt{s_{NN}} = 200$ GeV. ”, *Phys. Rev. C*, **72** 014904, 2005.
16. J. Adams *et al.*, STAR Collaboration. “Minijet Deformation and Charge-independent Angular Correlations on Momentum Subspace (η, ϕ) in Au + Au Collisions at $\sqrt{s_{NN}} = 130$ GeV. ”, *Phys. Rev. C*, **73** 064907, 2006.
17. J. Adams *et al.*, STAR Collaboration. “Pion Interferometry in Au + Au Collisions at $\sqrt{s_{NN}} = 200$ GeV. ”, *Phys. Rev. C*, **71** 044906, 2005.
18. J. Adams *et al.*, STAR Collaboration. “K(892)* Resonance Production in Au + Au and p + p collisions at $\sqrt{s_{NN}} = 200$ GeV at STAR. ”, *Phys. Rev. C*, **71** 064902, 2005.
19. J. Adams *et al.*, STAR Collaboration. “Experimental and Theoretical Challenges in the Search for the Quark Gluon Plasma: The STAR Collaboration’s Critical Assessment of the Evidence from RHIC Collisions. ”, *Nucl. Phys. A*, **757** 102, 2005.



20. J. Adams *et al.*, STAR Collaboration. “Multiplicity and Pseudorapidity Distributions of Photons in Au + Au Collisions at $\sqrt{s_{NN}} = 62.4$ GeV. ”, *Phys. Rev. Lett.*, **95** 062301, 2005.
21. J. Adams *et al.*, STAR Collaboration. “Multi-strange Baryon Elliptic Flow in Au + Au collisions at $\sqrt{s_{NN}} = 200$ GeV. ”, *Phys. Rev. Lett.*, **95** 122301, 2005.
22. J. Adams *et al.*, STAR Collaboration. “Incident Energy Dependence of p_T Correlations at RHIC. ”, *Phys. Rev. C*, **72** 044902, 2005.
23. J. Adams *et al.*, STAR Collaboration. “Transverse-momentum p_T Correlations on (η, ϕ) from mean p_T Fluctuations in Au + Au Collisions at $\sqrt{s_{NN}} = 200$ GeV. ”, *J. Phys. G*, **32** L37, 2006.
24. J. Adams *et al.*, STAR Collaboration. “Directed Flow in Au + Au Collisions at $\sqrt{s_{NN}} = 62$ GeV. ”, *Phys. Rev. C*, **73** 034903, 2006.
25. J. Adams *et al.*, STAR Collaboration. “Proton-Lambda Correlations in Central Au + Au Collisions at $\sqrt{s_{NN}} = 200$ GeV. ”, *Phys. Rev. C*, **74** 064906, 2006.
26. J. Adams *et al.*, STAR Collaboration. “Multiplicity and Pseudorapidity Distributions of Charged Particles and Photons at Forward Pseudorapidity in Au + Au Collisions at $\sqrt{s_{NN}} = 62.4$ GeV. ”, *Phys. Rev. C*, **73** 034906, 2006.
27. J. Adams *et al.*, STAR Collaboration. “Strangelet Search at RHIC. ”, *arXiv: nucl-ex/0511047*.
28. M. Calderon de la Barca Sanchez *et al.*, STAR Collaboration. “Open Charm Production from $d + Au$ Collisions in STAR. ”, *Eur. Phys. J. C*, **43** 187, 2005.
29. A. A. P. Suaide *et al.*, STAR Collaboration. “Charm Production in the STAR Experiment at RHIC. ”, *Eur. Phys. J. C*, **43** 193, 2005.
30. C. A. Gagliardi *et al.*, STAR Collaboration. “Recent high- p_T Results from STAR. ”, *Eur. Phys. J. C*, **43** 263, 2005.



31. J. Adams *et al.*, STAR Collaboration. “Identified Hadron Spectra at Large Transverse Momentum in $p + p$ and $d + Au$ Collisions at $\sqrt{s_{NN}} = 200$ GeV. ”, *Phys. Lett. B*, **637** 161, 2006.
32. J. Adams *et al.*, STAR Collaboration. “Measurements of Identified Particles at Intermediate Transverse Momentum in the STAR Experiment from Au + Au Collisions at $\sqrt{s_{NN}} = 200$ GeV. ”, *arXiv: nucl-ex/0601042* .
33. J. Adams *et al.*, STAR Collaboration. “Forward Neutral Pion Production in $p + p$ and $d + Au$ Collisions at $\sqrt{s_{NN}} = 200$ GeV. ”, *Phys. Rev. Lett.*, **97** 152302, 2006.
34. J. Adams *et al.*, STAR Collaboration. “Direct Observation of Dijets in Central Au + Au Collisions at $\sqrt{s_{NN}} = 200$ GeV. ”, *Phys. Rev. Lett.*, **97** 162301, 2006.
35. J. Adams *et al.*, STAR Collaboration. “Strange Baryon Resonance Production in $\sqrt{s_{NN}} = 200$ GeV $p + p$ and Au + Au Collisions. ”, *Phys. Rev. Lett.*, **97** 132301, 2006.
36. J. Adams *et al.*, STAR Collaboration. “The Energy Dependence of p_T Angular Correlations Inferred from mean p_T Fluctuation Scale Dependence in Heavy Ion Collisions at the SPS and RHIC. ”, *J. Phys. G*, **33** 451, 2007.
37. J. Adams *et al.*, STAR Collaboration. “Identified Baryon and Meson Distributions at Large Transverse Momenta from Au + Au Collisions at $\sqrt{s_{NN}} = 200$ GeV. ”, *Phys. Rev. Lett.*, **97** 152301, 2006.
38. J. Adams *et al.*, STAR Collaboration. “Scaling Properties of Hyperon Production in Au + Au Collisions at $\sqrt{s_{NN}} = 200$ GeV. ”, *arXiv: nucl-ex/0606014*.
39. J. Adams *et al.*, STAR Collaboration. “The Multiplicity Dependence of Inclusive p_T Spectra from $p + p$ Collisions at $\sqrt{s_{NN}} = 200$ GeV. ”, *Phys. Rev. D*, **74** 032006, 2006.
40. J. Adams *et al.*, STAR Collaboration. “Delta phi Delta eta Correlations in Central Au + Au Collisions at $\sqrt{s_{NN}} = 200$ GeV. ”, *Phys. Rev. C*, **75** 034901, 2007.



41. B. I. Abelev *et al.*, STAR Collaboration. “Transverse Momentum and Centrality Dependence of high- p_T Non-photonic Electron Suppression in Au + Au Collisions at $\sqrt{s_{NN}} = 200$ GeV. ”, *arXiv: nucl-ex/0607012*.
42. B. I. Abelev *et al.*, STAR Collaboration. “Strange Particle Production in $p + p$ Collisions at $\sqrt{s_{NN}} = 200$ GeV. ”, *arXiv: nucl-ex/0607033*.
43. B. I. Abelev *et al.*, STAR Collaboration. “Neutral Kaon Interferometry in Au + Au Collisions at $\sqrt{s_{NN}} = 200$ GeV. ”, *Phys. Rev. C*, **74** 054902, 2006.
44. B. I. Abelev *et al.*, STAR Collaboration. “Longitudinal Double-spin Asymmetry and Cross Section for Inclusive Jet Production in Polarized Proton Collisions at $\sqrt{s_{NN}} = 200$ GeV. ”, *Phys. Rev. Lett*, **97** 252001, 2006.
45. B. I. Abelev *et al.*, STAR Collaboration. “Rapidity and Species Dependence of Particle Production at Large Transverse Momentum for $d + Au$ Collisions at $\sqrt{s_{NN}} = 200$ GeV. ”, *arXiv: nucl-ex/0609021*.



Acknowledgements

Thanks all peoples who give me courage and helps to complete this thesis!

First, I would like to thank Professor Liu Lianshou who guides me to start the researches in high energy physics. He teaches me basic physics courses and stimulates my interests in doing some researches. Further, he provides me the chance and support to participate in IOPP, where I start my career in high energy physics. His scientific attitudes and spirits will drive me towards the scientific achievement forever!

I'm grateful to my supervisor Professor Liu Feng and Professor Xu Nu. With Feng's guide and support, I am involved in RQMD model study. Through this work, Nu knows me and further provides me a chance to do data analysis in heavy ion collisions in RNC group at LBL. I feel lucky to work in such a strong group and experience the scientific atmosphere there. Thanks them to choose this nice topic for me. Thanks them to trust and support me when I face difficulties.

Thanks all peoples in RNC group.

Thanks E-by-E physics working group and Flow discussion group.

Thanks to every member of the STAR collaboration and the RHIC operation group.

Thanks for the support from RCF and PDSF stuff.

Thanks all the professors, staffs and classmates in IOPP.

Thanks Dr. Markus Oldenburg, Professor Art Poskanzer, Dr. Kai Schweda, Dr. Ilya Selyuzhenkov, Dr. Paul Sorensen for the valuable discussions and helps on the topic of this thesis.

Thanks Chen Jiayun, Dong Xin, Du Jiaxin, Feng Aoqi, Huang Shengli, Lin Xiaoyan, Liu Haidong, Li Zhiming, Ruan lijuan, Shi Shusu, Wang Meijuan, Wu kejun, Xie Fei, Xu Mingmei, Xu Qinhua, Zhang Yifei, Zhong Chen, Zuo jiaxu, Sun Xiangming, Zhou wei to give me much help on both work and life.

Thanks to all my friends.



Finally, I'd like to thank my dear father and mother, who always support me and give me courage. Without them, I will never get there!